UC San Diego

UC San Diego Electronic Theses and Dissertations

Title

Spectroscopy of Tryptophan in Electron Transfer and Membrane Protein Folding

Permalink

https://escholarship.org/uc/item/5zr1r6c9

Author

Pena, Ignacio Lopez

Publication Date

2017

Peer reviewed|Thesis/dissertation

eScholarship.org Powered by the California Digital Library
University of California

UNIVERSITY OF CALIFORNIA, SAN DIEGO

Spectroscopy of Tryptophan in Electron Transfer and Membrane Protein Folding

A dissertation submitted in partial satisfaction of the
requirements for the degree

Doctor of Philosophy

in

Chemistry

by

Ignacio Lopez Peña

Committee in charge:

Professor Judy Kim, Chair
Professor Alexander Groisman
Professor Michael Galperin
Professor Stanley Opella
Professor Susan Taylor

2017

Copyright

Ignacio Lopez Peña, 2017

All rights reserved

The Dissertation of Ignacio Lopez Peña is approved, and it is acceptable in quality and form for publication on microfilm and electronically:

_____

_____

_____

_____

_____

Chair

University of California, San Diego

2017

TABLE OF CONTENTS

LIST OF FIGURES

LIST OF TABLES

ACKNOWLEDGEMENTS

There were many people who either directly or indirectly influenced this work, and made this dissertation possible. It gives me great pleasure to acknowledge them.

First, special thanks are due to my advisor Judy Kim for her patience and guidance. I have learned a tremendous amount about carrying out research from her, and this work would not have been possible without her scientific insight, endless encouragement, and enthusiasm. Some of my experiments worked, and many others did not. I especially thank her for promoting independence and self-sufficiency, and for developing my confidence when I thought I was completely lost. Judy's analytical and positive approach to instruction and scientific inquiry has been and will continue to be a constant source of inspiration.

I thank Brian Leigh for being supportive and promoting good research. He was always eager to help, quiz me, or make an evening run for coffee.

I also thank Michael Tauber for his valuable scientific feedback on these projects, and for all the time he spent debugging electronics and resuscitating the ns TA system with me. I am also thankful for having the opportunity to teach CHEM 105A with Michael, which was one of my most rewarding experiences as teacher.

The members of the Kim lab have helped tremendously in this research, and were an invaluable source of knowledge and inspiration. Special thanks to Guipeun Kang for her infinite patience, and for helping me learn everything there was to know about OmpA. She was always a daily beacon of immense support and cheer. Many thanks to Joel Rivera, Jen Daluz, Deeann Asamoto, Ivan Kozachenko, and Justine Liang for all the insightful discussions we shared, and for being passionate about providing feedback during practice talks. I would like to recognize the members that inspired me to join, and get started in the

group: Diana Schlamadinger, Hannah Shafaat, Bethany Larson Berg, and Jennifer Pomponio. I also appreciate all the efforts of our excellent undergraduates that have contributed to the OmpA project: Derek Deng, Saajan Bhakta, and Weihan Cao. I would like to thank our current and past laser spectroscopist neighbors in the Tauber lab for being easy to talk to about optics or pastries: Samantha Doyle, Megan Stone, Shuwan Huang, and Chen Wang. Special thanks to Maria Angelella for regularly helping me with my struggles with the TA system, and teaching me the value of taking detailed notes and checking everything twice.

I would like to express my gratitude to Jörg Kleinschmidt of the Universität Kassel for his tremendous excitement about Skp research, and his help with these experiments.

Many thanks to MBTG And GAANN faculty and colleagues for committing their time to organize meetings, and for providing helpful criticism.

I would like to acknowledge Robert Konecny and the W. M. Keck Laboratory for Integrated Biology Foundation for the computing resources that supported this research.

I would also like to acknowledge the Christopher Murphy and Jeff Rances for always offering me outreach opportunities that allowed this work to have impact outside of the lab. I also acknowledge the rest of the student affairs office, chemistry stockroom, machine shop, and Art Of Espresso staff for helping me avoid many crises.

I appreciate the memories and therapy that I shared with my friends: Greg Medders, Zach Berndsen, Kris Haushalter, and Jesse Meyer, and the rest of my teammates of the *Urey Fury* softball team. Their incredible enthusiasm for science promoted good research.

My research experience at SFSU introduced me to biophysical experiments and inspired me to pursue research. For that I thank Raymond Esquerra and Frank Bayliss.

The Fonseca family deserves credit for all of their love and support over the years.

I deeply appreciate all the love and support from my parents Ignacio Lopez Mendez and Lupita Peña, and my brothers Christian and Andrew. Thanks for understanding the need for me to work long hours, even though the reasons may not have been clear, and for always being supportive.

I am immensely grateful to Silvia Fonseca for her love, support, and encouragement. She gave me strength to overcome every challenge.

Lastly, the generous financial support of the National Institutes of Health, National Science Foundation, Department of Education, and a San Diego Fellowship made this work possible.

Chapter 3 is in preparation for submission: Lopez-Peña, I, Kim, J. E, "Photogeneration of tryptophan radical from the triplet excited state in azurin". The dissertation author was the primary investigator and author of this paper.

Chapter 4 is in preparation for submission: Lopez-Peña, I, Kleinschmidt, J. H, Kim, J. E, "Solvent deuterium isotope effect on the decay kinetics of the tryptophan triplet in membrane protein folding". The dissertation author was the primary investigator and author of this paper.

Chapter 5, in full, is a reprint of our previously published work. Reproduced with permission from López-Peña, I, Leigh, B. S., Schlamadinger, D. E., Kim, J. E, "Insights into protein structure and dynamics by ultraviolet and visible resonance Raman Spectroscopy", Biochemistry 2015, 54, 4770-4783. Copyright 2015 American Chemical Society. The dissertation author was the primary investigator and author of this paper.

VITA

2010 Bachelor of Science, San Francisco State University

2012 Master of Science, University of California, San Diego

2017 Doctor of Philosophy, University of California, San Diego

PUBLICATIONS

López-Peña, I., Leigh, B. S., Schlamadinger, D. E., Kim, J. E. “Insights into protein structure and dynamics by ultraviolet and visible resonance Raman spectroscopy”, *Biochemistry*, **2015**, 54, 4770-4783.

Kang, G., López-Peña, I., Saajan, B., and Kim, J.E. “Probing membrane protein structure and dynamics by fluorescence spectroscopy”, *Encyclopedia of Analytical Chemistry*, **2013**, 1-21

Kang, G., López-Peña, I., Oklejas, V., Gary, C.S., Cao, W., Kim, J.E. “Förster resonance energy transfer as a probe of membrane protein folding”, *Biochim. Biophys. Acta* **2011**, 1818, 154-161.

Esquerra, R.M., López-Peña, I., Tipgunlakant, P., Birukou, I., Nguyen, R.L., Soman, J., Olson, J.S., Kliger, D.S., Goldbeck, R.A. “Kinetic Spectroscopy of Heme Hydration and Ligand Binding in Myoglobin and Isolated Hemoglobin Chains: an Optical Window into the Functional Dynamics of Water in the Heme Pocket”, *Phys. Chem. Chem. Phys.*, **2010**, 12, 10270-10278

ABSTRACT OF THE DISSERTATION

Spectroscopy of Tryptophan in Electron Transfer and Membrane Protein Folding

by

Ignacio Lopez Peña

Doctor of Philosophy in Chemistry

University of California, San Diego, 2017

Professor Judy Kim, Chair

The tryptophan fluorescence of proteins has been widely used to examine protein structure, ligand binding, and conformational changes. The triplet state is also well suited for examining protein structure and dynamics because of its long lifetime in some proteins, up to seconds. This dissertation focuses on several aspects of the tryptophan triplet, especially the photochemistry and photophysics of this chromophore in electron transfer and membrane protein folding.

Chapter 3 describes the role of the tryptophan triplet state in mediating intermolecular electron transfer (ET). The ET rate across large distances is slow relative to

a typical fluorescence lifetime. The photooxidation reaction of tryptophan in mutants of apo- and Zn(II)azurin is shown to involve the triplet state via measurements of triplet absorption and phosphorescence in the presence of an external electron acceptor. The formation of neutral radical is demonstrated to coincide with quenched phosphorescence. The formation kinetics of the triplet state and neutral radical were modeled, and the results of 1×10^{7} and 8×10^{5} sec^{-1}, respectively, agree with a proposed intermolecular ET pathway (~18 Å) along 10 covalent bonds and two through-space steps.

The tryptophan triplet decay kinetics are known to be different in D_2O compared to H_2O. This isotope effect is correlated with local solvent accessibility, and can be used to examine changes in hydration during membrane protein folding. Chapter 4 describes experiments on a model tryptophan compound, a membrane-associated peptide (melittin), and a transmembrane protein (OmpA). An isotope effect was present when tryptophan was exposed to bulk solvent, such as in unfolded melittin $\left(k_{H_2O}/k_{D_2O}=0.71\right)$, but disappeared when buried in a bilayer, such as in folded melittin $\left(k_{H_2O}/k_{D_2O}=1.07\right)$. Additionally, when OmpA was bound to the native molecular chaperone Skp, an isotope effect was absent $\left(k_{H_2O}/k_{D_2O}=1.00\right)$. These results suggest Skp plays a role in desolvating OmpA, allowing OmpA to fold into the bilayer more easily. These data indicate that triplet photophysics may be a general tool to determine changes in hydration for proteins.

Finally, spectroscopy of protein chromophores, including tryptophan, and prosthetic groups reveals local structure and dynamics. Chapter 5 discusses applications of UV and visible resonance Raman spectroscopy to proteins.

1 Introduction

1.1 Motivation

Since Pauling and Corey deduced the structure of the α-helix and β-sheet, chemists have been curious about protein structure. The protein scaffold is involved in essentially every cellular process. Proteins enable energy conversion, chemical storage, ion transport, and many other biochemical transformations.[1] The three-dimensional shape of a protein is key for its function. The native conformation is formed when a nascent polypeptide spontaneously self-assembles in a remarkable process called folding.[2-3] The one-dimensional amino acid sequence contains all the information necessary for folding. Misfolding can occur if there are mutants in the encoded gene of a protein, which in turn, may lead to problems in folding kinetics and/or thermodynamics; these misfolded proteins are implicated in several aggregation-related diseases. Given the fundamental importance of protein folding, a natural question emerges: Can undiscovered concepts in catalysis or disease be revealed by understanding the interplay between protein structure and function?

In protein structure elucidation, high-resolution X-ray diffraction and NMR spectroscopy are powerful imaging tools. By combining optical spectroscopy with atomic-resolution structures, a comprehensive mechanistic picture of a protein can be illustrated. An optical spectrum of a chromophore or prosthetic group reveals information about bonding and local environment. For example, an absorption spectrum reports on electronic structure, and Raman spectra provide information about vibrational structure. In addition to steady-state insights, the kinetics of transient species can be investigated using rapid mixing or photolysis techniques. While structural tools only reflect the steady-state picture

of a protein, kinetics provides insight into the dynamics that is key for protein function. Optical studies of protein dynamics have led to important contributions to our understanding of ligand binding[4-5], light transduction in rhodopsin[6], and allostery in heme proteins[7-8]. An important requirement for optical studies is a reliable chromophore that reports on structures and/or dynamics. In proteins, the aromatic amino acid tryptophan is a ubiquitous spectroscopic probe. Spectroscopic studies of tryptophan are the subject of this dissertation.

1.2 Tryptophan optical transitions

The aromatic amino acid side chains, i.e. phenylalanine (Phe), tyrosine (Tyr), and tryptophan (Trp), give rise to an ultraviolet absorption between 250 and 300 nm. The complex photophysics and photochemistry of these aromatic residues in aqueous solutions and proteins have been the interest of several theoretical and experimental investigations. As shown in Figure 1.1, the maximum molar absorptivity of Trp is greater than that of Tyr by a factor of 4, and exceeds the molar absorptivity of Phe by more than 20-fold. The broad Trp absorption at 280 nm is the result of two overlapping absorption bands. These are the L_a and L_b transitions in Platt notation.[9] The Trp absorption is slightly red shifted in comparison to Tyr and Phe absorption maxima. This difference permits selective excitation at 295 nm, which allows interrogation of Trp in proteins without interference from Tyr or Phe.

The absorption of light promotes a molecule to a new electronic state (S_n). As shown in Figure 1.2, several unimolecular pathways can dissipate the absorbed energy.[10] Following photoexcitation, a molecule quickly relaxes to the lowest vibrational energy level of the lowest singlet excited state (S_1). The non-radiative deactivation of the singlet excited state proceeds via internal conversion to the ground state (S_0). The efficiency of internal conversion depends, in large part, on vibrionic coupling to the solvent. The coupling efficiency of Trp with water has applications to membrane protein folding, and this topic is the focus of Chapter 4. Another non-radiative pathway is intersystem crossing to the triplet state ($S_1 \rightarrow T_n$). The rate of intersystem crossing can be enhanced by bimolecular interactions with heavy atoms, whose large angular momentum enhances spin-orbit coupling.[11] The transition $^1(\pi\text{-}\pi^*) \leftrightarrow {}^3(\pi\text{-}\pi^*)$ is formally spin-forbidden by El Sayed's

rules, but weakly allowed in Trp. Because of the forbidden nature of the transition singlet ↔ triplet, the triplet lifetime is on the order of ms, and is several orders of magnitude longer than the ns lifetime of the singlet state.

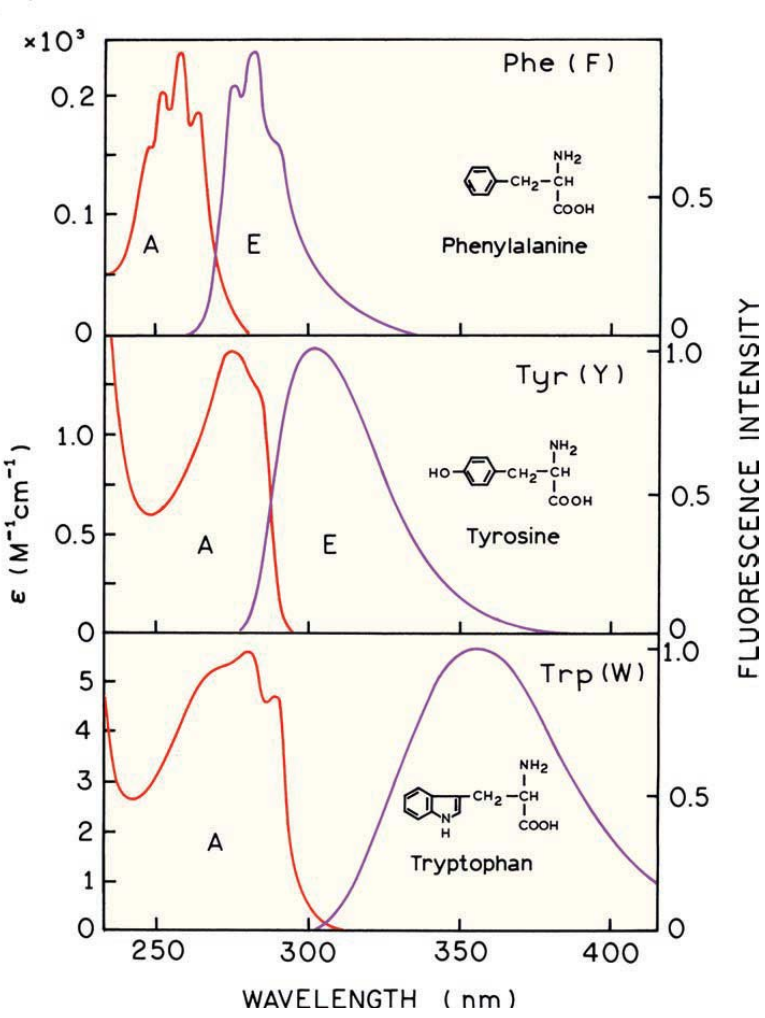

Figure 1.1 Absorption (A) and emission (E) of the aromatic amino acid residues in aqueous buffer, pH 7. Reproduced from ref 4.

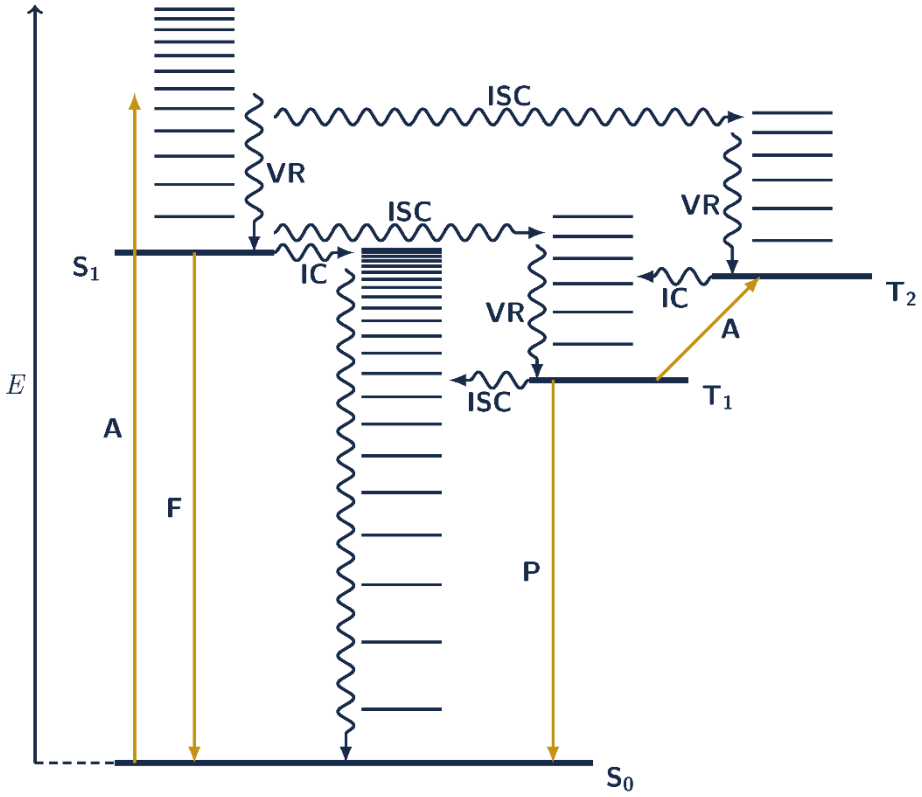

Figure 1.2 Jablonski diagram indicating electronic states and vibrational sublevels. Absorption (A), fluorescence (F), and phosphorescence (P) are shown as solid arrows. Higher-lying energy levels are denoted S_n (singlet states) or T_n (triplet states). Nonradiative transitions, such as internal conversion (IC), intersystem crossing (ISC), and vibrational relaxation (VR), are represented by wavy arrows. Reproduced from ref 10.

Fluorescence ($S_1 \rightarrow S_0$) and phosphorescence ($T_1 \rightarrow S_0$) are radiative transitions to the singlet ground state. The fluorescence from Trp is intense, broad, and featureless.[4] Furthermore, it is sensitive to the polarity of the local environment. For instance, Trp displays an emission maximum of 308 nm when buried in the hydrophobic interior of azurin. When solvent exposed, the Trp emission shifts to 355 nm. The fluorescence emission maximum, anisotropy, quantum yield, and lifetime are important probes for investigating protein conformational changes, such as in protein folding and unfolding. Most proteins also display room-temperature phosphorescence in deoxygenated solutions.[12-13] The phosphorescence from Trp is easily distinguished from the fluorescence. It has vibrionic structure with a 0-0 band at ~410 nm, as shown in Figure 1.3. In contrast to fluorescence, phosphorescence is not sensitive to the polarity of the local environment. However, the long phosphorescence lifetime is highly susceptible to bimolecular quenching. In addition to radiative decay in the form of fluorescence and phosphorescence, a variety of non-radiative deactivation mechanisms can depopulate excited states and thereby quench steady-state emission; these mechanisms include bimolecular energy transfer, charge transfer, electron transfer, collisions, and excited state chemical reactions. The quenching of the phosphorescence in azurin by an external electron transfer is the subject of Chapter 3.

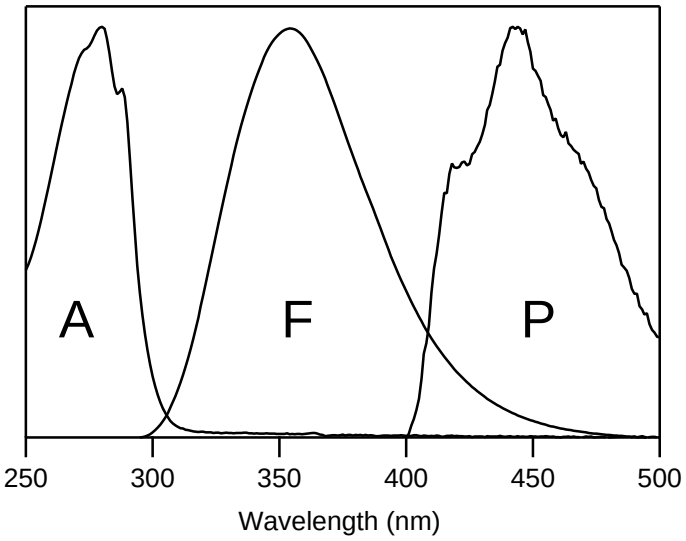

Figure 1.3 Absorption (A), fluorescence (F), and phosphorescence (P) of the model compound N-acetyl-tryptophanamide (NATA) at room-temperature in aqueous buffer, pH 7. The steady-state fluorescence and phosphorescnece spectra were acquired with 295 nm excitation. The phosphorescence spectrum was acquired in the presence of 4 M KI and 1 mM $Na_2S_2O_4$ to the NATA solution.

1.3 Excited state reactivity

The lowest singlet and triplet excited states of Trp are reactive. The excited state energies from their respective 0-0 transitions are about 4.0 and 3.0 eV. When Trp is photoexcited with ultraviolet radiation in aqueous solution, the primary photochemical process is ionization, which may proceed via monophotonic ionization from a pre-fluorescent state, or via two photon processes from a thermally equilibrated excited state.[14] In rigid solutions, the triplet state is the main precursor in ionization.[15]

The reactivity of the excited states toward an electron acceptor (A) can be characterized by electron transfer, such that

$$\mathrm{TrpH}\cdots\mathrm{A} \xrightarrow{h\nu} {}^{*}\mathrm{TrpH}\cdots\mathrm{A} \xrightarrow{k_{ET}} \mathrm{TrpH}^{+\bullet}\cdots\mathrm{A}^{-\bullet}$$

The rate of electron transfer depends on the driving force, distance, and reorganization energy as described by Marcus.[16] The photooxidation of Trp produces oxidized radical intermediates, and involves an initial electron transfer (ET) event followed by a proton transfer (PT) event. The rate of deprotonation of the cation radical is estimated to be on the order of 10^6 sec^{-1}.[17] The Trp cation and neutral radical in aqueous solution have been characterized by transient absorption spectroscopy.[18] The photoionization and photochemistry of the triplet state, and its role in radical formation in azurin is the subject of Chapter 3.

1.4 Overview

This dissertation examines the photochemistry and photophysics of tryptophan in a protein electron transfer reaction, and in membrane protein folding. The triplet state dynamics are a unifying theme of these studies. In Chapter 2, the general spectroscopic instrumentation is described, and protein expression and purification procedures are presented.

Chapter 3 is centered on the mechanisms of photooxidation of tryptophan in a model protein, azurin. The UV-photooxidation of Trp in Zn-substituted azurin in the presence of a suitable exogenous electron acceptor produces stable neutral radical.[19] The coordinated Zn-metal is not redox active in the photooxidation reaction. The backbone C_α rms deviation of Cu(II)-, Zn(II)-, and apoprotein X-ray crystal structures is less than 2.0 Å, with most of the differences emerging from the metal coordinating ligands.[20] The structure of azurin is surprisingly rigid (Figure 1.4). What is the role of protein dynamics in the photooxidation mechanism? In Chapter 3, the formation of Trp neutral radical in apoazurin is investigated. The phosphorescence of apoazurin is shown to be quenched by an external electron acceptor, and this quenching efficiency correlates with formation of the neutral radical. The steady-state concentration of triplet under continuous illumination is determined from the triplet-triplet absorption spectrum, and the susceptibility of the triplet state to photoionization is described. The kinetics of photogeneration of neutral radical in the presence of quencher is examined, and an intermolecular electron transfer pathway is proposed. These results are the first to implicate the triplet state in formation of the neutral Trp radical in azurin.

Chapters 4 focuses on the triplet state as a probe of solvent exposure during membrane protein folding. The outer membrane protein A (OmpA) is a beta-barrel transmembrane protein that is capable of refolding spontaneously into synthetic lipid bilayers from the denatured state.[21] The native protein contains five native tryptophan residues in the transmembrane region that are excellent spectroscopic probes for folding. These residues are shown in the folded structure in Figure 1.5, which is reconstructed from X-ray crystal structures of the transmembrane (1-171) and soluble domains (171-325). The high-resolution structure describes a steady-state picture of the protein. In protein folding, one important thermodynamic driving force is solvent reorganization, also known as the hydrophobic effect.[22] How does protein hydration affect folding intermediates during insertion and folding? In Chapter 4, the triplet decay kinetics of a lipid-associated peptide, melittin, and single-Trp mutants of OmpA were studied in deoxygenated water and deuterium oxide solutions. The decay kinetics exhibit an isotope effect due to vibrionic coupling to the solvent. This isotope effect can be utilized to investigate the change in hydration during the folding reaction, and help elucidate chaperone-binding events and membrane protein folding mechanisms. These results are important for characterizing the role of protein solvation in membrane protein folding.

In Chapter 5, the application of ultraviolet and visible resonance Raman in studies of protein structure and dynamics is reviewed. The fast time resolution and high selectivity of resonance Raman makes it a valuable tool for obtaining structural information about protein chromophores and prosthetic groups. Examples include rhodopsin, soluble and membrane proteins, and peptides. Despite numerous attempts to elucidate the vibrational structure of Trp triplet, a clear spectrum is not yet reported, in part because of facile

photoionization of the triplet state described in Chapter 3. Nonetheless, Raman spectra of an unidentified species, possibly triplet state, that is resonant with blue excitation is included in the Appendix.

Spectroscopy of tryptophan, as well as its photophysics and photochemistry, is a valuable tool for investigating protein structure and dynamics. The benefits of my studies to future investigations of proteins are presented as concluding remarks in Chapter 6.

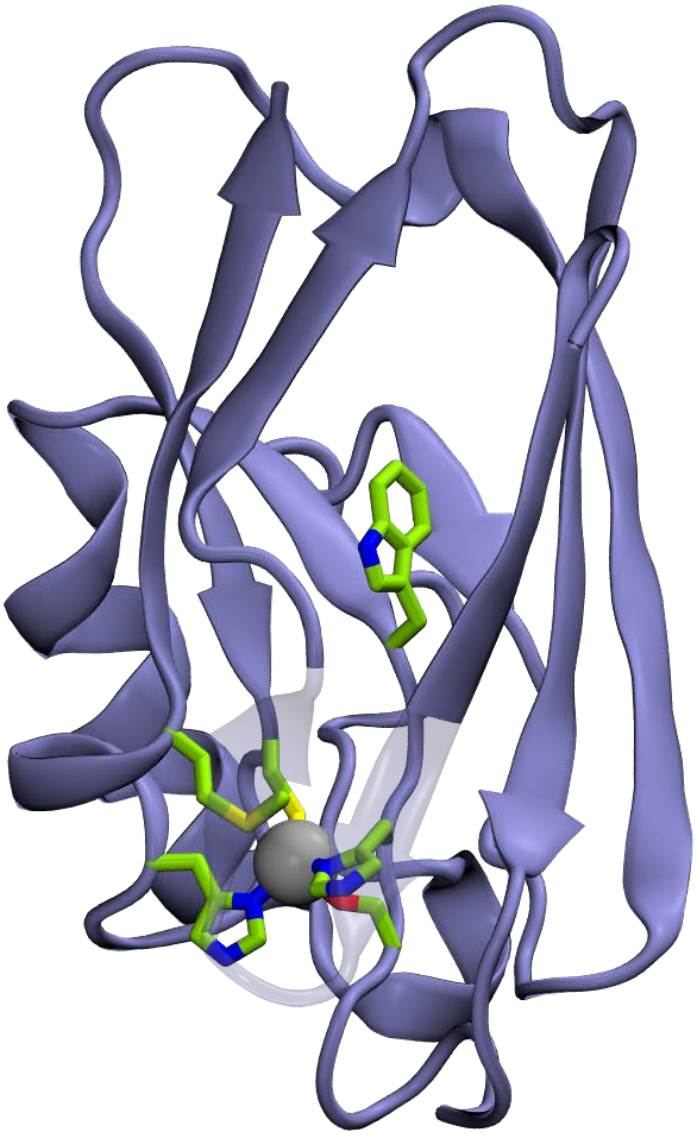

Figure 1.4 X-ray crystal structure of Zn-substituted azurin from PDB 1E67. The five coordinating ligands G45 (backbone carbonyl), H46, C112 H117, and M121, as well as the single buried W48 residue are shown.

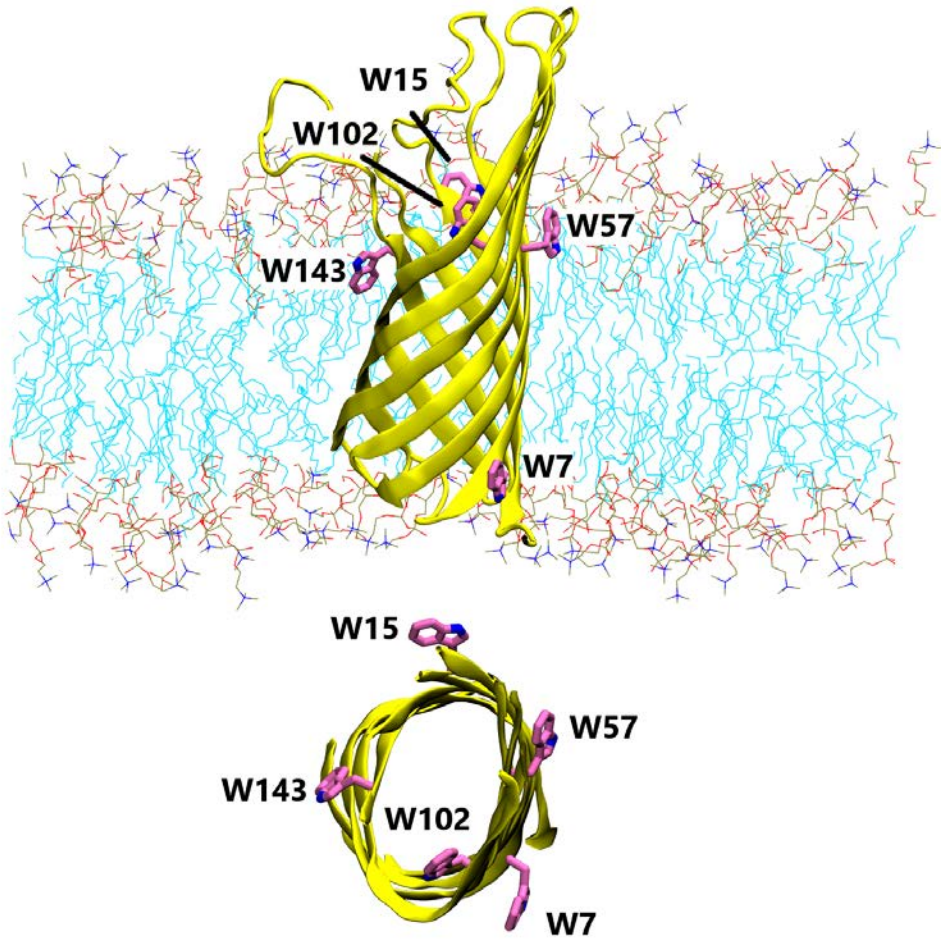

Figure 1.5 OmpA transmembrane (PDB:1QJP). The loops were reconstructed using MODELLER. Native tryptophan residues in their respective positions are shown.

1.5 References

1. Berg, J. M.; Tymoczko, J. L.; Stryer, L., *Biochemistry*. 7th ed.; Freeman: New York, 1988.

2. Anfinsen, C. B., Principles that govern the folding of protein chains. *Science* **1973,** *181*, 223-230.

3. Bryngelson, J. D.; Onuchic, J. N.; Socci, N. D.; Wolynes, P. G., Funnels, pathways, and the energy landscape of protein folding: a synthesis. *Proteins* **1995,** *21* (3), 167-195.

4. Lakowicz, J. R., *Principles of fluorescence spectroscopy*. 3rd ed.; Springer: New York, 2006.

5. Haustein, E.; Schwille, P., Ultrasensitive investigations of biological systems by fluorescence correlation spectroscopy. *Methods* **2003,** *29* (2), 153-166.

6. Smith, S. O., Structure and activation of the visual pigment rhodopsin. *Annu. Rev. Biophys.* **2010,** *39*, 309-328.

7. Derbyshire, E. R.; Marletta, M. A., Structure and regulation of soluble guanylate cyclase. *Annu. Rev. Biochem.* **2012,** *81*, 533-559.

8. Perutz, M. F.; Wilkinson, A. J.; Paoli, M.; Dodson, G. G., The stereochemical mechanism of the cooperative effects in hemoglobin revisited. *Annu. Rev. Biophys. Biomol. Struct.* **1998,** *27*, 1-34.

9. Platt, J. R., Classification of spectra of cata-condensed hydrocarbons. *J. Chem. Phys.* **1949,** *17* (5), 484-495.

10. Klessinger, M.; Michl, J., *Excited states and photochemistry of organic molecules*. VCH: New York, 1995.

11. Turro, N. J., *Modern molecular photochemistry*. University Science Books: California, 1992.

12. Saviotti, M. L.; Galley, W. C., Room temperature phosphorescence and the dynamic aspects of protein structure. *Proc. Natl. Acad. Sci. U. S. A.* **1974,** *71*, 4154-4158.

13. Vanderkooi, J. M.; Calhoun, D. B.; Englander, S. W., On the prevalence of room-temperature protein phosphorescence. *Science* **1987,** *236*, 568-569.

14. Grossweiner, L. I.; Brendzel, A. M.; Blum, A., Multiple pathways of tryptophan photoionization. *Chem. Phys.* **1981,** *57*, 147-155.

15. Moan, J.; Steen, H. B., Photoinduced trapped electrons in rigid polar solution. II. Kinetics and cross section of two-quantum ionization. *J. Phys. Chem.* **1971,** *75* (19), 2893-2897.

16. Marcus, R. A., On the theory of oxidation-reduction reactions involving electron transfer. I*. *J. Phys. Chem.* **1956,** *24*, 966-978.

17. Shafaat, H. S.; Leigh, B. S.; Tauber, M. J.; Kim, J. E., Spectroscopic comparison of photogenerated tryptophan radicals in azurin: effects of local environment and structure. *J. Am. Chem. Soc.* **2010,** *132*, 9030-9039.

18. Bent, D. V.; Hayon, E., Excited state chemistry of aromatic amino acids and related peptides. III. Tryptophan. *J. Am. Chem. Soc.* **1975,** *97* (10), 2612-2619.

19. Larson, B. C.; Pomponio, J. R.; Shafaat, H. S.; Kim, R. H.; Leigh, B. S.; Tauber, M. J.; Kim, J. E., Photogeneration and quenching of tryptophan radical in azurin. *J. Phys. Chem. B* **2015,** *119*, 9438-9449.

20. Nar, H.; Messerschmidt, A.; Huber, R.; van de Kamp, M.; Canters, G. W., Crystal structure of *Pseudomonas aeruginosa* apo-azurin at 1.85 Å resolution. *FEBS Lett.* **1992,** *306*, 119-124.

21. Surrey, T.; Jähnig, F., Refolding and oriented insertion of a membrane protein into a lipid bilayer. *Proc. Natl. Acad. Sci. U. S. A.* **1992,** *89*, 7457-7461.

22. Kauzmann, W., Some factors in the interpretation of protein denaturation. *Adv. Protein Chem.* **1959,** *14*, 1-63.

2 Experimental techniques

2.1 Steady-state photolysis and absorption

The continuous excitation (photolysis) of protein samples with ultraviolet (UV) and blue light was used to perturb the ground state equilibrium, creating transient species that were analyzed using a dual beam scanning spectrophotometer. In Figure 2.1, a schematic of the optical paths through the sample are shown. The absorbance of samples was measured along the long 10-mm pathlength (ℓ) of a 10 × 2 mm cuvette. The bandwidth of the probe beam from the UV-Vis spectrophotometer was set to 2 nm, and the slowest wavelength scanning speed of 300 nm/sec was used for optimal single to noise data. The width of this probe beam was ~1.5-2.0 mm at the face of the cuvette, which ensured that the probe beam was smaller than the 2-mm width of the sample in the cuvette. The excitation sources λ_1 and λ_2 were aligned orthogonal to the probe beam along the short pathlength (d). The concentration of the sample was chosen such that the absorbance along the short pathlength was ~0.3 optical density (OD).

A UV light-emitting diode (LED) was carefully selected to provide intense actinic light. The wavelength and power output of the LED is critical for achieving sufficiently high excitation rates, and thus measurable steady-state concentrations of transient species. The wavelength at 280 nm (λ_1) was selected because it corresponds to the peak L_a/L_b absorption. The power output of several LEDs from multiple sources were tested, and only the Crystal IS light source was found to fall within the advertised binned power range of 1 mW. This LED uses a fused-silica ball lens integrated into a TO-39 package. The typical peak profile is shown in Figure 1.2. The photolysis area on the sample was 8 x 8 mm square.

In general, the power output and wavelength stability of thermally-stable UV LEDs are excellent. The on-time of the LED was less than 5 minutes during the experiment, and temperature during this time was stable as measured by the case temperature.

A blue laser diode was used as a second light source for photolysis. This diode was harvested from a Pioneer BDR-209DBK drive. The output wavelength for the Blu-ray specification is 405 nm (λ_2). The blue light was focused using an AR-coated aspherical F/0.7 lens, and made roughly collinear with the UV light through the sample. The average output power at the sample was 440 mW and the beam dimensions were similar to the UV beam.

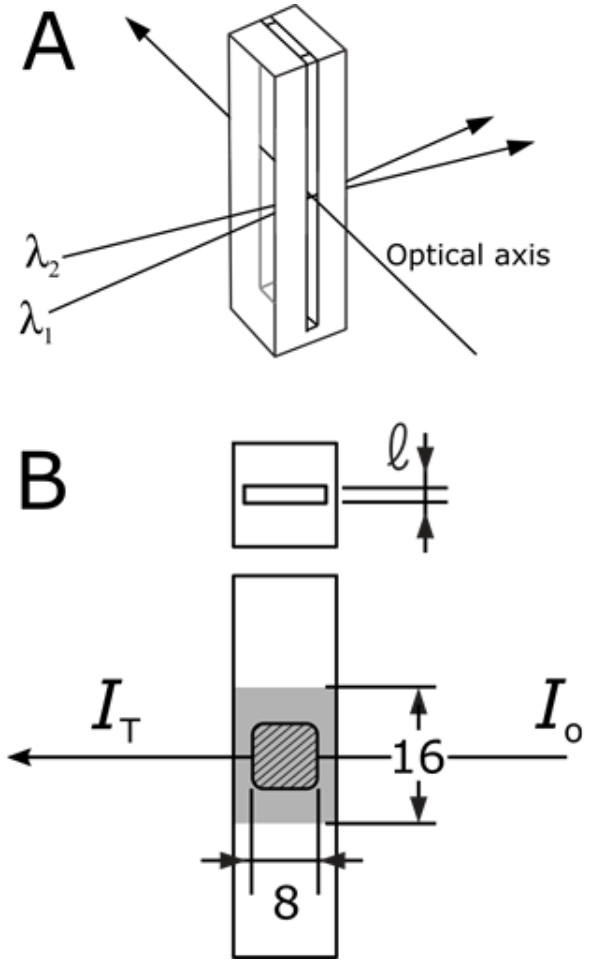

Figure 2.1 Steady-state photolysis paths of the cuvette. The optical axis is defined by the spectrophotometer probe beam path. Actinic light with wavelengths λ_1 and/or λ_2 entered the sample orthogonal to the optical axis of the UV-Vis spectrophotometer with incident intensity I_0. Typical dimensions for the UV and blue actinic beams (λ_1 and λ_2) are labeled; the excitation pathlength were $\boldsymbol{\ell}$=2 mm; the incident beam with intensity I_0 had a typical width of 1.5-1.8 mm.

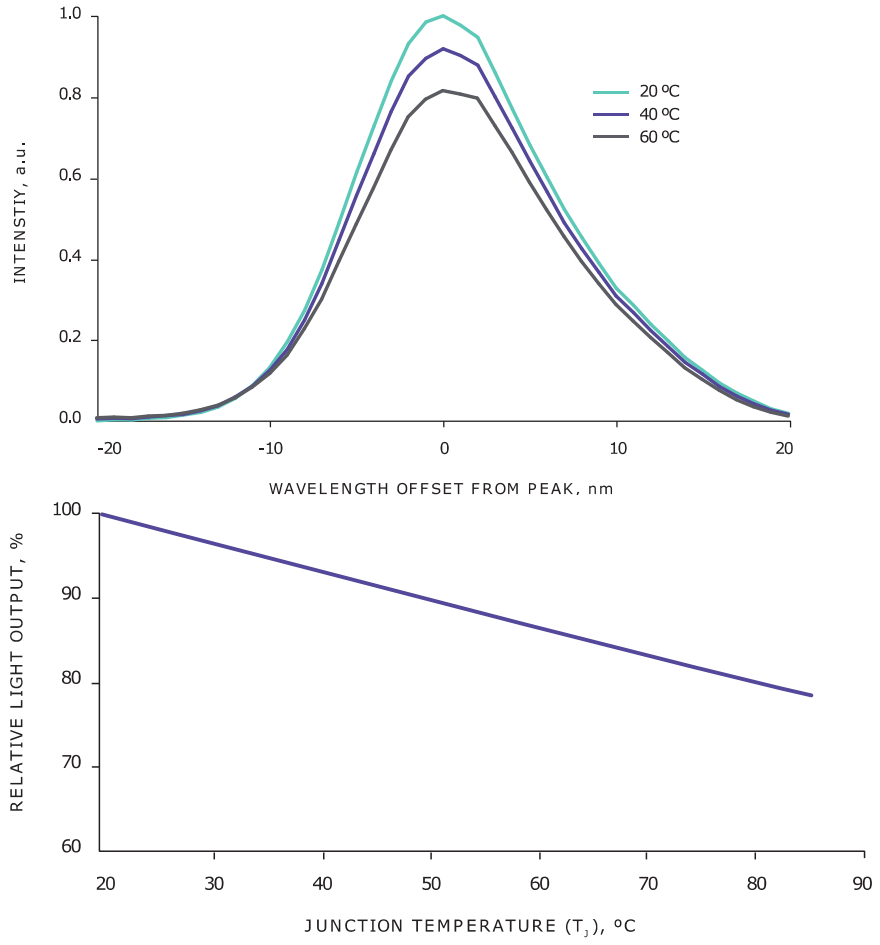

Figure 2.2 Temperature dependence of spectral profile (top), and output (bottom) of the commercial UV LED. Data are from the manufacturer's specification sheets.

2.2 Nanosecond (ns) time-resolved transient absorption

By monitoring the transient absorption signal of photoexcited samples, information about the dynamics of the transient species can be obtained. The ns time-resolved instrument is the same as described previously.[1] An optical parametric oscillator (OPOTEK, Magic Prism) was pumped at 20 Hz using the third-harmonic of a Nd:YAG laser (Quantel, Brilliant) to produce pulses at 580 nm. The output was directed through a barium borate (BBO) crystal to generate frequency doubled actinic pulses at 290 nm with an average energy per pulse of 50 μJ at the sample. This wavelength selectively excites Trp in proteins containing Tyr and Phe. A continuous-wave 65 W Xe arc light (PTI, New Jersey) was used as the probe beam. The damaging infrared and deep-UV light from the lamp was eliminated with a 10 cm IR water filter and a UV (>390 nm) long pass filter. The excitation and probe beams were made collinear with diameters of about 4-5 mm as they entered the sample. A fiber optic was used to direct the probe light to the detector; this fiber optic was unusually long (33 meters) because it also served to temporally separate Q-switching noise from detection. The output from the fiber optic was focused onto a PTI monochromator (bandpass 10 nm) and detected with a PMT (Hamamatsu R928) operating with five biased dynodes. The anode current was converted to voltage using a transimpedance amplifier (Edmund Optics 59-179), and recorded by a 500 MHz digital oscilloscope (LeCroy Wavesurfer 452). The bandwidth was limited to 14 MHz. The voltage transient was converted to an absorption signal using the pre-pulse voltage as the incident intensity (I_0).

2.3 Expression and purification of OmpA and azurin

2.3.1 OmpA

The folding of recombinant wild-type and mutant outer membrane protein A (OmpA) from *Escherichia coli* was examined using the tryptophan residue as a spectroscopic probe for insertion and assembly into synthetic lipid bilayers. The procedure for the expression and purification of OmpA was used as described previously.[2-6]

Unless specified, all single-trp mutant constructs used the pET1102 vector originally developed by Kleinschmidt et al.[7] This plasmid was a gift from Prof. Tamm, University of Virigina. The plasmid was modified earlier using site-directed mutagenesis to generate single-trp mutants,[5] and used here without any further modifications. In wild-type OmpA, the native tryptophan residues are located at position 7, 15, 57, 102, and 143. In single-Trp mutants, four of the five native Trp codons were changed to Phe. Single-trp variants fold into synthetic bilayers.[5]

Recombinant protein was expressed using OmpA- and OmpC-free *E. Coli* strain JF733. Bacteria were grown in six 1 L conical flasks with Luria Broth (LB) media. Ampicillin was added to a final concentration of 50 μg/mL, and isopropyl β-D-thiogalactoside (IPTG) to a final concentration of 1 mM. Each flask was inoculated with overnight culture, and grown at 37 ℃ for about 6 hours (OD_{600}=1) with constant shaking at 180 rpm. Cells were pelleted by centrifugation at 6,000 rpm for 10 minutes, and the pellets were harvested and frozen at -80℃ overnight.

Cells were lysed in two steps. First, cells were resuspended in lysis solution (0.4 M sucrose, 5 mM Tris-HCl, 10 mM EDTA, and 0.25 mg/mL lysozyme) containing 1 mM

phenylmethylsulfonyl fluoride (PMSF) as a protease inhibitor. The resuspended cells were stirred on ice for 1 hour. Second, the resuspended cells were sonicated using a ½" horn tip for 5 minutes with a 50% duty cycle. The lysed mixture was first pelleted by centrifugation at 5000 rpm to remove unwanted cell junk. The remaining supernatant was spun at 17,000 rpm for 90 minutes to separate a membrane protein pellet from the supernatant. The remaining brown-red pellet contains OmpA.

The membrane pellet was further separated into peripheral and integral membrane protein fractions. The pellet was resuspended in a pre-extraction solution (3.5 M urea, 20 mM Tris-HCl, 0.05 % 2-mercaptoethanol). This mild-denaturant solution releases peripheral proteins from the membrane. The pre-extraction mixture was pelleted by centrifugation at 17,000 rpm for 2 hours. The supernatant was then separated from the membrane proteins and OmpA-containing pellet. The pellet was resuspended in 70 mL solution a 1:1 mixture of denaturant (8 M urea, 20 mM Tris-HCl, 0.1 % 2-ME, pH 8.5) and isopropanol. A final centrifugation at 17,000 rpm for 1.5 hours is used to separate OmpA-containing supernatant.

The OmpA-containing supernatant was purified by anion exchange chromatography. The supernatant was loaded onto a prepacked 5 mL HiTrap Q Sepharose FF column (GE Healthcare) equilibrated in denaturant buffer (8 M urea, 15 mM Tris-HCl, 0.05 % 2-ME, pH 8.5). The protein was eluted using a salt gradient, and the eluent was analyzed for absorbance at 280 nm. The fractions with the highest $\lambda_{280}/\lambda_{260}$ were collected. In addition, the purity was further was assessed by SDS-polyacrylamide gel electrophoresis (PAGE). The fractions were concentrated, desalted, and buffer exchanged using an Amicon

stirring cell with a YM-10 membrane. Purified, unfolded OmpA samples were frozen, and stored at -80°C. Samples were thawed when needed.

2.3.2 Azurin

Apo- and metal-substituted azurin samples were kind gifts from members of the Kim group. The expression and purification protocols are described by Larson et al[8] and in the M.S. thesis of Justine Liang[9].

For experiments that involved the triplet state, protein samples were prepared anaerobically in atmospherically controlled cuvettes. Samples were subjected to repeat cycles of vacuum and argon gas using a Schlenk line, and sealed under 1 atm of Ar. The sample concentrations, optical densities, and pathlengths are described in respective sections. Samples were stirred with a magnetic stir bar during the duration of the experiment. The degradation was examined by absorption at the end of each experiment.

2.4 References

1. Wang, C.; Angelella, M.; Kuo, C. H.; Tauber, M. J., Singlet fission in carotenoid aggregates: insights from transient absorption spectroscopy. *Proc. SPIE* **2012,** *8459*.

2. Teather, R. M.; Bramhall, J.; Riede, I.; Wright, J. K.; Fürst, M.; Aichele, G.; Wilhelm, U.; Overath, P., Lactose carrier protein of *Escherichia coli*. *Eur. J. Biochem.* **1980,** *108*, 223-231.

3. Surrey, T.; Jähnig, F., Refolding and oriented insertion of a membrane protein into a lipid bilayer. *Proc. Natl. Acad. Sci. U. S. A.* **1992,** *89*, 7457-7461.

4. Surrey, T.; Schmid, A.; Jähnig, F., Folding and membrane insertion of the trimeric beta-barrel protein ompF. *Biochemistry* **1996,** *35* (7), 2283-2288.

5. Sanchez, K. M.; Gable, J. E.; Schlamadinger, D. E.; Kim, J. E., Effects of tryptophan microenvironment, soluble domain, and vesicle size on the thermodynamics of membrane protein folding: lessons from the transmembrane protein OmpA. *Biochemistry* **2008,** *47*, 12844-12852.

6. Kang, G. Fluorescence and energy transfer studies of membrane protein folding. University of California, San Diego, 2015.

7. Kleinschmidt, J. H.; den Blaauwen, T.; Driessen, A. J. M.; Tamm, L. K., Outer membrane protein A of *Escherichia coli* inserts and folds into lipid bilyers by a concerted mechanism. *Biochemistry* **1999,** *38* (16), 5006-5016.

8. Larson, B. C.; Pomponio, J. R.; Shafaat, H. S.; Kim, R. H.; Leigh, B. S.; Tauber, M. J.; Kim, J. E., Photogeneration and quenching of tryptophan radical in azurin. *J. Phys. Chem. B* **2015,** *119*, 9438-9449.

9. Liang, J. H., Vibrational and quantum yield studies of deuterated tryptophan radical in azurin. **2017**.

3 Photogeneration of tryptophan radical from the triplet excited state in azurin

3.1 Abstract

Steady-state UV-photolysis experiments of tryptophan in azurin were used to investigate the role of the triplet state in electron transfer within the framework of long-range interprotein electron transport. The triplet absorption and phosphorescence are quenched in the presence of an electron acceptor. The microscopic rate constants for electron transfer (k_{ET}, 8×10^5 sec^{-1}) and deprotonation (k_{deprot}, 4×10^5 sec^{-1}) were calculated from the kinetics of neutral radical formation. The two-photon ionization of tryptophan is also reported. The tryptophan neutral radical can be generated from the triplet state either by electron transfer or photoionization. These results agree with previous reports from phosphorescence quenching experiments.

3.2 Introduction

Long-range electron transfer (ET) is a key component of biological oxidation-reduction reactions. The photosystem II redox chain for example uses several redox intermediates, including an essential tyrosine radical (TyrZ),[1] to generate a charge separation greater than 20 Å with a near unity quantum efficiency[2-3]. Rapid multistep ET via multiple redox centers competes favorably against deactivation processes. In proteins, the side chains of aromatic amino acids (e.g., tyrosine and tryptophan) readily oxidize to form radicals, and thereby these amino acids can act as important mediators in long-range ET. Several studies have shown that aromatic amino acid radicals enhance enzymatic catalysis.[4] Tryptophan radical intermediates have been detected in the mechanisms of cytochrome *c* peroxidase,[5] ribonucleotide reductase,[6] and DNA photolyase.[7] In this report, we focus on investigations of ET reactions involving tryptophan in a model protein azurin.

The type I blue copper protein azurin is a redox partner in the bacterial electron transport chain. Azurin, with a molecular mass of 14 kDa, contains a Trp residue at position 48 buried inside a hydrophobic pocket. Trp48 has been oxidized using a photoactive redox label,[8] and also directly photooxidized in a tyrosine-deficient mutant.[9-10] The oxidation of tryptophan is a stepwise proton-coupled ET (PCET) event producing a cation radical intermediate followed by proton transfer. The resulting tryptophan neutral radical is a long-lived species that is stable for several hours in an oxygen-free environment. This relatively long-term stability has allowed for comprehensive spectroscopic characterization by absorption, resonance Raman, and EPR. Previous work by Larson et al show that the photogeneration of neutral radical is observed only in zinc-substituted azurin and not the native holoprotein of copper-azurin.[10]

The tryptophan fluorescence in copper-metalated holoazurin is noticeably quenched compared to apoprotein and other metal-substituted azurins.[11-16] Petrich et al ascribed the quenching mechanism to electron transfer from the excited tryptophan singlet to the copper center based on measurements of fluorescence lifetimes and theoretical considerations for an intraprotein ET path (k_{ET} ~10^9 sec^{-1}).[14] In addition to fluorescence, the phosphorescence is also quenched in metalated azurins. The quenching of the triplet state may simply reflect short lifetimes of the parent singlet state, but may also reflect ET from the triplet state to the metal.[17]

The zinc-substituted and copper metalated proteins are the subject of the current study; Trp48 in zinc-substituted azurin exhibits relatively long excited singlet (~ns) and triplet (~ms) state lifetimes compared to the copper-metalated system. In holoazurin, the fast intra-protein ET rate between the singlet state and copper center outcompetes intersystem crossing, ISC (k_{isc} ~10^7 sec^{-1}). Hence, when the excited state lifetime is long (k_{fluo} ~10^8 sec^{-1}), the triplet state becomes a reasonable deactivation pathway for the excited singlet state, enabling intra-protein ET from the triplet state to metal center.

The long-lived tryptophan triplet and neutral radical intermediates of azurin offer an extraordinary opportunity to examine the photoinduced oxidation of tryptophan. The focus of this study is to investigate the role of the triplet excited state in the intermolecular ET reaction of azurin. We demonstrate that the quenched phosphorescence in azurin samples containing an electron acceptor is associated with the formation of neutral radical. The neutral radical formation kinetics are modeled to estimate the ISC, ET, and

deprotonation rates. The estimated rates indicate that photooxidation of tryptophan can generally be described by electron transfer from the triplet excited state.

3.3 Materials and Methods

3.3.1 Sample preparation

The recombinant azurin mutant Y72F Y108F from *Pseudomonas aeruginosa* was expressed and purified as described previously[18-19] with modifications.[10] The single-tryptophan apoprotein mutant is referred to as apoAzW48, and the copper(II) holoprotein is Cu^{II}AzW48. The copper-bound holoazurin was demetalated by dialysis against a 500 mM potassium cyanide solution.[20] The apoprotein was stored in 50 mM acetate buffer at pH 4.5, and Zn-substituted azurin was reconstituted by dialysis in 7 mM ZnSO4. The ratio OD_{630}/OD_{280} of the apoprotein and Zn protein were both less than 0.002.

3.3.2 Photolysis and photoionization assays

Samples of apoazurin and Zn(II)-substituted azurin in deoxygenated solutions were exposed to continuous UV light (280 nm), blue light (405 nm), or both wavelengths in the presence and absence of cobalt pentaammine chloride $[Co(NH_3)_5Cl]^{2+}$ acting as an electron acceptor (quencher).

The UV beam from a light emitting diode LED280J OPTAN (Crystal IS, New York) produced excitation at 280 nm with a fwhm of 10 nm as reported by the manufacturer. The average UV output was 0.95 mW. A ball lens expanded the UV beam perpendicular to the probe beam of a scanning spectrophotometer (Shimadzu UV-3600). An 8 x 8 mm squircle of the UV beam overlapped with the probe beam (10 mm height) at their intersection. Photoionizing blue light from a blue-ray laser diode was focused with an aspherical lens and made collinear to the UV beam. The average 405 nm output was 450 mW. A 405-nm long pass filter (Semrock, New York) was placed after the sample, along

the probe light path of the spectrophotometer during photoionization experiments. The long-pass filter was not necessary for UV-only excitation experiments when spectra were acquired above 285 nm.

Samples were excited with UV and blue light along the 2-mm path length of a square 10 x 2 mm quartz cuvette. Absorption spectra were measured along the 10 mm pathlength. Kinetic traces were collected at 0.1 sec intervals at 514 nm. Samples were not stirred during photoexcitation.

3.3.3 Steady-state fluorescence and phosphorescence

Emission spectra of deoxygenated samples were collected at room temperature using a Fluorolog-3 fluorometer (JY-Horiba, California). Samples in a square quartz cell with sample dimensions 10 x 2 mm were excited via the long 10 mm pathlength, and emission was collected through the shorter 2 mm pathlength in a right-angle geometry. Emission and excitation monochromator slits were set to 1.5 nm, and spectra were integrated for 1 sec per step of 1 nm.

3.3.4 Quantum Yield Calculations

The quantum yields for formation of the neutral radical and triplet state (i.e. intersystem crossing) were calculated from the rates of appearance. Using the method of Larson et al with modifications,[10] the quantum yield for neutral radical formation was calculated from the rate of formation of the radical in units of radicals sec^{-1}, and rate of formation of excited singlet state with units of excited W48 sec^{-1} such that,

$$\Phi = \frac{k(\mathrm{W48}\bullet)}{k(\mathrm{W48}^*)} \tag{3.1}$$

In the present study, the linear dependence of the radical formation rate on the incident power was used to calculate the quantum yield. In each experiment, neutral density (ND) filters with values of 0.1, 0.2, 0.3, 0.4, 0.5, 1.0 optical density (OD) were used to attenuate the UV excitation. The incident intensity was also corrected for the absorbance of the sample at 280 nm. The initial rates in units of radical sec^{-1} were determined from the change in absorbance at 514 nm ($\varepsilon_{514\ nm}$ = 2,200 M^{-1} cm^{-1}),[10] and illuminated volume of 8 x 8 x 2 mm.

The quantum yield for triplet formation was determined from the rate of intersystem crossing k_{isc} such that,

$$\Phi_{isc} = \frac{k_{isc}}{k_{isc} + k_r + k_{ic}} = k_{isc}\tau_f \tag{3.2}$$

The observed rate of triplet formation was fit to the following set of differential equations,

$$d[\mathrm{Trp}]/dt = -k_{excit}[\mathrm{Trp}] + (1/\tau_S - k_{isc})[^1\mathrm{Trp}^*] + k_{isc}[^3\mathrm{Trp}] \tag{3.3}$$

$$d[^1\mathrm{Trp}^*]/dt = k_{excit}[\mathrm{Trp}] - (1/\tau_S)[^1\mathrm{Trp}^*] \tag{3.4}$$

$$d[^3\mathrm{Trp}]/dt = k_{isc}[^1\mathrm{Trp}^*] - (1/\tau_T)[^3\mathrm{Trp}] \tag{3.5}$$

The equations 3.3−3.5 are derived from the chemical reaction:

$$\mathrm{Trp} + h\nu \underset{k_r + k_{ic}}{\overset{k_{excit}}{\rightleftharpoons}} {}^1\mathrm{Trp}^* \xrightarrow{k_{isc}} {}^3\mathrm{Trp} \xrightarrow{1/\tau_T} {}^1\mathrm{Trp}$$

The excitation rate is given as

$$k_{excit} = I(\lambda)\sigma_A(\lambda)\Phi(\lambda) \tag{3.6}$$

In this equation $I(\lambda)$ is the photon irradiance in units of photons cm^{-2} sec^{-1}, $\sigma_A(\lambda)$ is the absorption cross-section of the ground state in units of cm^2 $molecule^{-1}$, and $\Phi(\lambda)$ is the probability for generation of W48* per incident photon (assumed to be 1). For the highest absorbed power, the irradiance $I(\lambda)$ was 1.3×10^{15} photons cm^{-2} sec^{-1}. The value for $\sigma_A(\lambda)$ is $\varepsilon(\lambda)\times3.824\times10^{-21}$ and equal to 2.5×10^{-17} cm^2 $molecule^{-1}$ at 280 nm for apoAzW48. The singlet lifetime is defined as $\tau_S \equiv \tau_{fluo} = 1/(k_r + k_{ic} + k_{isc})$, where the deactivation pathways include radiative (r), internal conversion (ic), and intersystem crossing (isc), and the triplet lifetime is $\tau_T = 1/(k'_r + k'_{nr})$, where the deactivation pathways are radiative (r) and non-radiative decay (nr). Using known experimental $(k_{excit}$ and $\tau_T)$ or published values (τ_{fluo}), a fit to the rise in the transient triplet absorption was solved numerically to obtain the rate of intersystem crossing.

3.3.5 Growth and decay of W48•

Absorbance data were converted to fraction of W48 converted to radical via equation 3.7, where $[W48]_0$ is the initial concentration of W48:

$$f_{converted} = \frac{[W48\bullet]}{[W48]_0} \tag{3.7}$$

To gain insight into the ET mechanism, time-resolved absorption data were fit to a set of ordinary differential equations described by the kinetic model in the following scheme:

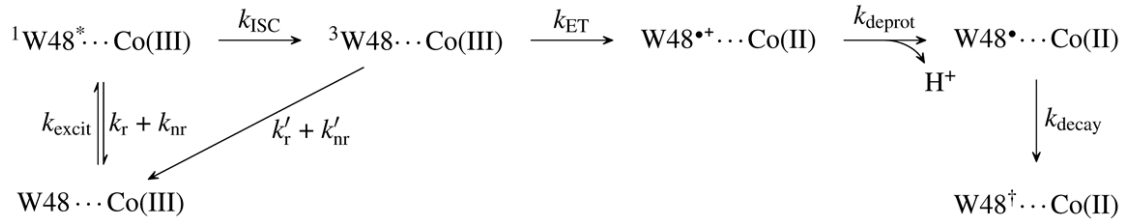

Scheme 3.1 Photooxidation of tryptophan in apoAzW48 in the presence of a Co(III) electron acceptor. The photoexcited trp48 residue is denoted ^{1}W48*, and the triplet as ^{3}W48. The cation and neutral tryptophan radicals are denoted W48$^{\bullet+}$ and W48•, respectively. The unreactive oxidized tryptophan photoproduct is denoted W48†.

The differential equations that are solved for [W48•] are given:

$$\frac{d[\mathrm{W48}]}{dt} = -k_{\mathrm{excit}}[\mathrm{W48}] + (1/\tau_{\mathrm{S}})[^1\mathrm{W48}^*] + (1/\tau_{\mathrm{T}})[^3\mathrm{W48}] \tag{3.8}$$

$$\frac{d[^1\mathrm{W48}^*]}{dt} = k_{\mathrm{excit}}[\mathrm{W48}] - (1/\tau_{\mathrm{S}})[^1\mathrm{W48}^*] - k_{\mathrm{ISC}}[^1\mathrm{W48}^*] \tag{3.9}$$

$$\frac{d[^3\mathrm{W48}]}{dt} = k_{\mathrm{ISC}}[^1\mathrm{W48}^*] - (1/\tau_{\mathrm{T}})[^3\mathrm{W48}] - k_{\mathrm{ET}}[^3\mathrm{W48}] \tag{3.10}$$

$$\frac{d[\mathrm{W48}^{\bullet+}]}{dt} = k_{\mathrm{ET}}[^3\mathrm{W48}] - k_{\mathrm{deprot}}[\mathrm{W48}^{\bullet+}] \tag{3.11}$$

$$\frac{d[\mathrm{W48}^{\bullet}]}{dt} = k_{\mathrm{deprot}}[\mathrm{W48}^{\bullet+}] - k_{\mathrm{decay}}[\mathrm{W48}^{\bullet}] \tag{3.12}$$

$$\frac{d[\mathrm{W48}^{\dagger}]}{dt} = k_{\mathrm{decay}}[\mathrm{W48}^{\bullet}] \tag{3.13}$$

The set of equations were solved numerically with the initial condition $[\mathrm{W48}]_o = 1$ (100% of molecules are in the ground state at t=0), and the rate constants k_{excit}, $k_{nr} + k_r = \frac{1}{\tau_S}$, and $k'_{nr} + k'_r = \frac{1}{\tau_T}$ were fixed: k_{excit} was determined from experimental conditions (see equation 3.6). The four rate constants $k_{ISC}, k_{ET}, k_{deprot}$, and k_{decay}, were determined through least-squares fitting. In this mechanism, $W48^{\dagger}$ is an unreactive photoproduct that is spectroscopically undetectable.

3.3.6 Molecular Dynamics (MD) Simulations

The crystallographic coordinates for apoazurin were obtained from the Protein Data Bank (PDB:1E65), and processed to predict the protonation state of titratable residues at pH 7.2 using the H++ webserver (http://biophysics.cs.vt.edu/H++).[21-23] The system was neutralized with 2 sodium ions, and solvated with 5644 water molecules in a cubic box. The X-ray resolved disulfide bridge between residues 3 and 26 was maintained intact.

The AMBER 2016 package was used to perform GPU-accelerated MD simulations with 2 fs timesteps and periodic boundary conditions using AMBER 2016 force-fields.[24] The system was minimized to correct atomic overlap, and then equilibrated by raising the temperature from 0.1 to 300 K. In equilibration, a pressure of 1 bar was maintained, and temperature was controlled using a Langevin thermostat with a collision frequency of 2 ps. A harmonic restraint of 5.0 kcal/mol $Å^2$ on backbone atoms was gradually removed over the course of 300 ps. A 10 Å cutoff radius was used for range-limited interactions. A set of five independent 100 ns simulations were completed for analysis. The first 5 ns of each

simulation were excluded to ensure equilibration. ET pathways were analyzed using the pathways plug-in for VMD.

3.3.7 Calculation of ET rates

Knowledge of a possible pathway can be used to calculate the ET rate according to Marcus theory treatment of Fermi's golden rule,[25]

$$k_{ET} = \frac{2\pi}{\hbar}\frac{1}{\sqrt{(4\pi\lambda k_B T)}}\exp\left[-\frac{(\lambda + \Delta G^{\circ})^2}{4\lambda k_B T}\right]\left|T_{DA}\right|^2 \tag{3.14}$$

where ΔG° is the driving force, λ is the reorganization energy, k_B is the Boltzmann constant, T is temperature, $\hbar$ is Plank's constant. The coupling term $\left|T_{DA}\right|$ was calculated from the pathways model.[26]

3.4 Results

3.4.1 Phosphorescence quenching

The quenched phosphorescence in protein samples may involve long-range intermolecular electron transfer from the excited triplet state of tryptophan to exogenous electron acceptors.[27-29] To investigate this possibility, we examined the room-temperature phosphorescence of a deoxygenated apoAzW48 sample in the presence of an irreversible electron acceptor, $[Co(NH_3)_5Cl]^{2+}$. Figure 3.1 compares the emission spectra without and with the Co^{3+} electron acceptor. The emission above 400 nm vanishes in the latter. The spectra were normalized to the intensity of the fluorescence maximum (λ_{max} ~308 nm). The inset shows the difference spectrum in which the normalized emission from the sample with Co^{3+} electron acceptor was subtracted from the normalized emission of the sample that lacked Co^{3+}. The remaining difference spectrum reveals a characteristic 0-0 triplet-singlet emission band at ~414 nm.

3.4.2 Triplet-triplet absorption spectrum

To investigate the triplet state of apoAzW48, the absorption spectrum was measured under steady-state UV irradiation. Figure 3.2 (top panel) shows that apoAzW48 in the absence of Co^{3+} develops a light-induced change in absorption. The middle panel displays the difference spectrum in which the pre-photolysis spectrum is subtracted from the 280-nm illuminated spectrum. The difference spectrum displays an absorbance at 450 nm, and a decrease at 630 nm. The absorption at 450 nm is similar to the transient absorption belonging to a triplet-triplet transition as reported by Bent and Hayon.[30] The time-constant for the decay of the absorption is 530 ± 0.10 ms (bottom panel), which is

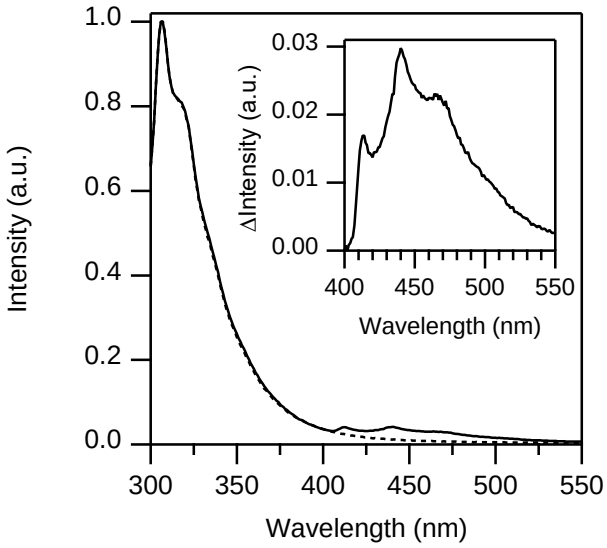

Figure 3.1 Room-temperature emission spectra of 50 μM apoAzW48 in deoxygenated 20 mM phosphate buffer at pH 7.3 in the absence (solid line) and presence (dashed line) of 100 μM $[Co(NH_3)_5Cl]^{2+}$ as electron acceptor. Excitation was at 292 nm. The spectra were normalized for peak fluorescence intensity. A red shoulder 400-500 nm is present in the emission of the sample in the absence of Co^{3+}. The inset shows the difference spectrum of the emission in the absence of Co^{3+} minus the emission from the sample in the presence of Co^{3+}. The remaining difference feature resembles tryptophan phosphorescence.

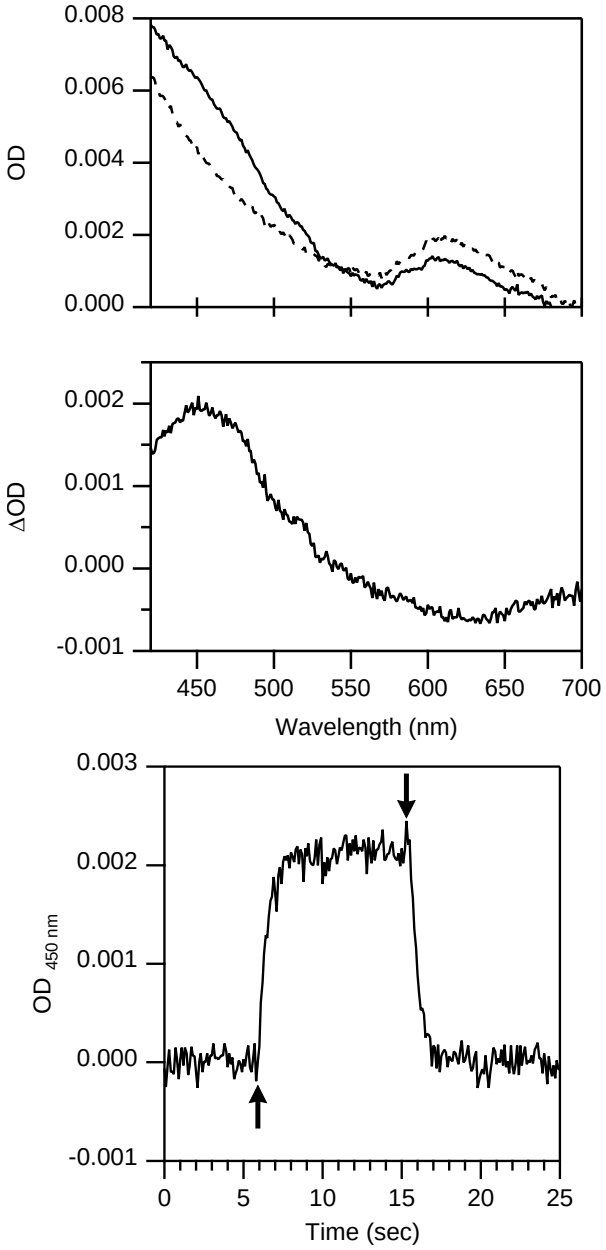

Figure 3.2 Room-temperature triplet-triplet absorption of 250 μM apoAzW48 in deoxygenated 20 mM phosphate buffer at pH 7.3 during UV photolysis. The electron acceptor Co^{3+} is absent from the sample. Top: Absorption spectrum before photolysis (dashed line), and during 280 nm photolysis (solid line). Middle: The difference spectrum after subtraction of the pre-photolysis spectrum from the 280-nm constant-photolysis spectrum. Bottom: The triplet absorption growth and decay measured at 450 nm. The arrows mark the points at which the excitation was turned (↑) on, and (↓) off.

consistent with phosphorescence lifetime measurements. The quantum yield of the triplet and rate for intersystem crossing are discussed below. The slight absorbance bleach at 630 nm is a known feature of copper azurin, and is caused by the reduction of trace amounts of Cu^{II}AzW48 to Cu^{I}AzW48 in the nominal apoAzW48 sample. The small shoulder at 515 nm is a feature of the tryptophan neutral radical, and likely reflects the presence of trace amounts of both Zn^{II}AzW48 and Cu^{II}AzW48; this combination has been shown to generate neutral radical.[10]

3.4.3 Photoionization of the triplet state

The photooxidation of triplet states can also occur via direct light-induced ionization as demonstrated by Codogan and Albrecht.[31] To test the possibility that photoionization of the tryptophan triplet generates neutral radical, apoAzW48 samples were simultaneously irradiated with UV and blue light. The top panel of Figure 3.3. shows absorption spectra before photolysis and during simultaneous photolysis with both UV and blue light. The bottom panel of Figure 3.3 shows the difference spectrum, and indicates an increase in absorption at 488 and 514 nm with a concomitant decrease at 450 nm. The absorption bands at 488 and 514 nm correspond to tryptophan neutral radical. The peaks do not remain after the excitation sources are removed. In contrast, photogenerated neutral radical is stable for hours in Zn(II)AzW48 samples containing Co^{3+}. Figure 3.4 shows the control experiment with only blue light; illumination of the sample with blue light generates no new spectral features and instead, slightly offsets the baseline absorbance.

The formation of neutral radical in apoAzW48 is a surprising result because previous experiments have suggested that only Zn-substituted AzW48 produces neutral radical.

The photoionization of tryptophan triplet in Zn(II)AzW48 samples was also examined. Figure 3.5 shows an increase in the absorption of Zn(II)AzW48 samples in the visible region during UV excitation in the absence of Co^{3+}. The top panel show absorption spectra before photolysis, during photolysis with UV light, and after photolysis. The middle panel presents the difference spectra after subtraction of the prephotolysis spectrum. Difference spectrum (D) shows an increase in the absorbance at 488, 514 nm, and 450 nm. A decrease in absorption at 630 nm is attributed to Cu(II)AzW48 contamination, and the subsequent bleach of Cu(II) to Cu(I). The ratio of the steady-state magnitude in the difference absorbance at 630 to that at 514 nm is about 0.5 in spectrum (E). This ratio indicates that the amount of neutral radical generated during the experiment is greater than the amount of Cu(II)AzW48 reduction by about a factor of about 5 (ε_{630}=5900, ε_{514}=2200), suggesting that other electron acceptors outside of Cu(II)AzW48 must be in the sample. However, this reduced product was not identified. In contrast to apoAzW48, the neutral radical peaks in Zn(II)AzW48 persist after the excitation source is turned off. The bottom panel is a double difference spectrum, and reveals an absorption band centered at 450 nm when the signal from steady-state buildup of radical is removed. This isolated transient absorption resembles the apoAzW48 triplet (see Figure 3.2). The effect of 405 nm excitation on the radical concentration was also investigated. In Figure 3.6, the top panel

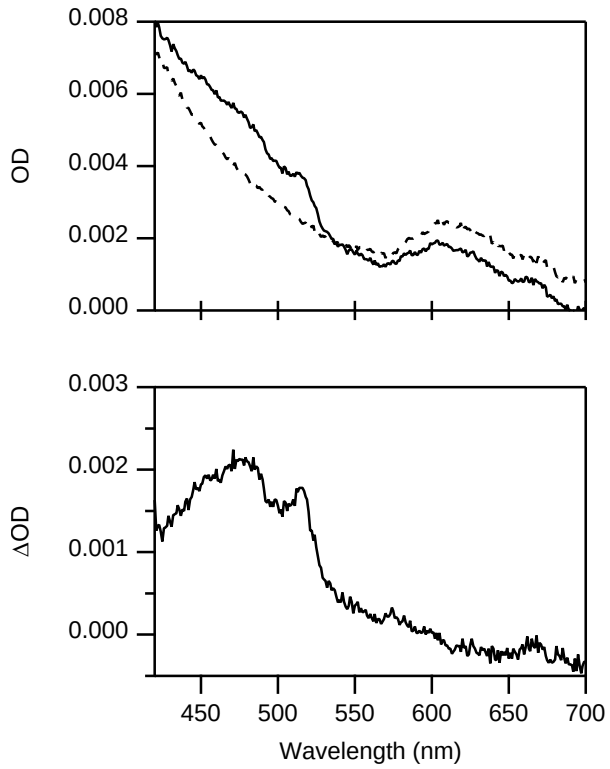

Figure 3.3 Photoionization of apoAzW48 triplet state via 405 nm irradiation. The electron acceptor Co^{3+} is absent from the sample. Sample conditions were the same as in Figure 3.2. Top: absorption spectrum before photolysis (dashed line), and during simultaneous 280 nm and 405 nm photolysis (solid line). Bottom: the difference spectrum after subtraction of the pre-photolysis spectrum from the constant-photolysis spectrum. The difference spectrum shows new peaks indicative of the neutral radical.

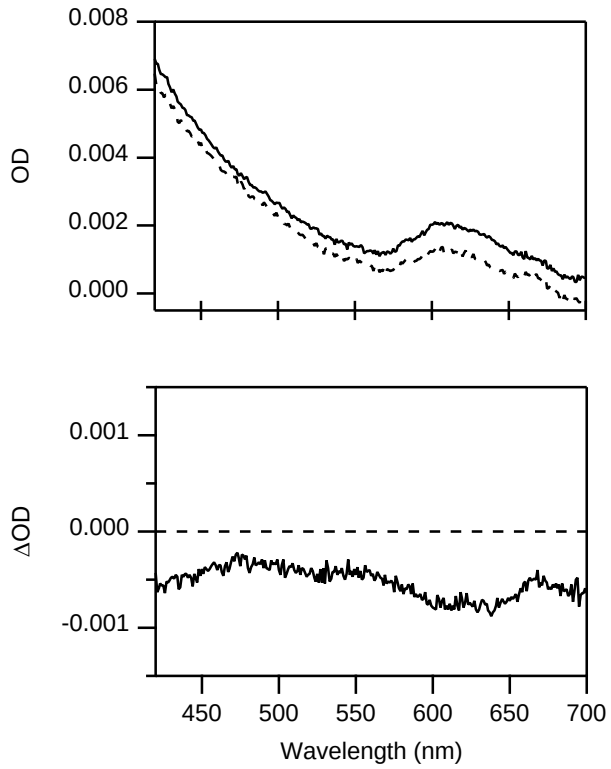

Figure 3.4 Top: Absorption spectrum of apoAzW48 before photolysis (dashed line), and during 405 nm irradiation (solid line). The electron acceptor Co^{3+} is absent from the sample. Sample conditions were the same as in Figure 3.2. Bottom: the difference spectrum after subtraction of the pre-photolysis spectrum from the constant-photolysis spectrum. The difference spectrum shows a baseline offset caused by 405 nm illumination of the sample compartment.

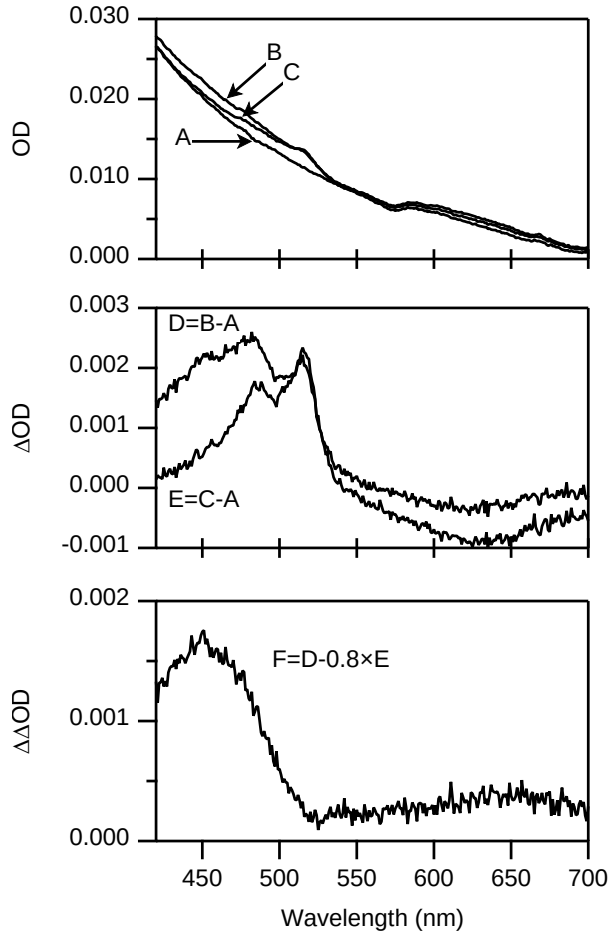

Figure 3.5 Triplet-triplet absorption of 250 μM Zn(II)AzW48 in deoxygenated 20 mM phosphate buffer at pH 7.3 during UV photolysis. The electron acceptor Co^{3+} is absent from the sample. Top: (A) Absorption spectrum before photolysis, (B) during photolysis with 280 nm light, and (C) after photolysis. Middle: Difference spectrum (D) during UV photolysis and (E) after photolysis. Bottom: Double difference spectrum in which 0.8-times graph (E), the neutral radical spectrum, was subtracted from (D), transient absorption spectrum, to generate (F). The double difference spectrum resembles the triplet-triplet absorption of tryptophan.

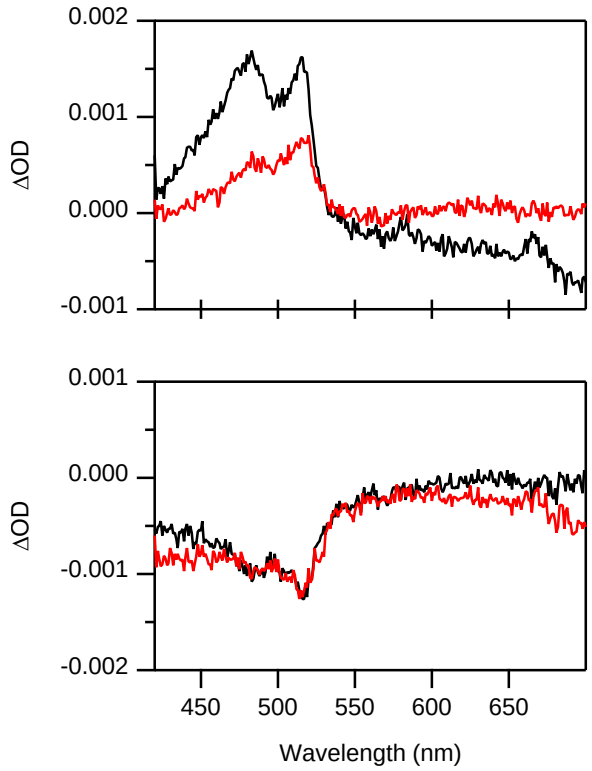

Figure 3.6 Photoionization of triplet Zn(II)AzW48 to neutral radical with 405 nm irradiation. The electron acceptor Co^{3+} is absent from the sample. Top: Difference absorption spectrum (black) during simultaneous 280 nm and 405 nm photolysis, and (red) after photolysis. Bottom. The sample represented by the red spectrum from the top panel (i.e. the steady-state buildup of neutral radical) was considered to be a subsequent (second) pre-photolysis spectrum, and was further illuminated with 405 nm light. The black graph in the bottom panel is the difference spectrum in which the second pre-photolysis spectrum was subtracted from the 405-nm constant-photolysis spectrum, and represents the bleach caused by 405-nm illumination of steady-state radical. After the 405-nm light was turned off, a final difference spectrum was generated to illustrate that there was a steady-state, irreversible loss of radical with 405 nm excitation. See text for more details.

indicates that simultaneous UV and 405 nm excitation increases the absorbance at 488 and 514 nm. This finding is consistent with the results in apoAzW48, and suggests that greater quantity of neutral radical is generated in the simultaneous presence of UV and 405 nm light. The effect of 405 nm light on the radical concentration was also investigated. The bottom panel shows that exposure of a small amount of neutral radical to only 405 nm light decreases the absorption at 488 and 514 nm, indicating that 405 nm was able to successfully bleach the radical.

3.4.4 Photogeneration of neutral radical.

The generation of neutral radical in apoAzW48 in the presence of Co^{3+} quencher was investigated. This experiment was motivated by the fact that in the presence of the electron acceptor $[Co(NH_3)_5Cl]^{2+}$, relatively stable neutral radical is generated from UV excitation of tryptophan in Zn(II)AzW48.[10] In Figure 3.7, the top panel shows the photooxidation kinetics measured at 514 nm during constant UV excitation. The absorbance of the sample was measured (A) before, (B) during, and (C) after photolysis. The absorption spectrum during constant illumination displays neutral radical features at 488 and 514 nm (bottom panel of Figure 3.7). The kinetics of the formation of the radical as a function of absorbed photon flux was investigated. In Figure 3.8, the left panel shows the power dependence of the absorbance kinetics at 514 nm. The temporal response of the inflection in the data depends on the rate of ground state depletion (fastest, 0.035 sec^{-1}, see below), and the observation of the inflection suggests that a non-productive product is formed (e.g. decay of the neutral radical, see below). In the right panel, the decay curves were fit to monoexponential functions, and revealed a time constant $\tau_{decay} = 0.025\ sec^{-1}$ that

is independent of the absorbed photon flux, and is significantly shorter than the lifetime of the neutral radical reported for Zn(II)AzW48 (~7 hrs).[10]

The quantum yield for generation of the neutral radical was calculated from the power-dependence data. The top panel of Figure 3.9 shows linear least-squares fits to the kinetic traces to determine the initial rates of radical formation. These initial slopes were converted to rate of formation of the radical using the published molar absorptivity of 2,200 M^{-1} cm^{-1}.[10] In the bottom panel, the quantum yield is calculated from the graph of initial rates of radical formation (radicals sec^{-1}) and absorbed photon flux (photon sec^{-1}) based on linear regression. The quantum yield for neutral radical formation of photoexcited apoAzW48 in the presence of Co^{3+} is 0.009 ± 0.003. This value is much lower than the radical yield in Zn(II)AzW48 (0.080 ± 0.002) and Zn(II)AzWT (0.045 ± 0.004) in the presence of the same electron acceptor.[10]

3.4.5 Electron tunneling pathway

The curves with the second, third, and fourth highest excitations are shown in Figure 3.9 are shown in the left panel of Figure 3.10; these curves represent the highest incident powers. The curve with the highest inflection may include photoproduct absorption, and thus was not included in the fits.

The data were fit to equations 3.8 to 3.13 (Scheme 3.1) The rate constants k_{excit}, $k_r + k_{nr}$, and $k'_r + k'_{nr}$ were fixed: k_{excit} was determined from experimental conditions (see equation 3.6), with values of 0.027 s^{-1}, 0.024 s^{-1}, 0.017 s^{-1}, for curves B, C, and D, respectively; $k_r + k_{nr}$ is 2.0×10^8 s^{-1};[32-33] and $k'_r + k'_{nr}$ is 2 s^{-1} (from Figure 3.8). The three

rate constants k_{ISC}, k_{ET}, k_{deprot}, and k_{decay} were determined through least-squares fitting, and the results from the fits are shown in Table 3.1. The residuals in the top panel of Figure 3.10 suggest a questionable fit to the data after the point of inflection, but generally the amplitude is described well. Simulated results for all excitation rates are shown in Figure 3.11.

The ET rate predicted from fitting the data to Scheme 3.1 was compared to a theoretical result based on the pathways model for electron transfer in proteins.[26] As illustrated in Figure 3.12, the positively charged cobalt may bind onto a negative patch of the protein near His 83, such as near residues Asp 71 and Asp 76. One viable tunneling pathway to this patch is shown below in Scheme 3.2 (and shown in Figure 3.12). The pathway includes 10 covalent bonds, one through-space jump, and one through-space step to an external electron acceptor. A distance of ~18 Å between the donor and acceptor was estimated from the apoprotein X-ray crystal structure (1E65) coordinates, and counting an additional through-space step and covalent bond.

$$\text{W48 indole} \xrightarrow{5C} \text{O W48} \xrightarrow[3.2\text{Å}]{TS} \text{C}_{\alpha}\ \text{His 83} \xrightarrow{4C} \text{N}_{\epsilon 2}\ \text{His 83} \xrightarrow[3.5\text{Å}]{TS} \text{N (amine) of acceptor} \xrightarrow{1C} \text{Co}^{III}\ \text{(metal atom)}$$

Scheme 3.2 Intermolecular ET pathway in azurin

The average electronic coupling from five 95 ns MD simulations was calculated using the pathways plugin for VMD.[34-35] An additional 3.5 Å through-space step and covalent bond were included in the pathway, which led to a value for $|T_{DA}|$ of 3.5×10^{-5} eV. Other input values were the reorganization energy $\lambda = 0.3$ eV, driving force $\Delta G° = 0$ eV,

and temperature T = 300 K. The distance-based decay factor β reflects the barrier to through space tunneling in the pathways model. A decay of 1.1 $Å^{-1}$ was chosen based on theory and experiment, including estimates from ET in azurin.[36-37] The predicted maximum ET rate from W48 to the acceptor based on Scheme 3.2 is ~2×10^{6} sec^{-1}.

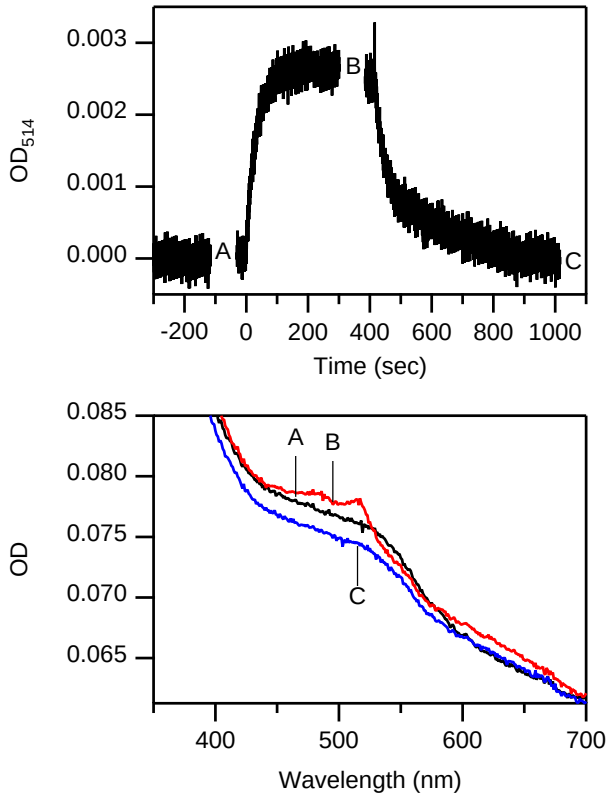

Figure 3.7 Photooxidation of 75 μM apoAzW48 in the presence of 125 μM $[Co(NH_3)_5Cl]^{2+}$ as electron acceptor. Top: the absorption kinetics were measured at 514 nm, and interrupted to measure the absorption spectrum before photolysis (Bottom panel A, black), during photolysis (Bottom panel B, red), and after photolysis (Bottom panel C, blue).

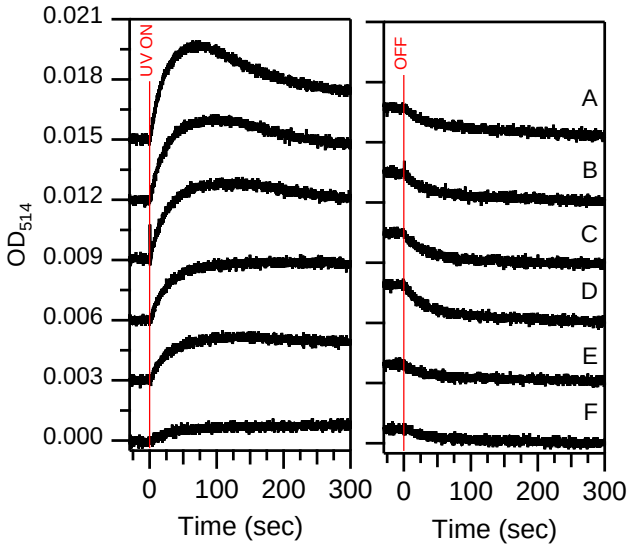

Figure 3.8 Photooxidation of 75 μM apoAzW48 in the presence of 150 μM $[Co(NH_3)_5Cl]^{2+}$ as a function of absorbed photon flux. The left panel shows the rise of the absorption upon turning on the UV light. The right panel shows the decay after the light source is turned off. An absorbtion spectrum was taken at the end of the growth kinetics. The maximum photon flux without attenuation was 1.3×10^{15} photon sec^{-1} (0.95 mW). Inset labels A, B, C, D, E, F correspond to absorbed photon fluxes: 9.0×10^{14}, 7.0×10^{14}, 6.0×10^{14}, 4.3×10^{14}, 3.3×10^{14}, 1.1×10^{14} photon sec^{-1}, respectively The average decay of the signal on the right panel was $k_{decay} = 1/\tau_{decay} = 0.025$ sec^{-1}.

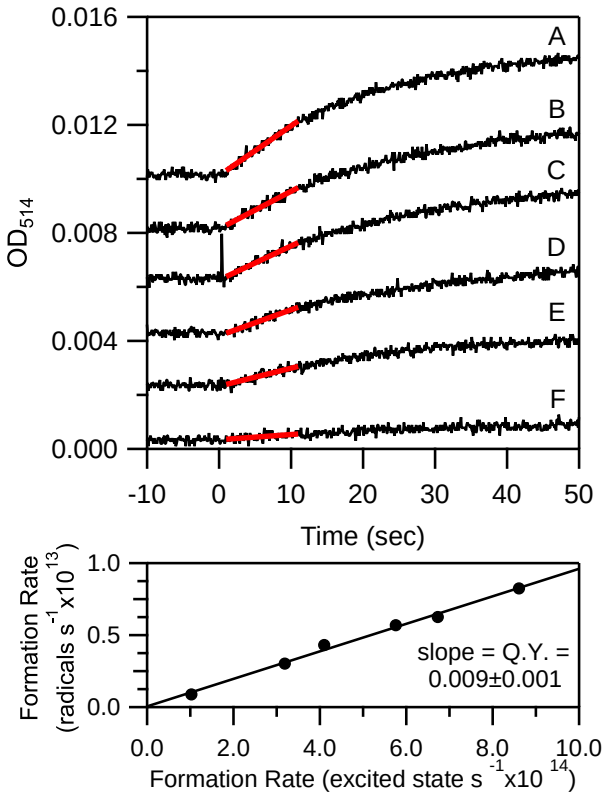

Figure 3.9 Determination of the neutral radical quantum yield for apoAzW48. Top: Change in absorbance at 514 nm (same curves as Figure 3.8), and (red) linear least squares fits. Inset labels A, B, C, D, E, F correspond to absorbed photon flux: 9.0×10^{14}, 7.0×10^{14}, 6.0×10^{14}, 4.3×10^{14}, 3.3×10^{14}, 1.1×10^{14} photon sec^{-1}, respectively Bottom: Graph of formation rate of radicals per second as a function of absorbed photon flux. The quantum yield was determined from the linear regression slope.

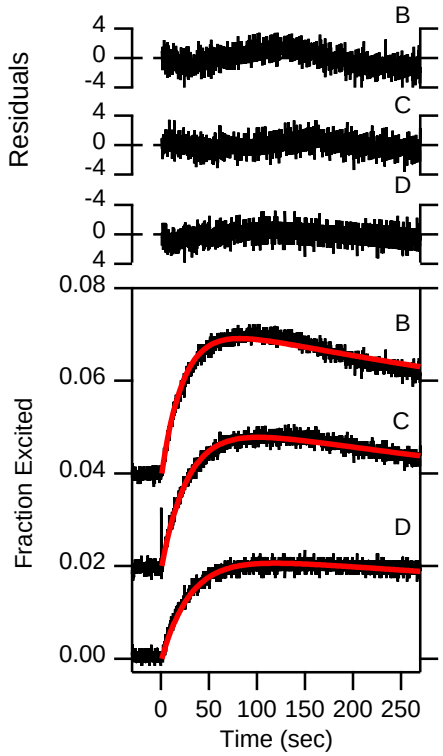

Figure 3.10 The curves with the largest inflections from Figure 3.9 (curves B, C, and D) were regraphed as fraction of W48 converted to radical, and fit to kinetic scheme 3.1 (shown in red). Top panel shows residuals. See text for details.

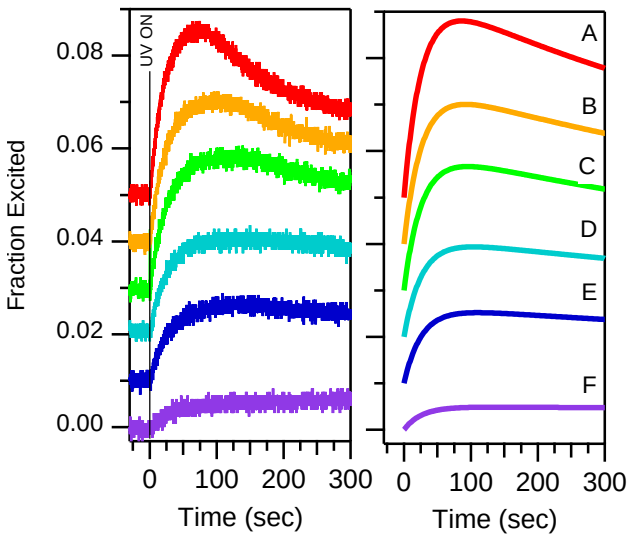

Figure 3.11 Left: Experimental results. Right: Simulation of fraction of W48 converted to neutral radical based on Scheme 3.1, and average rates from Table 3.1. The indicated excitation rates correspond to experimental values in Figure 3.8, and are 0.035, 0.027, 0.024, 0.017, 0.013, and 0.004 sec^{-1} for graphs A, B, C, D, E, and F, respectively. See text for details.

Table 3.1 Fit results for the triplet as the photooxidation intermediate

Curve	k_{excit} (10^{-2} s^{-1})	k_{ISC} (10^{7} s^{-1})	k_{ET} (10^{5} s^{-1})	k_{deprot} (10^{5} s^{-1})	k_{decay} (10^{-2} s^{-1})
A	3.5	–	–	–	–
B	2.7	1.1	8	2	4.4
C	2.4	1.0	8	4	3.6
D	1.7	0.9	8	4	3.3
E	1.3	–	–	–	–
F	0.4	–	–	–	–
	Average	1.0	8	4	3.8

Notes: $\tau_S \equiv \tau_{fluo} = \frac{1}{k_r + k_{nr}} = 5.0$ ns; $\tau_T = \frac{1}{k'_r + k'_{nr}} = 0.5$ s

3.5 Discussion

Steady-state UV photoexcitation of tryptophan in apoazurin samples provides insight into the role of the triplet state in long-range ET reactions. The results suggest that the triplet state is associated with neutral radical formation. The quenching of apoazurin phosphorescence in the presence of an electron acceptor correlates with the photogeneration of neutral radical. Tryptophan radical is observed only when phosphorescence is quenched. These results agree with previous interpretations on the role of ET as a mechanism to quench phosphorescence in proteins, and advance the role of the triplet state as a precursor in interprotein and long-range electron transport.

3.5.1 Phosphorescence quenching

The room-temperature phosphorescence of deoxygenated protein samples is a natural, widespread property.[38] Proteins with buried, solvent inaccessible tryptophan residues typically exhibit long-lived phosphoresce on the order of 10^{-6} to 10^{0} sec. The triplet lifetime of apoAzW48 has been reported between 270[17], 400[38], and 600[39] ms. This relatively long lifetime is consistent with the buried nature of W48. The long decay time of the tryptophan triplet makes the photoexcited triplet state a favorable electron donor in long-range ET reactions. Support for ET-based quenching of phosphorescence in apoAzW48 is reported. The presence of the electron acceptor Co^{3+} eliminated the phosphorescence below our detection limit. A pathway model prediction estimates a maximum tunneling rate constant through the protein backbone of 2×10^{6} sec^{-1}. This predicted ET rate is consistent with the experimentally determined value of 8×10^{5} sec^{-1} (Table 3.1). Therefore, it follows that quenching of the phosphorescence of the buried tryptophan residue in apoAzW48 is due to an ET mechanism.[28-29] A previously reported

linear dependence of phosphorescence quenching rates with concentration of acceptor suggests that ET quenching can be the dominant mechanism for deactivation of the triplet state.[28] One other possible deactivation mechanism is triplet-triplet energy transfer based on Dexter exchange. However, Dexter exchange requires relatively close distances between electron donor and acceptor because the wavefunctions must overlap.[40] This overlap is unlikely in our experiments because the Co^{3+} quencher is presumably external to the protein and more than 10 Å from W48. Förster resonance energy transfer (FRET) is also ruled out because the triplet-to-singlet transition is formally not allowed, and there is no spectral overlap between donor and acceptor. The molar absorptivity of $[Co(NH_3)_5Cl]^{2+}$ in the region of W48 phosphorescence (400-550 nm) is also negligible (~0 M^{-1} cm^{-1}) relative to that of Trp (ε_{292}=5800 M^{-1} cm^{-1}).

3.5.2 Triplet absorption

The T_1-T_n absorption of UV-photoexcited apo- and Zn(II)AzW48 samples was examined under steady-state conditions. In the absence of quencher, a dominating feature of the difference spectrum in apoAzW48 and ZnAzW48 samples is the triplet absorption (Figures 3.2 and 3.5). The steady-state concentration of triplet can be estimated *a priori* from the ground state depletion $(h\nu + S_0 \rightarrow S_1)$. The rate of triplet production can be determined by considering the quantum yield for intersystem crossing in the expression for k_{excit} described by equation 3.6 above. In these experiments, a 1 mW beam of 280 nm light was expanded to a 0.8 cm square spot on the sample. The rate of triplet production based on this power is 0.0028 sec^{-1} (I=1.1×10^{15} photons cm^{-2} sec^{-1}, ε_{280}=6800 M^{-1} cm^{-1}, OD_{2mm}=0.3, and φ=0.10). As described by Mathies et al, [41] the photoalteration parameter

$F = \tau_T k_{\text{excit}}$ can be used calculate the fraction excited, and F is 0.14% (τ_T =0.50 sec) in this case. A sample concentration of 250 μM under steady state excitation creates a triplet concentration of 0.35 μM, and is expected to generate an absorption of 1.4 mOD (ε_{460}=5000 M^{-1} cm^{-1})[42]. The calculations from this feasibility study are consistent with the magnitude of the observed absorption at 450 nm.

The k_{isc} value of 3×10^7 sec^{-1} calculated from a fit to the observed rate of triplet formation (Figure 3.2) agrees with published transient absorption quenching experiments. Published results of 5×10^7 sec^{-1} for NATA and Trp, but can range from 2.1–7.6×10^7 sec^{-1} depending on substituents.[43] The quantum yield of 0.15 is identical to the value for NATA and Trp reported by Chen et al. in aqueous solution.[43] These result support the observed absorption as triplet state in origin.

3.5.3 Two-photon ionization of the triplet

A second beam of 405 nm excitation transforms the triplet absorption of apoAzW48 samples into a spectrum with absorption peaks at 488 and 514 nm. These absorption bands correspond to the one electron oxidized neutral radical intermediate. A similar decrease in lifetime of the phosphorescence and triplet absorption of N, N, N', N'-tetramethyl-p-phenylenediamine (TMPD), which was explained by a two-photon processes involving the triplet state.[31, 44] The time constant for the phosphorescence decay of L-Trp in rigid solutions is also sensitive to biphotonic ionization.[45] In our two beam experiments, photoionization of tryptophan generates oxidized radical intermediates, and we conclude that neutral radical is generated directly from the triplet state.

The triplet is readily ionized when the energy of the photon exceeds the ionization threshold. The triplet energy is 3.0 eV above the ground state (phosphorescence emission max of ~440 nm), and the second excited triplet state lies at about 5.86 eV (T_1-T_n absorption max of ~450 nm). The gas phase ionization potential of L-Trp is <7.5 eV.[46] Solvent stabilization of the products may decrease the ionization potential by as much as 2.5 eV[47] and reasonable one-photon ionization of aqueous tryptophan and model compounds has been reported with 266 nm in the solvated electron community. [48] It is reasonable to expect that excitation into the continuum may lead to ionization. Due to the short lifetime of the cation radical <μs, only the neutral radical is expected to be observed under steady-state conditions.

3.5.4 ApoAzW48• quantum yield

Samples containing $[Co(NH_3)_5Cl]^{2+}$ generate neutral radical during UV excitation. The radical in apoAzW48 has not been reported until now. The species apoAzW48• is surprisingly less stable than its counterpart Zn(II)AzW48• with the same electron acceptor Co^{3+}; the lifetimes are 40 sec and ~6 hrs, respectively. The quantum yield for radical formation, as assessed by the initial slopes, is 0.9 %. The maximum yield reported for Zn(II)AzW48 is 8%.[10] This is a surprising result given that the backbone atom RMSD for apo and Zn-substituted azurin from X-ray diffraction coordinates is less than 0.5 %. It appears that differences in dynamics may affect radical stability and formation.

3.5.5 Neutral radical kinetics

A kinetic argument can be made that if the rate of ET (k_{ET}) is slower than the rate of the singlet excited state lifetime ($k_r + k_{nr}$), then oxidation will preferentially occur from

the long-lived triplet state. The rate of ET from the photoexcited state is estimated from the neutral radical formation kinetics measured at 514 nm as 8×10^5 sec^{-1}. It should be noted the decay (k_{decay}) of the neutral radical produces a non-productive product that is not spectroscopically identifiable. The data are consistent with a model that involves stepwise electron transfer followed by deprotonation. The timescale for electron transfer is on the order of μs, and is slower than the excited singlet state lifetime of 5 ns.[32] The triplet state lifetime is reported as 230–600 ms,[17, 38-39] and easily quenched by an ET mechanism. The rate constant for deprotonation of the cation radical is estimated as k_{deprot} of 4×10^5 s^{-1}, which is within roughly an order of magnitude of previous estimates of 5×10^6 s^{-1}.[9]

3.5.6 Electron transfer pathway

The kinetic model in Scheme 3.1 requires pre-association of the positively charged quencher molecule with the protein. Since the pI of apoazurin from *P. aeruginosa* is <7,[33, 39] the surface charge is acidic as illustrated in Figure 3.12. One proposed binding spot is near His 83.[10] The electron transfer rate constant for the pathway shown in Figure 3.12 concurs with estimates from the rate of neutral radical formation within a factor two. A second pathway to a disulfide bridge also exists. However, the phosphorescence was unquenched in the absence of external acceptor. Therefore, it is unlikely that the disulfide acts as an intramolecular electron acceptor. The ET pathway from W48 to His presented here awaits investigation by protein modifications. A glutamine mutation at position 83 is expected to produce a null result with respect to the ET rate constant because the hydrogen-bonding properties of glutamine and histidine re similar, while mutation from histidine to

glutamate may attract cobalt and enhance ET. An alanine or lysine residue may turn off this pathway completely by preventing Co(II) from binding.

3.6 Conclusions

The transient and steady-state buildup of tryptophan neutral radical and the triplet state have been observed in apoazurin samples during constant illumination. The triplet state was generated under constant UV excitation, as evidenced by spectroscopic signature of the T1-Tn absorption at room-temperature. In the presence of simultaneous UV and blue excitation, a two-photon ionization process generated neutral radical in the absence and presence of an electron acceptor (Co^{3+}), with greater yield of formation of radical in the presence of an electron acceptor. The observation of phosphorescence quenching of apoAzW48 in the presence of Co^{3+} suggests ionization proceeds primarily from the triplet state. The kinetics of radical formation reveal a quantum yield of 0.9% for the photogeneration of radical, and allow for the examination of a previously proposed ET pathway. The results from this study suggest that the long lifetime of the tryptophan triplet state in proteins makes it possible to overcome kinetic barriers in long-range electron transport.

3.7 Acknowledgements

Chapter 3 is in preparation for submission: Lopez-Peña, I, Kim, J. E, “Photogeneration of tryptophan radical from the triplet excited state in azurin”. The dissertation author was the primary investigator and author of this paper.

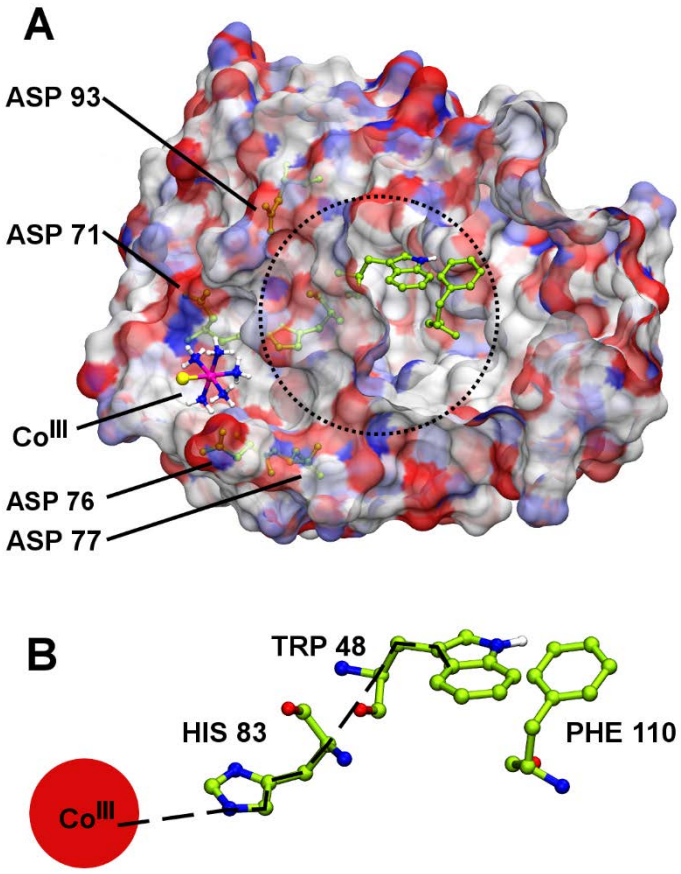

Figure 3.12 (A) The proposed binding site for Co^{3+} and nearby negatively charged residues (within 10 Å). The surface charges are shown in red (negative) and blue (positive). (B) Isolated view of the region near W48, and proposed electron transfer path from trp48 to external electron acceptor Co^{3+} from panel A (dashed line).

3.8 References

1. Barry, B. A.; Babcock, G. T., Tyrosine radicals are involved in the photosynthetic oxygen-evolving system. *Proc. Natl. Acad. Sci. U. S. A.* **1987,** *84*, 7099-7103.

2. Wientjes, E.; van Amerongen, H.; Croce, R., Quantum yield of charge separation in photosystem II: functional effect of changes in the antenna size upon light acclimation. *J. Phys. Chem. B* **2013,** *117* (38), 11200-11208.

3. Croce, R.; van Amerongen, H., Light-harvesting and structural organization of photosystem II: from individual complexes to thylakoid membrane. *J. Photoch. Photobio. B* **2011,** *104* (1-2), 142-153.

4. Stubbe, J.; van der Donk, W. A., Protein radicals in enzyme catalysis. *Chem. Rev.* **1998,** *98*, 705-762.

5. Huyett, J. E.; Doan, P. E.; Gurbiel, R.; Houseman, A. L. P.; Sivaraja, M.; Goodin, D. B.; Hoffman, B. M., Compound ES of cytochrome *c* peroxidase contains a trp π-cation radical: characterization by CW and pulsed Q-band ENDOR spectroscopy. *J. Am. Chem. Soc.* **1995,** *117*, 9033-9041.

6. Lendzian, F.; Sahlin, M.; MacMillan, F.; Bittl, R.; Fiege, R.; Pötsch, S.; Sjöberg, B. M.; Gräslund, A.; Lubitz, W.; Lassmann, G., Electronic structure of neutral tryptophan radicals in ribonucleotide reductase studied by EPR and ENDOR spectroscopy. *J. Am. Chem. Soc.* **1996,** *118* (34), 8111-8120.

7. Aubert, C.; Vos, M. H.; Mathis, P.; Eker, A. P. M.; Brettel, K., Intraprotein radical transfer during photoactivation of DNA photolyase. *Nature* **2000,** *405*, 586-590.

8. Shafaat, H. S.; Leigh, B. S.; Tauber, M. J.; Kim, J. E., Resonance Raman characterization of a stable tryptophan radical in an azurin mutant. *J. Phys. Chem. B* **2009,** *113*, 382-388.

9. Shafaat, H. S.; Leigh, B. S.; Tauber, M. J.; Kim, J. E., Spectroscopic comparison of photogenerated tryptophan radicals in azurin: effects of local environment and structure. *J. Am. Chem. Soc.* **2010,** *132*, 9030-9039.

10. Larson, B. C.; Pomponio, J. R.; Shafaat, H. S.; Kim, R. H.; Leigh, B. S.; Tauber, M. J.; Kim, J. E., Photogeneration and quenching of tryptophan radical in azurin. *J. Phys. Chem. B* **2015,** *119*, 9438-9449.

11. Finazzi-Agro, A.; Rotilio, G.; Avigliano, L.; Guerrieri, P.; Boffi, V.; Mondovi, B., Environment of copper in Pseudomonas fluorescens azurin: fluorometric approach. *Biochemistry* **1970,** *9* (9), 2009-2014.

12. Finazzi-Agro, A.; Giovagnoli, C.; Avigliano, L.; Rotilio, G.; Mondovi, B., Luminescence quenching in azurin. *Eur. J. Biochem.* **1973,** *34*, 20-24.

13. Szabo, A. G.; Stepanik, T. M.; Wayner, D. M.; Young, N. M., Conformational heterogeneity of the copper binding site in azurin. *Biophys. J.* **1983,** *41*, 233-244.

14. Petrich, J. W.; Longworth, J. W.; Fleming, G. R., Internal motion and electron transfer in proteins: a picosecond fluorescence study of three homologous azurins. *Biochemistry* **1987,** *26*, 2711-2722.

15. Hutnik, C. M.; Szabo, A. G., A time-resolved fluorescence study of azurin and metalloazurin derivatives. *Biochemistry* **1989,** *28* (9), 3935-3939.

16. Turoverov, K. K.; Kurnetsova, I. M.; Zaitsev, V. N., The environment of the tryptophan residue in Pseudomonas aeruginosa azurin and its fluorescence properties. *Biophys. Chem.* **1985,** *23*, 79-89.

17. Klemens, F. K.; Mcmillin, D. R., Room-temperature phosphorescence from azurin derivatives. Phosphorescence quenching in oxidized native azurin. *Photochem. Photobio.* **1992,** *55* (5), 671-676.

18. Miller, J. E.; Gradinaru, C.; Crane, B. R.; Di Bilio, A. J.; Wehbi, W. A.; Un, S.; Winkler, J. R.; Gray, H. B., Spectroscopy and reactivity of a photogenerated tryptophan radical in a structurally defined protein environment. *J. Am. Chem. Soc.* **2003,** *125*, 14220-14221.

19. Di Bilio, A. J.; Crane, B. R.; Wehbi, W. A.; Kiser, C. N.; Abu-Omar, M. M.; Carlos, R. M.; Richards, J. H.; Winkler, J. R.; Gray, H. B., Properties of photogenerated tryptophan and tyrosyl radicals in structurally characterized proteins containing rhenium(I) tricarbonyl diimines. *J. Am. Chem. Soc.* **2001,** *123*, 3181-3182.

20. Lancaster, K. M.; Farver, O.; Wherland, S.; Crane, E. J.; Richards, J. H.; Pecht, I.; Gray, H. B., Electron Transfer Reactivity of Type Zero Pseudomonas aeruginosa Azurin. *J. Am. Chem. Soc.* **2011,** *133* (13), 4865-4873.

21. Gordon, J. C.; Myers, J. B.; Folta, T.; Shoja, V.; Heath, L. S.; Onufriev, A., H++: a server for estimating pKas and adding missing hydrogens to macromolecules. *Nucleic Acids Res.* **2005,** *33*, W368-W371.

22. Myers, J.; Grothaus, G.; Narayanan, S.; Onufriev, A., A simple clustering algorithm can be accurate enough for use in calculations of pKs in macromolecules. *Proteins* **2006,** *63* (4), 928-938.

23. Anandakrishnan, R.; Aguilar, B.; Onufriev, A. V., H++ 3.0: automating pK prediction and the preparation of biomolecular structures for atomistic molecular modeling and simulations. *Nucleic Acids Res.* **2012,** *40*, W537-W541.

24. Case, D. A.; Betz, R. M.; Cerutti, D. S.; Cheatham, T. E.; Darden, T. A.; Duke, R. E.; Giese, T. J.; Gohlke, H.; Goetz, A. W.; Homeyer, N.; Izadi, S.; Janowski, P.; Kaus, J.; Kovalenko, A.; Lee, T. S.; LeGrand, S.; Li, P.; Lin, S.; Luchko, T.; Luo, R.; Madej, B.; Mermelstein, D.; Merz, K. M.; Monard, G.; Nguyen, H.; Nguyen, H. T.; Omelyan, I.; Onufriev, A.; Roe, D. R.; Roitberg, A.; Sagui, C.; Simmerling, C. L.; Botello-Smith, W. M.; Swails, J.; Walker, R. C.; Wang, J.; Wolf, R. M.; Wu, X.; Xiao, L.; Kollman, P. A., AMBER 2016. *University of California, San Francisco* **2016**.

25. Marcus, R. A., On the theory of oxidation-reduction reactions involving electron transfer. I*. *J. Phys. Chem.* **1956,** *24*, 966-978.

26. Beratan, D. N.; Betts, J. N.; Onuchic, J. N., Protein electron transfer rates set by the bridging secondary and tertiary structure. *Science* **1991,** *252*, 1285-1288.

27. Calhoun, D. B.; Englander, S. W.; Wright, W. W.; Vanderkooi, J. M., Quenching of room temperature protein phosphorescence by added small molecules. *Biochemistry* **1988,** *27*, 8466-8474.

28. Mersol, J. V.; Steel, D. G.; Gafni, A., Quenching of tryptophan phosphorescence in *Escherichia coli* Alkaline phosphoatase by long-range transfer mechanisms to external agents in the rapid-diffusion limit. *Biochemistry* **1991,** *30* (3), 668-675.

29. Dadak, V.; Vanderkooi, J. M.; Wright, W. W., Electron transfer from excited tryptophan to cytochrome *c*: mechanism of phosphorescence quenching? *Biochim. Biophys. Acta* **1992,** *1100*, 33-39.

30. Bent, D. V.; Hayon, E., Excited state chemistry of aromatic amino acids and related peptides. III. Tryptophan. *J. Am. Chem. Soc.* **1975,** *97* (10), 2612-2619.

31. Cadogan, K. D.; Albrecht, A. C., Detailed studies of a one-electron, two-photon ionization in a rigid organic solution at 77 K. *J. Phys. Chem.* **1968,** *72* (3), 929-944.

32. Hansen, J. E.; Longworth, J. W.; Fleming, G. R., Photophysics of metalloazurins. *Biochemistry* **1990,** *29*, 7329-7338.

33. Hutnik, C. M.; Szabo, A. G., Confirmation that multiexponential fluorescence decay behavior of holoazurin originates from conformational heterogeneity. *Biochemistry* **1989,** *28* (9), 3923-3934.

34. Humphrey, W.; Dalke, A.; Schulten, K., VMD - Visual Molecular Dynamics. *J. Molec. Graphics* **1996,** *14*, 33-38.

35. Balabin, I. A.; Hu, X.; Beratan, D. N., Exploring biological electron transfer pathway dynamics with the Pathways plugin for VMD. *J. Comput. Chem.* **2012,** *33* (8), 906-10.

36. Jones, M. L.; Kurnikov, I. V.; Beratan, D. N., The nature of tunneling pathway and average packing density models of protein-mediated electron transfer. *J. Phys. Chem. A* **2002,** *106*, 2002-2006.

37. Gray, H. B.; Winkler, J. R., Long-range electron transfer. *Proc. Natl. Acad. Sci. U. S. A.* **2005,** *102* (10), 3534-3539.

38. Vanderkooi, J. M.; Calhoun, D. B.; Englander, S. W., On the prevalence of room-temperature protein phosphorescence. *Science* **1987,** *236*, 568-569.

39. Strambini, G. B.; Gabellieri, E., Phosphorescence from trp-48 in azurin: influence of Cu(II), Cu(I), Ag(I), and Cd(II) at the coordination site. *J. Phys. Chem.* **1991,** *95*, 4352-4356.

40. Dexter, D. L., A theory of sensitized luminescence in solids. *J. Chem. Phys.* **1953,** *21* (5), 836-850.

41. Mathies, R.; Oseroff, A. R.; Stryer, L., Rapid-flow resonance Raman spectroscopy of photolabile molecules: rhodopsin and isorhodopsin. *Proc. Natl. Acad. Sci. U. S. A.* **1976,** *73* (1), 1-5.

42. Volkert, W. A.; Kuntz, R. R.; Ghiron, C. A.; Evans, R. F.; Santus, R.; Bazin, M., Flash photolysis of tryptophan and N-acetyl-L-tryptophanamide; the effect of bromide on transient yields. *Photochem. Photobiol.* **1977,** *26*, 3-9.

43. Chen, Y.; Liu, B.; Yu, H. T.; Barkley, M. D., The peptide bond quenches indole fluorescence. *J. Am. Chem. Soc.* **1996,** *118* (39), 9271-9278.

44. Cadogan, K. D.; Albrecht, A. C., Two-photon ionizations in rigid organic solutions and the triplet-state intermediate. *J. Chem. Phys.* **1965,** *43* (7), 2550-2552.

45. Moan, J.; Steen, H. B., Photoinduced trapped electrons in rigid polar solution. II. Kinetics and cross section of two-quantum ionization. *J. Phys. Chem.* **1971,** *75* (19), 2893-2897.

46. Tamuliene, J.; Romanova, L. G.; Vukstich, V. S.; Papp, A. V.; Snegursky, A. V., Electron-impact-induced tryptophan molecule fragmentation. *Eur. Phys. J. D* **2015,** *69* (1).

47. Bernas, A.; Grand, D.; Amouyal, E., Photoionization of solutes and conduction band edge of solvents. Indole in water and alcohols. *J. Phys. Chem.* **1980,** *84* (10), 1259-1262.

48. Stevenson, K. L.; Papadantonakis, G. A.; LeBreton, P. R., Nanosecond UV laser photoionization of aqueous tryptophan: temperature dependence of quantum yield, mechanism, and kinetics of hydrated electron decay. *J. Photochem. Photobiol. A* **2000,** *133*, 159-167.

4 Solvent deuterium isotope effect on the decay kinetics of the tryptophan triplet in membrane protein folding

4.1 Abstract

The role of solvation in protein folding has been studied using a deuterium isotope effect on the triplet decay kinetics. Unfolded melittin and OmpA exhibit an isotope effect $\left(k_{H_2O}/k_{D_2O} < 1\right)$. The isotope effect is absent for OmpA bound to its chaperone Skp $\left(k_{H_2O}/k_{D_2O} \approx 1\right)$, and for folded melittin. The differences in the observed isotope effect is attributed to differences in solvation of the trp residue.

4.2 Introduction

In a suitable environment, the folding of proteins into its native configuration is spontaneous.[1] The folding process is well understood for small globular proteins via statistical energy landscape theory,[2-4] but far less is known about membrane proteins. There are at least two important driving forces in protein folding. One driving force is the formation of native contacts that stabilize the folded state.[5] The other driving force is solvent reorganization, e.g. hydrophobic effect.[6] The dynamics of protein chains and solvent water molecules are typically slaved to each other during folding,[7] and as such, water molecules play an important role in the folding mechanisms via their de-solvation dynamics.[8] Here, we characterize protein solvation in membrane protein folding.

The folding of membrane proteins *in vivo* and *in vitro* is complex. The production of viable proteins in the cell begins immediately following translation. The leader sequences of both types of membrane proteins, i.e. α-helical and β-barrel, directs them to the sec-translocon machinery. Whereas α-helical proteins are laterally inserted through a channel into the cytoplasmic membrane,[9] outer membrane proteins are secreted into the periplasm between the inner and outer leaflet.[10] Once in the periplasm, unfolded outer membrane proteins are bound by molecular chaperones, such as the 17 kDa protein (Skp), that prevent aggregation. Small outer membrane proteins spontaneously fold into synthetic lipid bilayers *in vitro* from the denatured state,[11] and are thought to be able to do so *in vivo.* The ability of outer membrane proteins to spontaneous fold suggests that common themes exist between globular and membrane protein folding. Consequently, the folding of outer membrane proteins has been the subject of many biophysical studies aimed toward

understanding the basic principles that govern the thermodynamics and kinetics of membrane protein structure formation.[12-20]

Isotopic substitution of the solvent with deuterium influences the phosphorescence decay kinetics of small aromatic molecules.[21-23] When H_2O is substituted with D_2O, the phosphorescence lifetime of the tryptophan residue has also been observed to display an isotope effect.[24-25] Specifically, Trp model compounds have been shown to exhibit longer triplet lifetimes in D_2O as measured by phosphorescence; this isotope effect is consistent with the fact that coupling to D_2O vibrations is less efficient than with H_2O because of the decreased vibrational frequency of O-D vs O-H. Many proteins exhibit a long lived triplet lifetime.[26] It follows that small differences in solvation will be reflected in the triplet lifetime, and moreover, it is expected the transfer of a protein from aqueous solvent to a lipid bilayer will exhibit a change in the isotope effect because of the elimination of bulk water in a bilayer.

In this work, we demonstrate an isotope effect in the lifetime of the tryptophan triplet in unfolded and folded membrane proteins that reflects the presence (or absence) of water coupled to the chomophore. We examined the decay kinetics of the triplet via transient absorption, and report an isotope effect that is opposite to that of phosphorescence measurements. These results highlight the successful application of triplet lifetimes to determine extent of solvent exposure in unfolded and folded membrane proteins.

4.3 Materials and Methods

4.3.1 Protein, peptide, and reagents

Recombinant OmpA wild-type (WT) and a mutant were cloned, expressed, and purified as described previously.[16] The mutant studied here was W7, which is a full-length OmpA variant that contains a single tryptophan residue at the native position 7 and the four other native tryptophan residues mutated to phenylalanine. Melittin was purchased from Genscript (New Jersey). The *in vitro* refolding of denatured proteins was performed using lipids (1,2-dimyristoyl-sn-glycero-3-phosphocholine, DMPC) from Avanti Polar Lipids. N-acetyl-tryptophanamide (NATA), urea-d4, and acetonitrile were purchased from Sigma Aldrich. Acetonitrile was dried using molecular sieves. Ultrapure urea was purchased from MP Biomedical. Ultrapure H_2O (18.2 MΩ cm) was obtained from a NANOpure purification system (Barnstead), and D_2O (99.9%) was purchased from Cambridge Isotope Laboratories or Sigma Aldrich. Potassium phosphate, Tris base, n-octyl-β-D-glucopyranoside (OG), and all other chemicals were purchased from Fisher Scientific.

4.3.2 Transient absorption measurements

The ns time-resolved absorption apparatus has been described elsewhere[27] and in Chapter 2. Briefly, the absorption of the Trp triplet was detected at 450 nm using a continuous-wave broadband probe light source and a monochromator (10 nm bandpass) with a 5-stage photomultiplier tube. The excitation pulse was generated by pumping an OPO with the third harmonic of a Nd:YAG laser. The output of the OPO was frequency-doubled in a barium borate crystal to produce pulses at 290 nm (8-10 ns, 20 Hz, 50 μJ). The continuous-wave probe beam and pulsed UV excitation beam were made collinear

through the sample. The transient absorption after photolysis from the 290-nm laser pulse was bandwidth-limited to 14 MHz and recorded using a 500 MHZ oscilloscope.

The samples were sealed under 1 atm of argon gas after cycling with vacuum in an atmosphere-controlled cuvette. NATA and melittin samples were prepared to a final concentration of 50 μM and volume of about 3 mL in a square 10 × 10 mm fused silica cuvette. OmpA samples were prepared to a final concentration of 40 μM and a volume of 800 μL in a 4 × 10 mm fused silica cuvette. The transient absorption for the latter was detected along the short pathlength. Each transient absorption trace that was recorded was an average of 1500 shots. The decay kinetics were determined from an exponential fit to at least 10× the nominal lifetime.

4.3.3 Indole H/D exchange

The indole nitrogen proton (NH) in NATA samples was substituted with deuteron (ND) by dissolving fully protiated NATA in D_2O. The sample was lyophilized to remove D_2O, and the resulting ND-NATA solid was redissolved in dry acetonitrile. Melittin samples were prepared in H_2O, D_2O, or deuterated Tris buffer without further preparation.

Deuterated OmpA was prepared by extensive buffer exchange against 8.0 M urea–d4, 10 mM Tris/D_2O, pD 8, with the use of a Millipore Ultra 15 kDa centrifugal unit. The dilution volume was approximately 100-fold. This sample was diluted an additional 10-fold during the final step of sample preparation. The chaperone Skp in deuterated buffered was also prepared by buffer exchange.

4.3.4 Vesicle preparation

The protocol for vesicle preparation has been described previously.[16, 28] Briefly, the chloroform was removed from a lipid stock using a stream of nitrogen gas. The dry lipid was resuspended in Tris buffer to a concentration of 5 or 10 mg/mL using microtip sonication. Vesicle solutions were passed through a 0.45 μm filter to remove metal debris from sonication. The final vesicle solution was equilibrated overnight at 37℃ prior to experiments. The final lipid concentration was 1 mg/mL for melittin and 2 mg/mL for OmpA samples.

4.4 Results

4.4.1 Isotope effect on the triplet decay kinetics of NATA

Figure 4.1 shows the decay of the triplet absorption of NATA in Tris buffered water and deuterium oxide solutions. The data are fit to a single-exponential equation. The decay rate $\left(\tau^{-1} \equiv k\right)$ when the indole ring nitrogen is in the protonated form (NH) is defined as k_{H}, and when deuterated (ND), the decay constant is k_{D}. The decay lifetimes were 72 and 52 μs for NATA in H_2O and D_2O, respectively; these results are summarized in Table 4.1. The triplet decay kinetics from transient absorption display an *inverse* isotope effect $\left(k_{\mathrm{H}}/k_{\mathrm{D}} < 1\right)$ compared to published reports that utilized phosphorescence measurements; in these previous reports, the isotope effect $k_{\mathrm{H}}/k_{\mathrm{D}}$ was greater than 1. The triplet NATA in aqueous 0.3 and 0.8 M urea solutions displayed the same trend as non-urea solutions, i.e. the triplet state decays faster in deuterated water. The decay lifetimes were generally longer by as much as 2-fold in urea solutions compared to non-urea solutions. All NATA samples displayed a baseline offset due to a residual component with a long decay time constant.

The triplet decay kinetics of protiated and deuterated NATA samples were measured in aprotic solvent to determine if the isotope effect on the decay kinetics is due to an intramolecular deuterium exchange or primarily influenced by solvent. Figure 4.2 shows the triplet decay kinetics of NATA $\left(\mathrm{NH}/\mathrm{D}\right)$ samples after solvent exchange to dry acetonitrile. These triplet lifetimes in acetonitrile were generally longer than in water, but the samples did not exhibit an isotope effect, $k_{\mathrm{H}}/k_{\mathrm{D}} \approx 1$. This finding suggests that the

isotope effect in aqueous solution largely reflects coupling of the triplet state to water, and not intramolecular vibrational differences of NH- vs ND-NATA (discussed further below). The magnitude of the transient absorption signal in acetonitrile was at least 4-fold greater than in aqueous solution.

4.4.2 Isotope effect on the triplet decay kinetics of melittin

The triplet decay kinetics and corresponding isotope effect of the melittin peptide are comparable to the results for NATA samples. Compared to NATA, the lifetime was slightly shorter for melittin, but the decay traces were remarkably reproducible within the same sample and different sample preparations; representative data are shown in Figure 4.3. When melittin was added to lipid vesicles (Figure 4.4), the lifetimes for the folded peptide were relatively unchanged from the unfolded forms, but an isotope effect was absent, $k_H/k_D \approx 1$. The vesicle-containing melittin samples became opaque during the duration of the experiment. However, this optical obscurity did not affect the reproducibility of the melittin triplet lifetimes during the duration of the experiment.

4.4.3 Isotope effect on the triplet decay kinetics of OmpA

The triplet decay lifetimes of unfolded/aggregated WT and W7 OmpA were quenched by as much as 10-fold compared to unfolded melittin, with lifetimes less than 10 μs for unfolded OmpA. The isotope effect was surprisingly opposite to that of NATA and melittin, with $k_H/k_D \geq 1$. When WT and W7 OmpA was folded into detergent micelles (10 mg/mL OG), the triplet lifetimes of WT increased marginally, while W7 increased substantially to ~100 μs. In contrast to folded melittin, which lacked an isotope effect, the decay kinetics of folded OmpA in micelles displayed an isotope effect, $k_H/k_D < 1$.

The triplet lifetimes of unfolded OmpA W7 bound by the chaperone Skp was ~20 μs, which is an intermediate value relative to unfolded protein and folded protein in micelle. This finding indicates that the Skp-bound unfolded form is different from the collapsed/denatured form in 0.8 M urea (see below). The isotope effect for the Skp-bound protein was $k_H/k_D \approx 1$, which suggests that Skp-encapsulated protein is not as sensitive to solvent as unfolded in 0.8 M urea or folded protein in OG.

The triplet lifetimes for OmpA W7 were measured at three timepoints during the folding reaction into lipid vesicles. Figure 4.5 shows that the increase in triplet lifetime from 15 to 180 μsec, which corresponds to 10 to 180 minutes after unfolded protein was mixed with vesicle. The solution became opaque during the reaction. However, the results were reproducible between sample preparations.

4.5 Discussion

The decay kinetics of the triplet excited state of NATA in water and deuterium oxide exhibits the normal, expected isotope effect $\left(k_{H_2O}/k_{D_2O} > 1\right)$ as determined from phosphorescence lifetimes.[24] We characterized the isotope effect on the triplet decay kinetics of NATA, the single Trp-containing peptide melittin, and OmpA using transient absorption. The results from transient absorption measurements show an *inverse* isotope effect $\left(k_{H_2O}/k_{D_2O} < 1\right)$; the reason for the opposite outcome from phosphorescence measurements is the subject of future studies. Nonetheless, the results here illustrate that the isotope effect can be used to report on the degree of solvent accessibility of the tryptophan residue in unfolded and folded membrane proteins.

4.5.1 NATA

The normal isotope effect in the phosphorescence decay rate of simple aromatic molecules has been attributed to vibrational contributions to the intramolecular $T_1 \rightarrow S_0$ radiationless transition.[29] Similar analyses have been made for intermolecular relaxation that involves bath accepting modes, e.g. water O−H stretch. The non-radiative decay rate of the triplet state (under the assumption of Born-Oppenheimer approximation) described by El Sayed includes a term for vibrational overlap between the excited triplet and solvent accepting modes: rate of non-radiative transition for the triplet state is $\propto \prod_{if} \left|\Theta_{Sf}|\Theta_{Ti}\right|^2 \Phi_S|V|\Phi_T{}^2$ where Θ_{Sf} and Θ_{Ti} are the vibrational wavefunctions *i* and *f* of the final solvent (S) and initial triplet (T) states, and Φ_S and Φ_T are the electronic wavefunctions of the solvent and triplet states. The first term, $\left|\Theta_{Sf}|\Theta_{Ti}\right|^2$, is simply the

Franck-Condon (FC) factor. The perturbation, V, could be spin-orbit coupling between the two states. In the context of Fermi's golden rule, the transition rate is also dependent on the density of final states, ρ. Both the FC factor and density of states can lead to large isotope effects between the vibrationally relaxed triplet and the singlet ground state.[29-31] In this formulation, the rate is governed mainly by vibrational coupling and overlap while the bath provides a continuum of states (ρ). The final vibrational states can also be treated.[32-33]

In the state diagram shown in Figure 4.5, a lower isoenergetic quantum number for H_2O (v ~8) compared to D_2O (v ~16) leads to greater FCs in water than deuterium oxide. The harmonics were calculated from Tam and Patel.[34] We assume that the triplet decay is dominated by vibronic coupling and FC factors, although no attempt is made to calculate the rate of decay. However, the observed *inverse* isotope effect $k_{H_2O}/k_{D_2O} < 1$ in our results indicates that other considerations must be made, e.g. excited-state photochemistry or photoionization. The observation of the normal isotope effect for NATA from phosphorescence decays reported by Fischer et al. were determined using excitation energies below 0.1 μJ/pulse.[24] Further, our decay lifetimes of 72 μs are longer than those reported previously (NATA 40 μs[24], NATA 30 μs[35], Trp 12 μs[36]). One explanation for the difference in lifetimes maybe due to different methods employed for preparation of deoxygenated samples.

The central theme of this report is to utilize the isotope effect, regardless of the direction of the isotope effect, as a measure of the presence of local water. The hope is that the isotope effect is dominated by solvent accepting modes, and not by intramolecular

modes on account of ND-NATA or NH-NATA. If the isotope effect can be attributed to the presence of OH or OD in the solvent, then we expect the isotope effect to essentially vanish in dry acetonitrile solutions. Indeed, this isotope effect is minimized in acetonitrile, where the ratio of triplet decay rates of NH-NATA and ND-NATA is close to unity: $k_H/k_D = 1.07$. Further, the isotope effect is not present in N-methyl indole.[24] In general, this observation suggests that the isotope effect, either normal or inverse, can be used to indicate the presence of aqueous solvent.

4.5.2 Melittin

If protein hydration evolves during membrane protein folding, we can expect a difference in isotope effect in unfolded and folded protein. Melittin is a small membrane-interacting peptide containing 26 amino acids and a single Trp residue. The sequence is GIGAVLKVLTTGLPALISWIKRKRQQ. The peptide is unfolded in buffered solutions, and folded when bound to neutral lipids vesicles as determined from the fluorescence emission. The tryptophan emission maximum blue-shifts 10 nm when bound to lipid vesicles, suggesting a change from an aqueous to a hydrophobic environment. As expected with this dehydration event, the isotope effect vanishes when melittin is bound to vesicles, from 0.71 (unfolded) to 1.07 (folded). This result is consistent with the change in fluorescence maximum. This finding suggests that isotope effect can be used to investigate the extent of solvation for a membrane-associated peptide.

4.5.3 OmpA

The isotope effect in unfolded and folded OmpA provides insight into the role of protein hydration in folding. First, characterizing the unfolded state is just as important as the folded state in the folding reaction. The triplet decay lifetimes in unfolded WT and W7 OmpA in 0.8 M urea are quenched, likely because of interaction with backbone or residues known to quench the triplet state (e.g. cysteine, tyrosine, and histidine).[37] The isotope effect of unfolded protein is difficult to measure on account of the short lifetime of <10 ms; nonetheless, it appears to be normal. It is worth noting that in 0.8 M urea, it may be more appropriate to consider OmpA as aggregated, and not fully unfolded.

The chaperone protein Skp is known is bind unfolded OmpA. In fact, it has been proposed that the unfolded form of OmpA bound to Skp is distinct from fully unfolded OmpA, or aggregated OmpA, in aqueous solution. This difference in structure agrees with our results. The lifetimes of Skp-bound OmpA are longer than in unfolded OmpA, and the isotope effect vanishes for the Skp-bound form. It should be noted that approximately half of the signal is due to a leader sequence in Skp, which contains one tryptophan residue. Unfortunately, we were unable to obtain Skp that lacked this leader sequence.

We also examined the structure of OmpA folded into OG micelles. The triplet lifetimes of WT and W7 are longer than unfolded protein. However, the WT lifetimes are still quenched. In the single trp-mutant the lifetime is longer than the WT protein that contains five trp residues. One possibility is that triplet-triplet energy transfer quenches the lifetimes. The folded protein in micelles is distinct from the protein folded into lipid

vesicles. The presence of an isotope effect in micelles may suggest the water is still accessible to the W7 position in the folded protein in the micelle cavity.

Finally, the evolution of the triplet lifetime from unfolded to folded states is visible in the folding experiment of OmpA. As shown in Figure 4.5, the lifetime evolves from 15 to 180 μs in H_2O during the 3-hour folding period. We have not yet performed the identical experiment in D_2O, but expect to observe the disappearance of the isotope effect as the protein folds.

4.6 Conclusions

These results show that the decay kinetics of the tryptophan triplet as measured by transient absorption exhibit an inverse isotope effect for D_2O. We examined the triplet decay kinetics of unfolded and folded membrane proteins. Both unfolded and folded protein are sensitive to the isotopic composition of the solvent. However, the degree of accessibility determines the extent of the isotope effect. This study shows that an isotope effect on the decay kinetics of the tryptophan residue can be used as a measure of solvent accessibility during folding.

4.7 Acknowledgements

Chapter 4 is in preparation for submission: Lopez-Peña, I, Kleinschmidt, J. H, Kim, J. E, “Solvent deuterium isotope effect on the decay kinetics of the tryptophan triplet in membrane protein folding”. The dissertation author was the primary investigator and author of this paper.

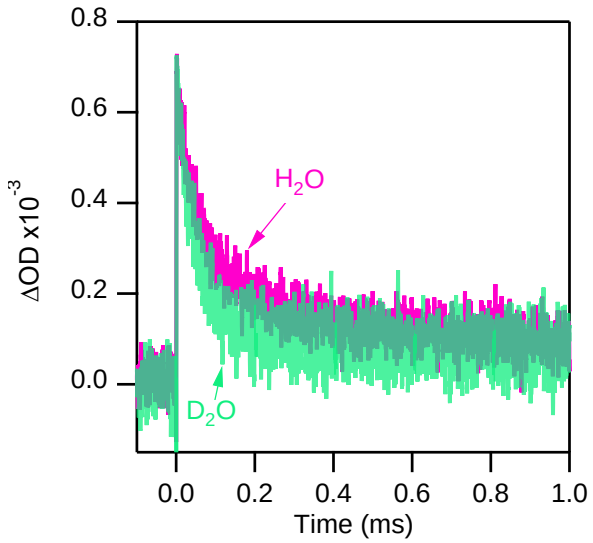

Figure 4.1 Transient absorption kinetic traces at 450 nm of 50 μM NATA in H_2O (pink) and D_2O (green), 40 mM Tris pH=7.6 or pD=8.0. UV pump power 290 nm was 50 μJ/pulse at the sample. Each curve represents the average of 1500 pulses. The data were subjected to a 1 μs box car average. The different shades of pink and green (overlaid) are sequential measurements in H_2O and D_2O, respectively. The traces of NATA in D_2O (green) were multiplied by a scalar 1.3 to match the amplitude of the traces in H_2O (pink)

Table 4.1 The tryptophan triplet decay kinetics of n-acetyl-l-tryptophanamide, melittin, and outer membrane protein A (OmpA) in H2O and D2O

Solvent	Lifetimes (μs)		k_H/k_D
NATA	NH	ND	
40 mM Tris	72 ± 12	52 ± 6	0.73 ± 0.15
0.3 M urea, 40 mM Tris	128 ± 7	112 ± 10	0.88 ± 0.09
0.8 M urea, 40 mM Tris	109 ± 11	70 ± 5	0.64 ± 0.08
acetonitrile (solvent exchange)	86 ± 4	92 ± 4	1.07 ± 0.07
melittin			
40 mM Tris	50 ± 6	36 ± 5	0.71 ± 0.12
40 mM Tris, 1 mg/mL DMPC	52 ± 2	56 ± 6	1.07 ± 0.12
WT			
0.8 M urea, 40 mM Tris	2.7 ± 0.3	3.2 ± 0.3	1.2 ± 0.2
0.8 M urea, 40 mM Tris, 10 mg/mL OG	8.7 ± 0.1	6.3 ± 0.2	0.72 ± 0.09
W7			
0.8 M urea, 40 mM Tris	4.1 ± 1.0	7.3 ± 1.4	1.8 ± 0.5
0.8 M urea, 40 mM Tris, 10 mg/mL OG	111 ± 13	91 ± 5	0.82 ± 0.10
0.8 M urea, 40 mM Tris, 4x Skp	21 ± 3	22 ± 2	1.00 ± 0.15
W7			
0.8 M urea, 40 mM Tris 1 mg/mL DMPC, 10 min	15 ± 3		
0.8 M urea, 40 mM Tris 1 mg/ml DMPC, 60 min	80 ± 8		
0.8 M urea, 40 mM Tris 1 mg/ml DMPC, 60 min	180 ± 18		

$\tau^{-1} \equiv k$

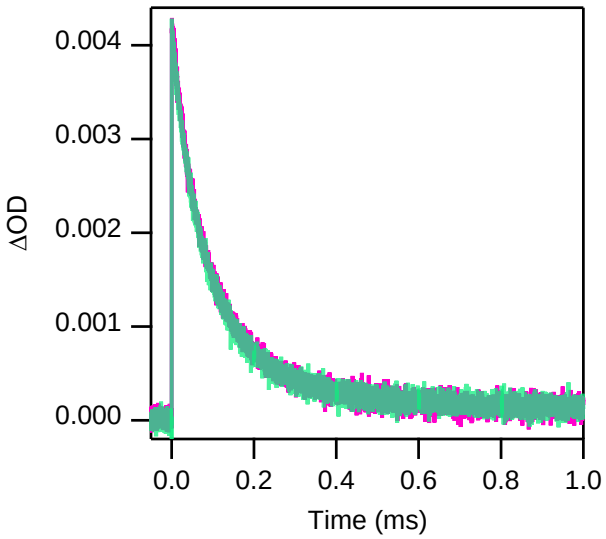

Figure 4.2 Transient absorption kinetic traces at 450 nm of 50 μM NATA-NH (pink) and NATA-ND (green) in dry acetonitrile. UV pump power at 290 nm was 50 μJ/pulse at the sample. Each curve represents the average of 1500 pulses. The different shades of pink and green (overlaid) indicate sequential measurements for NATA-NH and NATA-ND, respectively.

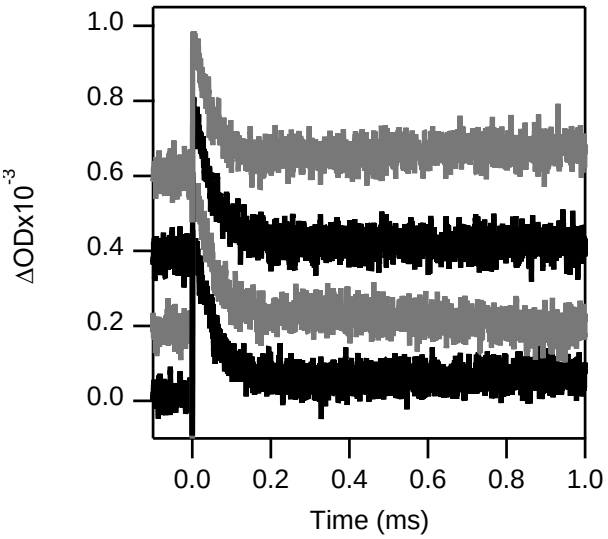

Figure 4.3 Transient absorption kinetic traces at 450 nm of 50 μM melittin in H_2O 40 mM Tris pH(D) 8. UV pump power at 290 nm was 50 μJ/pulse at the sample. Each curve represents repeat photolysis of the same sample over the course of 12000 shots. The data were subjected to a 1 μs box car average.

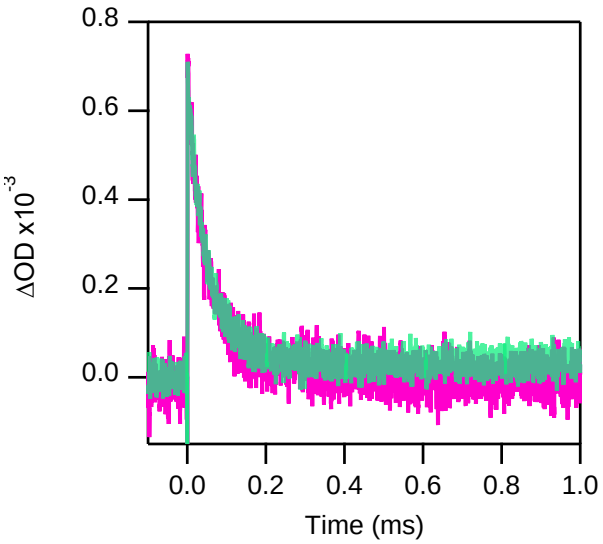

Figure 4.4 Transient absorption kinetic traces at 450 nm of 50 μM melittin in H_2O (pink) and D_2O (green) 40 mM Tris pH(D) 8, 1 mg/mL DMPC. UV pump power at 290 nm was 50 μJ/pulse at the sample. Each curve represents the average of 1500 pulses. The data were subjected to a 1 μs box car average, the different shades of pink and green (overlaid) indicate sequential measurements in H_2O and D_2O, respectively. The traces of melittin in D_2O (green) were multiplied by the scalar 0.67 to match the amplitude of the traces in H_2O (pink).

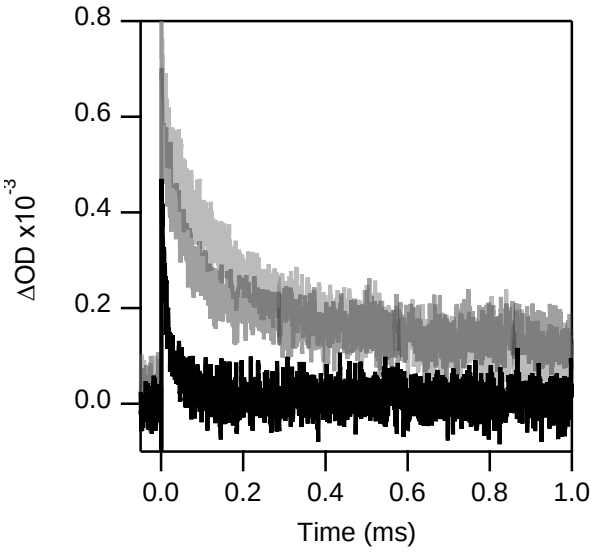

Figure 4.5 Transient absorption kinetic traces of 40 μM W7 folding into DMPC vesicles at 450 nm. UV pump power at 290 nm was 50 μJ/pulse at the sample. Each curve represents the average of 1500 pulses. The data were subjected to a 1 μs box car average, black is unfolded protein, and gray curves are kinetic traces at 10, 60, and 180 min after initiation of the folding reaction. The lifetimes are 15, 80, and 180 μs, respectively.

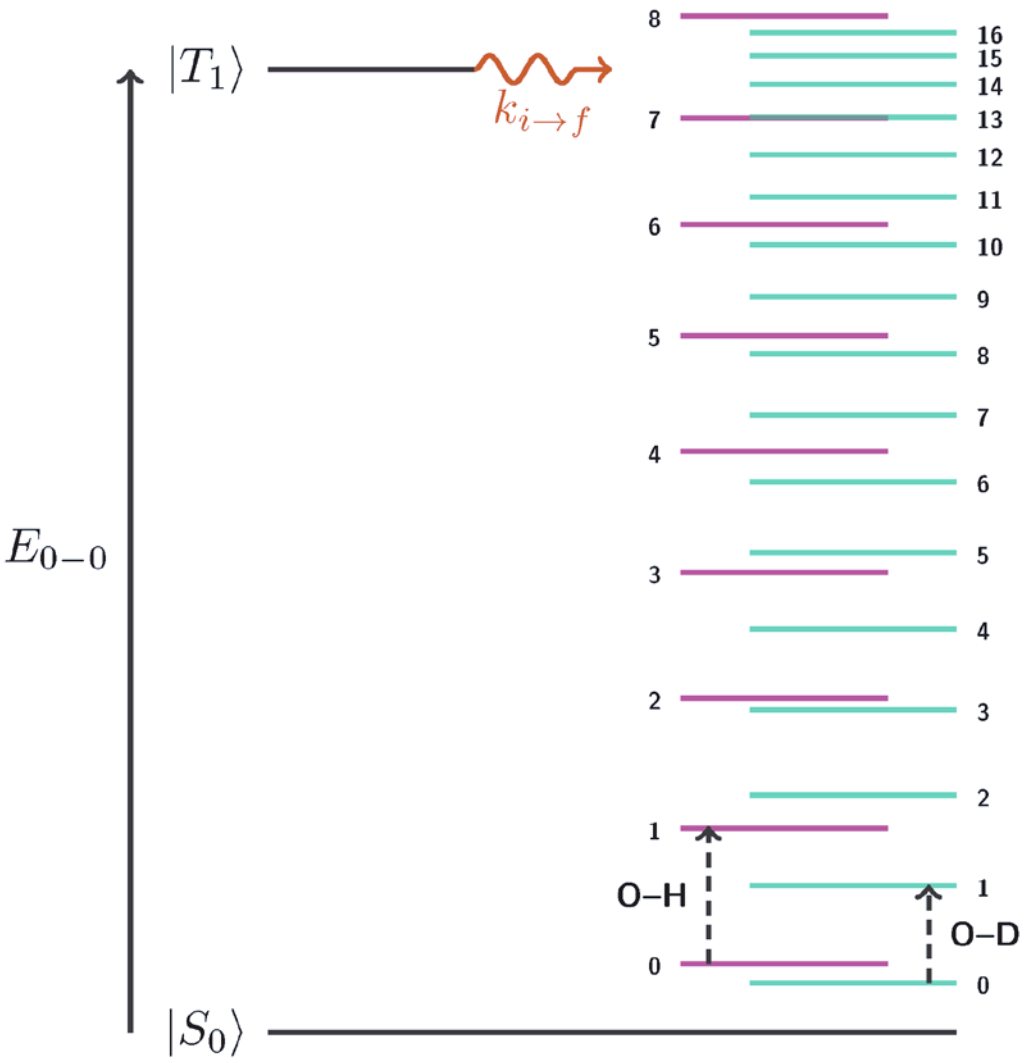

Figure 4.6 State diagram for the rate of intramolecular radiationless decay of the triplet excited state. The relative vibrational energy levels for the fundamental O−H (3500 cm^{-1}) and O−D (2500 cm^{-1}) stretches were calculated from ref 34.

4.8 References

1. Anfinsen, C. B., Principles that govern the folding of protein chains. *Science* **1973,** *181*, 223-230.

2. Bryngelson, J. D.; Wolynes, P. G., Spin glasses and the statistical mechanics of protein folding. *Proc. Natl. Acad. Sci. U. S. A.* **1987,** *84* (21), 7524-7528.

3. Frauenfelder, H.; Sligar, S. G.; Wolynes, P. G., The energy landscapes and motions of proteins. *Science* **1991,** *254*, 1598-1603.

4. Bryngelson, J. D.; Onuchic, J. N.; Socci, N. D.; Wolynes, P. G., Funnels, pathways, and the energy landscape of protein folding: a synthesis. *Proteins* **1995,** *21* (3), 167-195.

5. Munoz, V.; Eaton, W. A., A simple model for calculating the kinetics of protein folding from three-dimensional structures. *Proc. Natl. Acad. Sci. U. S. A.* **1999,** *96* (20), 11311-11316.

6. Kauzmann, W., Some factors in the interpretation of protein denaturation. *Adv. Protein Chem.* **1959,** *14*, 1-63.

7. Frauenfelder, H.; Fenimore, P. W.; Chen, G.; McMahon, B. H., Protein folding is slaved to solvent motions. *Proc. Natl. Acad. Sci. U. S. A.* **2006,** *103* (42), 15469-15472.

8. Cheung, M. S.; Garcia, A. E.; Onuchic, J. N., Protein folding mediated by solvation: Water expulsion and formation of the hydrophobic core occur after the structural collapse. *Proc. Natl. Acad. Sci. U. S. A.* **2002,** *99* (2), 685-690.

9. Cymer, F.; von Heijne, G.; White, S. H., Mechanisms of integral membrane protein insertion and folding. *J. Mol. Biol.* **2015,** *427* (5), 999-1022.

10. Tamm, L. K.; Hong, H.; Liang, B. Y., Folding and assembly of beta-barrel membrane proteins. *Biochim. Biophys. Acta, Biomembr.* **2004,** *1666* (1-2), 250-263.

11. Surrey, T.; Jähnig, F., Refolding and oriented insertion of a membrane protein into a lipid bilayer. *Proc. Natl. Acad. Sci. U. S. A.* **1992,** *89*, 7457-7461.

12. Kleinschmidt, J. H.; den Blaauwen, T.; Driessen, A. J. M.; Tamm, L. K., Outer membrane protein A of *Escherichia coli* inserts and folds into lipid bilyers by a concerted mechanism. *Biochemistry* **1999,** *38* (16), 5006-5016.

13. Bulieris, P. V.; Behrens, S.; Holst, O.; Kleinschmidt, J. H., Folding and insertion of the outer membrane protein OmpA is assisted by the chaperone Skp and by lipopolysaccharide. *J. Biol. Chem* **2003,** *278* (11), 9092-9099.

14. Hong, H.; Tamm, L. K., Elastic coupling of integral membrane protein stability to lipid bilayer forces. *Proc. Natl. Acad. Sci. U. S. A.* **2004,** *101*, 4065-4070.

15. Sanchez, K. M.; Neary, T. J.; Kim, J. E., UV resonance Raman spectroscopy of folded and unfolded states of an integral membrane protein. *J. Phys. Chem. B* **2008,** *112*, 9507-9511.

16. Sanchez, K. M.; Gable, J. E.; Schlamadinger, D. E.; Kim, J. E., Effects of tryptophan microenvironment, soluble domain, and vesicle size on the thermodynamics of membrane protein folding: lessons from the transmembrane protein OmpA. *Biochemistry* **2008,** *47*, 12844-12852.

17. Patel, G. J.; Behrens-Kneip, S.; Holst, O.; Kleinschmidt, J. H., The periplasmic chaperone Skp facilitates targeting, insertion, and folding of OmpA into lipid membranes with a negative membrane surface potential. *Biochemistry* **2009,** *48*, 10235-10245.

18. Sanchez, K. M.; Kang, G.; Wu, B.; Kim, J. E., Tryptophan-lipid interactions in membrane protein folding probed by UV resonance Raman and fluorescence spectroscopy. *Biophys. J.* **2011,** *100*, 2121-2130.

19. Andersen, K. K.; Wang, H.; Otzen, D. E., A kinetic analysis of the folding and unfolding of OmpA in urea and guanidinium chloride: single and parallel pathways. *Biochemistry* **2012,** *51*, 8371-8383.

20. Hong, H.; Rinehart, D.; Tamm, L. K., Membrane depth-dependent energetic contribution of the tryptophan side chain to the stability of integral membrane proteins. *Biochemistry* **2013,** *52* (25), 4413-21.

21. Wright, M. R.; Frosch, R. P.; Robinson, G. W., Phosphorescence lifetime of benzene. An intermolecular heavy-atom effect, a deuterium effect, and a temperature effect. *J. Chem. Phys.* **1960,** *33* (3), 934-935.

22. Watts, R. J.; Strickler, S. J., Deuterium isotope effects on the lifetime of the phosphorescence state of naphthalene. *J. Chem. Phys.* **1968,** *49* (9), 3867-3871.

23. Hutchison, C. A.; Magnum, B. W., Effect of deuterium substitution on the lifetime of the phosphorescent triplet state of naphthalene. *J. Chem. Phys.* **1960,** *32*, 1261-1262.

24. Fischer, C. J.; Gafni, A.; Steel, D. G.; Schauerte, J. A., The triplet-state lifetime of indole in aqueous and viscous environments: Significance to the interpretation of room temperature phosphorescence in proteins. *J. Am. Chem. Soc.* **2002,** *124*, 10359-10366.

25. Fischer, C. J.; Schauerte, J. A.; Wisser, K. C.; Gafni, A.; Steel, D. G., Hydrogen exchange at the core of *Escherichia coli* alkaline phosphatase studied by room-temperature tryptophan phosphorescence. *Biochemistry* **2000,** *39* (6), 1455-1461.

26. Vanderkooi, J. M.; Calhoun, D. B.; Englander, S. W., On the prevalence of room-temperature protein phosphorescence. *Science* **1987,** *236*, 568-569.

27. Wang, C.; Angelella, M.; Kuo, C. H.; Tauber, M. J., Singlet fission in carotenoid aggregates: insights from transient absorption spectroscopy. *Proc. SPIE* **2012,** *8459*.

28. Kang, G. P.; Lopez-Peña, I.; Oklejas, V.; Gary, C. S.; Cao, W. H.; Kim, J. E., Förster resonance energy transfer as a probe of membrane protein folding. *Biochim. Biophys. Acta* **2012,** *1818* (2), 154-161.

29. Robinson, G. W.; Frosch, R. P., Electronic excitation transfer and relaxation. *J. Chem. Phys.* **1963,** *38* (5), 1187-1203.

30. Siebrand, W., Mechanism of radiationless triplet decay in aromatic hydrocarbon and the magnitude of the Franck-Condon factors. *J. Chem. Phys.* **1966,** *44* (10), 4055-4057.

31. Siebrand, W.; Williams, D. F., Isotope rule for radiationless transitions with an application to triplet decay in aromatic hydrocarbons. *J. Chem. Phys.* **1967,** *46* (1), 403-404.

32. Freed, K. F.; Jortner, J., Radiative decay of polyatomic molecules. *J. Chem. Phys.* **1969,** *50* (7), 2916-2927.

33. Englman, R.; Jortner, J., The energy gap law for radiationless transitions in large molecules. *Mol. Phys.* **1970,** *18* (2), 145-164.

34. Tam, A. C.; Patel, C. K. N., Optical absorptions of light and heavy water by laser optoacoustic spectroscopy. *Appl. Optics* **1979,** *18* (19), 3348-3358.

35. Sudhakar, K.; Phillips, C. M.; Owen, C. S.; Vanderkooi, J. M., Dynamics of parvalbumin studied by fluorescence and emission and triplet absorption spectroscopy of tryptophan. *Biochemistry* **1995,** *34* (4), 1355-1363.

36. Bent, D. V.; Hayon, E., Excited state chemistry of aromatic amino acids and related peptides. III. Tryptophan. *J. Am. Chem. Soc.* **1975,** *97* (10), 2612-2619.

37. Gonnelli, M.; Strambini, G. B., Intramolecular quenching of tryptophan phosphorescence in short peptides and proteins. *Photochem. Photobiol.* **2005,** *81* (3), 614-622.

5 Insights into protein structure and dynamics by ultraviolet and visible resonance Raman Spectroscopy

5.1 Abstract

Raman spectroscopy is a form of vibrational spectroscopy based on inelastic scattering of light. In *resonance* Raman spectroscopy, the wavelength of the incident light falls within an absorption band of a chromophore, and this overlap of excitation and absorption energy greatly enhances the Raman scattering efficiency of the absorbing species. The ability to probe vibrational spectra of select chromophores within a complex mixture of molecules makes resonance Raman spectroscopy an excellent tool for studies of biomolecules. In this Current Topic, we discuss the type of molecular insights obtained from steady-state and time-resolved resonance Raman studies of a prototypical photoactive protein, rhodopsin. We also review recent efforts in ultraviolet resonance Raman investigations of soluble and membrane-associated biomolecules, including integral membrane proteins and antimicrobial peptides. These examples illustrate that resonance Raman is a sensitive, selective, and practical method for studying the structures of biological molecules, and the molecular bonding, geometry, and environments of protein cofactors, the backbone, and side chains.

5.2 Introduction

The Raman effect was first reported by C. V. Raman in 1928[1,2] and describes inelastic scattering of light from molecules. The difference in energy between the incident and scattered photon corresponds to the vibrational frequency of one of the Raman-active normal modes of the molecule. Hence, Raman spectroscopy reveals vibrational structures. Raman scattering is observed for normal modes that are characterized by a change in polarizability during vibration; in contrast, infrared absorption is associated with a change in dipole moment during vibration. The Raman effect is inherently weak; ~1 in 10^{10} of the incident photons is inelastically scattered in the form of Raman scattering relative to absorption in the form of an infrared transition.[3] The energy of the Raman scattered photon may be lower or higher than that of the incident light. In Stokes Raman scattering, the energy of the scattered photon is lower than that of the incident photon (see Figure 5.1). When the energy of the scattered photon is higher than that of the incident radiation, the process is called anti-Stokes Raman scattering. Anti-Stokes scattering requires population of higher-lying vibrational states and, therefore, is observed for only low-frequency or hot vibrational modes.

In resonance Raman spectroscopy, the incident wavelength is resonant with an electronic transition. Figure 5.1 shows both the Stokes and anti-Stokes resonance Raman scattering process. The efficiency of Raman scattering is increased drastically, typically by ~10^3 to 10^6, under resonance conditions.[3–5] Vibrational modes that are coupled to the allowed electronic transition of the absorbing chromophore are selectively enhanced. Fully symmetric modes generally exhibit the strongest enhancements because they can have large displacement (Δ) between ground and resonant excited states (Figure 5.1).[6] In one

limit, the Raman cross section of a mode is proportional to Δ^2. Separate from resonance enhancement, the excitation (E_{exc}) and scattering (E_{scatt}) photon energies also play important roles in determining Raman intensities because the resonance Raman cross section is proportional to $E_{exc}E_{scatt}{}^3$. This wavelength dependence offers an important advantage for ultraviolet (UV) resonance Raman spectroscopy.

The first biological application of resonance Raman spectroscopy (on carotenoids) appeared in 1932, which is only four years after C.V. Raman first reported the Raman effect.[5] About four decades later, in 1970, Rimai and co-workers published the spectra of carotenoid pigments from carrot root and tomato tissue and of the protein rhodopsin from frozen bovine retinae.[7,8] Raman measurements of the heme structure in hemoglobin[9,10] and cytochrome c[11] were reported afterward. In light of these studies, a strategy for the calculation of resonance Raman scattering was presented by Warshel to facilitate vibrational-mode assignment and the interpretation of spectra from proteins.[12] Today, more than 40 years after the first visible resonance Raman spectrum of a biological system was published, Raman instrumentation is commercially widespread, and visible resonance Raman spectroscopy has become a straightforward tool in biophysics research.

In the case of biological molecules, when the excitation wavelength is tuned to coincide with a UV or visible absorption band of a chromophore, the scattering intensities of the normal modes associated with that chromophore are enhanced while Raman intensities of all other normal modes of the biomolecule and aqueous buffer remain weak. In this manner, resonance Raman spectroscopy provides chromophore-specific signal without the need for isotopic labeling or other chemical modification. This specificity

contrasts with infrared absorption in which strong signal from IR-active water as well as other molecules is a common problem. This increased sensitivity of resonance Raman allows for the investigation of samples with low concentrations; resonance Raman spectra of micro- to nanomolar concentrations are obtained in minutes. Raman spectroscopy, like other vibrational techniques, has high time and structure sensitivity and can be used to characterize nuclear motions that occur on the timescale of 10^{-13} s and measure changes in bond lengths of ~0.2 Å.[13] Collectively, these advantages make resonance Raman a valuable method for studying the structures of biological molecules, and the molecular bonding, geometry, and environment of protein cofactors, the backbone, and side chains.

The fact that resonance Raman is capable of yielding structural information with fast time resolution and high selectivity makes it an excellent tool for the study of protein dynamics. Steady-state and time-resolved optical techniques, including resonance Raman spectroscopy, complement high-resolution structural methods in the characterization of electronic and nuclear structures of biological molecules and reaction intermediates. High-resolution methods reveal the average atomic coordinates of the protein ensemble, typically under equilibrium conditions. In addition to static structures, knowledge of the dynamics associated with proteins is essential for fully understanding their varied functions. A broad range of dynamical events over several orders of magnitude in time scale have been probed, such as bond formation and breakage, side-chain rotations, ligand binding, protein folding, and aggregation. The large variation in biologically relevant time scales can be accessed with a variety of methods. X-ray diffraction[14] and multidimensional nuclear magnetic resonance (NMR)[15] techniques remain two of the most powerful structural tools for biomolecules. Optical tools are also essential in the study of proteins. It is now standard to

determine reaction kinetics of aqueous protein solutions using continuous-wave (CW) or pulsed lasers combined with rapid-mixing, rapid-flowing, or pump–probe methods. Techniques such as absorption, fluorescence, circular dichroism, and vibrational spectroscopies offer advantages such as minimal sample preparation, dilute solutions, and facile sample recovery. The advent of pulsed lasers has allowed for the measurement of reaction kinetics with femtosecond time resolution, which is comparable to the time scale for molecular vibrations.

We present in this Current Topic biological applications of resonance Raman spectroscopy, with focus on time-resolved studies of a prototypical photoactive protein and recent UV resonance spectroscopy of biomolecules. The first section provides background on the experimental methods, and the second section discusses visible resonance Raman studies of rhodopsin; we have chosen rhodopsin as a prototypical protein to illustrate the depth and breadth of information gained from resonance Raman studies, in particular time-resolved experiments. In the final section, we discuss investigations of the side chains and backbone of soluble and membrane proteins using UV resonance Raman spectroscopy.

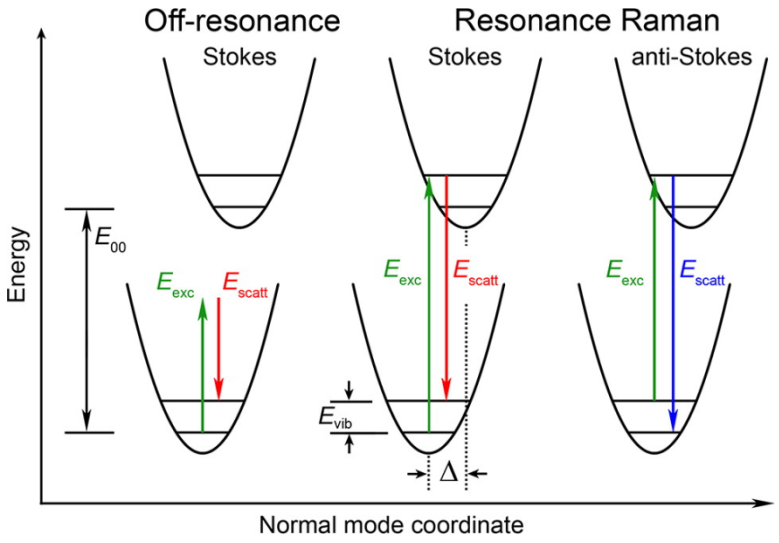

Figure 5.1. Schematic of the Raman process for a single, harmonic normal mode. Energies of the incident excitation and Raman scattered photons are denoted E_{exc} (green) and E_{scatt} (red and blue), respectively. The zero−zero energy of absorption is denoted E_{00}. Left: off-resonance Raman spectroscopy (Stokes) in which E_{exc} does not coincide with an absorption band. Middle: resonance Raman scattering in which E_{scatt} is lower than E_{exc} (Stokes). Right: resonance Raman spectroscopy in which E_{scatt} is greater than E_{exc} (anti-Stokes). The difference in energy between E_{exc} and E_{scatt} is the Raman shift, denoted E_{vib}, and reflects the vibrational energy of the normal mode. The difference in equilibrium geometry between ground and excited states is denoted Δ.

5.3 Experimental Methods

5.3.1 Picosecond and Femtosecond Resonance Raman Spectroscopy

The history of visible ultrafast resonance Raman spectroscopy is extensive, and there has been rapid growth in the capabilities of this technique. The first picosecond resonance Raman experiments were conducted in the early 1980s, which is approximately a decade after the first CW experiment was described. In these initial studies of hemoglobin and rhodopsin dynamics, a single-pulse method was used in which pump and probe photons were contained within a single 30 ps pulse.[16,17] Subsequent two-color, pump–probe experiments based on dye lasers and solid-state, Ti:sapphire systems were reported.[18–23] In the dye lasers, tunability was achieved by combinations of dyes and nonlinear frequency conversion methods, such as second-harmonic generation or continuum generation. Ultrafast resonance Raman experiments based on Ti:sapphire systems relied on harmonic generation as well as Raman shifting. The stability and commercial availability of Ti:sapphire lasers further expanded the capabilities of resonance Raman to the femtosecond time regime in femtosecond stimulated Raman spectroscopy (FSRS).[24–27] Given the robust nature and ease of operation of Ti:sapphire systems, ultrafast Raman studies have become common, and numerous reviews of picosecond spontaneous[21–23] and femtosecond stimulated[24–27] resonance Raman experiments have been published. FSRS has become a particularly valuable technique that has allowed investigations of excited-state structures and dynamics. Experimental details will not be described here.

5.3.2 Ultraviolet Resonance Raman Spectroscopy

UV resonance Raman spectroscopy (UVRR) also has an extensive history of nearly four decades and became widespread as laser and detection systems became more sophisticated. The first UVRR spectra of nucleic acids and UV preresonance Raman spectra of small molecules were acquired in 1975 by a doubled Ar ion laser at 257 nm,[28,29] followed by preresonance Raman studies of benzene derivatives with a nitrogen dye laser.[30] These and other intracavity-doubled CW lasers are excellent for UVRR experiments because they offer inherently narrow spectral bandwidths that give rise to high-resolution spectra. Additionally, photolysis with CW lasers results in minimal photodamage relative to pulsed systems. The drawback of CW lasers is that they are not tunable, with wavelengths limited to harmonics of the lasing medium; useful wavelengths for UVRR studies of proteins are 228.9 and 206.5 nm from doubled argon and krypton ion lasers, respectively. Greater tunability is achieved with pulsed lasers, including Nd:YAG and Ti:sapphire systems, that pump other media, such as Raman shifters that contain a variety of gases (H_2, D_2, etc.), nonlinear crystals for frequency conversion, and dye lasers.

Currently, the most widespread UVRR systems utilize kilohertz nanosecond Ti:sapphire lasers combined with harmonic generation. In this setup, the laser can typically be tuned from ~700 to 960 nm and the third and fourth harmonics provide wavelengths in the UV region of approximately 195–240 nm.[22,31–35] The advantages of this system are numerous: the high repetition rate minimizes the probability for nonlinear phenomena in the sample, the data collection time is reasonable, nanosecond pulses ensure narrow bandwidths that are suitable for UVRR, and the system is entirely solid-state and, therefore,

is robust and straightforward to operate. However, as with all pulsed lasers, high pulse energies can cause significant photodamage, and the concentration of photodamaged sample can continuously increase in the sample reservoir if one utilizes a recirculating system. The 1 kHz repetition rate of a standard Ti:sapphire laser system combined with a single-pass microcapillary flow system is ideal for preventing the accumulation of photoproducts; the illuminated sample volume in a capillary or liquid jet can be replenished between laser pulses, and the photolyzed sample can be discarded. With the right balance among the sample flow rate, capillary diameter, and laser spot size, sample usage and signal can be optimized. For example, a 10 min single-pass Raman measurement of a small (30 kDa) protein may require ≤1 mg of sample for a reasonable signal-to-noise ratio (S/N).

One of the most difficult aspects of UVRR is rejection of Rayleigh scattering. With 228.0 nm excitation, a 200 cm^{-1} Raman-shifted photon has a wavelength of 229.0 nm, which is only 1.0 nm shifted from the excitation wavelength. As a comparison, the same 200 cm^{-1} Raman-shifted photon with 514.5 nm excitation is separated from the excitation wavelength by 5.3 nm. This difference illustrates one of the biggest challenges of UVRR: it is difficult to obtain a commercial UV cutoff filter that can effectively separate 228.0 and 229.0 nm, whereas visible cutoff filters can easily separate 514.5 and 519.8 nm. For this reason, the majority of Rayleigh rejection is accomplished with high-throughput prefilters or other modified dispersing systems. Some examples of filters used in UVRR experiments include low-dispersion, prism-based prefilters,[36–38] modified double monochromators,[32,33,39] and a spatial filter.[40]

5.4 Application of Time-Resolved, Visible Resonance Raman Spectroscopy

5.4.1 Protein Chromophores Investigated by Resonance Raman

Visible resonance Raman spectroscopy has been applied to a wide range of colored proteins and related model compounds. Because the Raman effect is weak, chromophores that exhibit low fluorescence and high absorptivity have been the main subjects of this technique. Heme and retinal proteins are ideal for resonance Raman spectroscopy, and as such, these cofactors have been and continue to be studied extensively. Metal–ligand bonds, such as those in iron containing (e.g., ferredoxin) and copper-containing (e.g., azurin) proteins, have also been investigated by resonance Raman spectroscopy. It has been possible to study fluorescent chromophores, including flavins[41] and chlorophylls,[42,43] using fluorescence rejection techniques, such as gated detection[44,45] and shifted excitation Raman difference spectroscopy (SERDS),[46] as well as fluorescence quenching methods.[41] In the past decade, stimulated Raman spectroscopy has allowed Raman investigations of molecules with near unity fluorescence quantum yields, e.g., laser dyes and fluorescent proteins.[42,47] FSRS has become a powerful modern tool; the combination of femtosecond time resolution and insensitivity to fluorescence has allowed researchers to investigate complex dynamics without complications from fluorescence, such as excited-state proton transfer in green fluorescent protein.[47] Examples of proteins and cofactors investigated via visible resonance Raman spectroscopy are shown in Figure 5.2. Here we discuss both historical and modern experiments of one of the most widely studied photoactive proteins, rhodopsin.

5.4.2 Rhodopsin

Rhodopsins make up a class of photo-receptors that utilize a retinal chromophore as the light absorber. These proteins are found in eukaryotes, bacteria, and archaea and are essential for organism survival and adaptation to the environment.[48] The two most widely studied retinal proteins are the mammalian visual pigment, rhodopsin, and the microbial proton pump, bacteriorhodopsin. Despite a divergence in function, they share a common mechanism for photoactivation, which is photoisomerization of a retinal chromophore. In both proteins, the retinal chromophores are attached to lysine residues via a protonated Schiff base linkage and are located in the center of a membrane-embedded, seven-α-helix structure. Because of the low fluorescence quantum yields and high molar absorptivities of the reactants and photointermediates, rhodopsin and bacteriorhodopsin, as well as other retinal proteins, have been investigated extensively with resonance Raman spectroscopy.

The visual pigment rhodopsin, herein simply termed rhodopsin, is the protein responsible for vision in all vertebrates, mollusks, and arthropods. It is a well-studied G protein-coupled receptor (GPCR) and, in fact, was the first GPCR to be crystallized in 2000.[49] Early photochemical studies of mammalian rhodopsin were led by Wald and co-workers, who demonstrated in the early 1950s that the molecular basis of vision is the 11-*cis*-to-*trans* photoisomerization of a protein-bound retinal chromophore that absorbs maximally at 498 nm.[50] These and other foundational discoveries in vision were

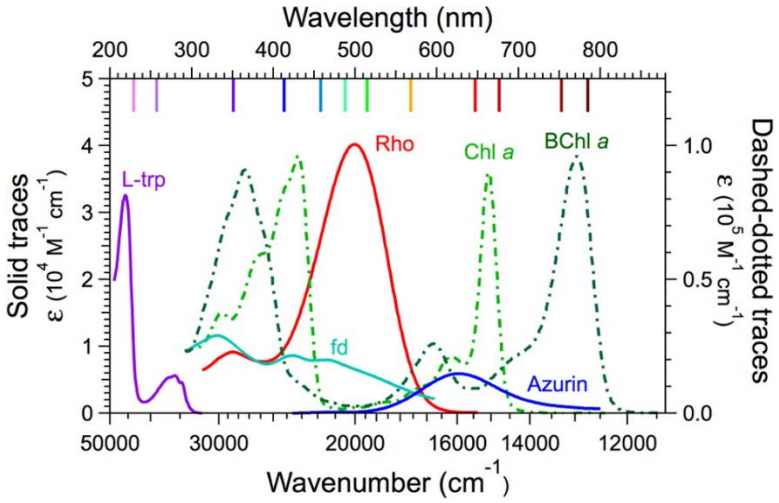

Figure 5.2 Absorption spectra of some biomolecules studied by resonance Raman spectroscopy. Spectra are for the amino acid Ltryptophan (L-trp), and proteins ferredoxin (fd), bovine rhodopsin (Rho), azurin, chlorophyll a (Chl a), and bacterial chlorophyll a (BChl a). Representative excitation wavelengths from frequency-doubled or fundamental lines of argon ion 228.9, 257.2, 351.1, 457.9, 488.0, and 514.5 nm), krypton ion (413.1, 568.2, 647.1, 676.4, and 752.5 nm), and diode (785 nm) lasers are indicated as vertical lines along the top. Note the two scales of molar absorptivity for solid (left axis) and dashed−dotted (right axis) traces. The absorption spectrum of fd is from ref 167, and spectra of Chl a and BChl a are from refs 168 and169.

recognized by a Nobel Prize in 1967, and several years later, the first resonance Raman spectra of rhodopsin from intact bovine retinae[7] and solubilized in detergent[51] were reported.

The initial, groundbreaking resonance Raman studies were followed by a suite of rapid-flow, low-temperature, and pump–probe experiments that revealed the ground-state structures of rhodopsin and its photoproducts and thermal products. The first resonance Raman spectrum of the 77 K-trapped all-trans photoproduct,[52] called bathorhodopsin (λ_{max} = 543 nm), exhibited unusually intense peaks at 856, 877, and 920 cm^{-1} that were not present in resonance Raman spectra of the model compound, the all-trans protonated Schiff base. These resonance Raman and related transient absorption spectra led some to hypothesize that bathorhodopsin was not an all-trans species but instead reflected a cis structure that had undergone proton translocation[53] or tautomerization.[54] These hypotheses were shown to be incorrect, and subsequent low-temperature resonance Raman studies of isotopic derivatives led Mathies and co-workers to properly assign the intense bathorhodopsin peaks to hydrogen-out-of-plane (HOOP) modes of a highly strained and distorted all-trans chromophore.[55,56] Resonance Raman spectroscopy was key in establishing that the bathorhodopsin all-trans retinal chromophore is not planar, but instead, exhibits ~40° dihedral twists about the C_{11}=C_{12} and C_{12}–C_{13} bonds because of protein–chromophore interactions.[57] This distorted photoproduct also exists at room temperature and appears within hundreds of femtoseconds following photon absorption.[58] The relevance of this distorted chromophore in bathorhodopsin has been the subject of many papers. It is now well accepted that a significant fraction of the photon energy is stored in

these distortions, and that this strained chromophore ultimately drives global protein conformational changes for G protein activation.[57]

Other intermediates have also been investigated in detail with both low- and roomtemperature resonance Raman spectroscopy; the room-temperature measurements were performed with time-resolved methods, such as fast-flow and pump–probe spectroscopy. Bathorhodopsin converts to the blue-shifted intermediate (BSI, λ_{max} of 477 nm), and this conversion is accompanied by partial relaxation in the all-trans structure.[59] The chromophore continues to relax and transfer energy to the surrounding protein as BSI decays to lumirhodopsin (λ_{max} = 492 nm), followed by Meta I (λ_{max} = 478 nm).[60] This relaxation is evident in the comparison of the resonance Raman spectra of rhodopsin,[58] bathorhodopsin,[58] and lumirhodopsin[60] in Figure 5.3; the intense, ~850 cm^{-1} HOOP modes appear in bathorhodopsin but are absent in rhodopsin and lumirhodopsin. A comparison of the protein and chromophore structures based on X-ray diffraction highlights the surprising similarity between the 11-cis (rhodopsin) and distorted all-trans (bathorhodopsin) species and shows the subsequent structural changes in the relaxed lumirhodopsin form (Figure 5.3). This analysis of rhodopsin and bathorhodopsin illustrates that resonance Raman spectra of two species may exhibit significant differences despite relatively minor variations in crystallographic structures. Meta I decays to Meta II (λ_{max} = 380 nm), which exhibits a deprotonated all-trans retinal; Meta II is the signaling state of rhodopsin during which the G protein, transducin, is activated to initiate the enzymatic cascade. Finally, the retinal chromophore is released to yield the apoprotein opsin and all-trans retinal.

Our understanding of the chromophore dynamics as well as the global protein response associated with the isomerization reaction has been enhanced through time-resolved resonance Raman experiments. Picosecond visible pump–probe and femtosecond stimulated Raman spectroscopy (FSRS) experiments demonstrated that the highly strained, all-trans chromophore of bathorhodopsin is present within 200 fs following photon absorption;[58,61] this time scale was consistent with transient absorption data[62] that had been reported at least 10 years prior to these resonance Raman studies. Analysis of the FSRS data further indicated that the photoproduct approaches its equilibrium structure in ~140 fs,[63] and picosecond antiStokes experiments revealed vibrational cooling of the chromophore in ~3 ps.[64] Transfer of the photon energy from the distorted chromophore to surrounding protein binding pocket has also been investigated with time-resolved UVRR spectroscopy (see below).

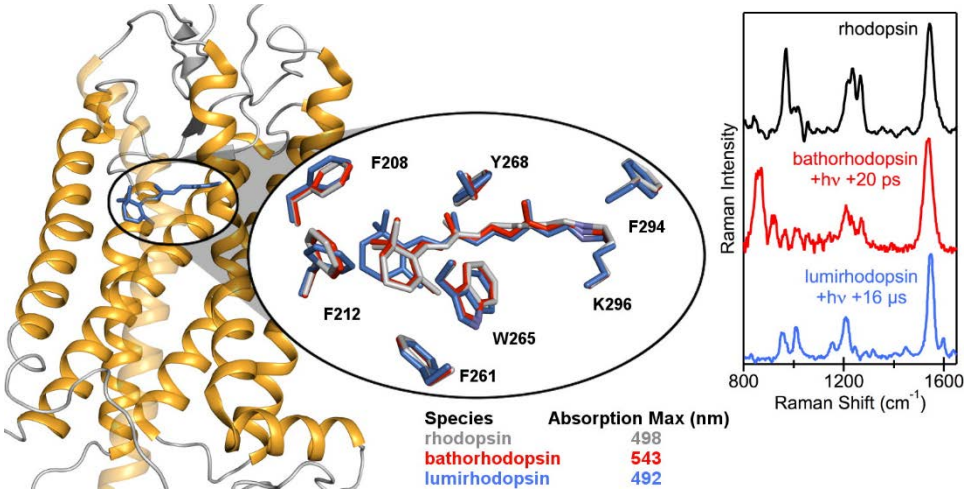

Figure 5.3. Crystal structures and resonance Raman spectra of rhodopsin (gray) and two photointermediates, bathorhodopsin (red) and lumirhodopsin (blue). The protein backbone is shown as yellow ribbons and corresponds to that of rhodopsin. Crystal structures are from Protein Data Bank entries 1U19 (rhodopsin), 2G87 (bathorhodopsin), and 2HPY (lumirhodopsin). Tryoptophan, tyrosine, and phenylalanine residues within 4.5 Å of the retinal chromophore are shown; Y178 has been omitted to preserve the unobstructed view of the binding pocket. Pump−probe time delays for resonance Raman spectra are indicated. Raman spectra are from refs 58 (rhodopsin and bathorhodopsin) and 60 (lumirhodopsin).

5.5 Ultraviolet Resonance Raman (UVRR) Spectroscopy

5.5.1 Protein Chromophores Investigated by UVRR

UV lasers have extended the application of resonance Raman spectroscopy to chromophores that absorb UV light and are prevalent in all proteins, such as amide backbone, aromatic amino acids, proline, and, to a lesser extent, sulfur-containing residues.[65,66] As was demonstrated for visible resonance Raman spectroscopy, selectivity in UVRR is also achieved by tuning the excitation wavelength. For example, the backbone carbonyl $\pi \rightarrow \pi^*$ transition is intense at wavelengths below ~210 nm, so excitation near 200 nm preferentially probes secondary structure. On the other hand, higher-wavelength excitation (~230 nm) probes side-chain structure. This selectivity is illustrated in the UVRR spectra of the peptide melittin, which has the primary sequence GIGAVLKVLTTGLPALISWIKRKRQQ. Figure 5.4 shows that 210 nm excitation of melittin gives rise to a UVRR spectrum of the backbone that is different from that of the 230 nm spectrum of the single tryptophan residue at position 19.

5.5.1.1 Secondary Structure

The UVRR spectrum of amide backbone can be used to characterize secondary structure because of the sensitivity of vibrational frequencies to the hydrogen bonding environment. Intense UVRR bands appear for vibrations that involve carbonyl and amide functional groups: amide I (predominantly C=O stretch), amide II (~60% N–H bend + ~40% C–N stretch), and amide III (~40% C–N stretch + ~30% N–H bend) modes.[67] In addition to these well-known amide modes, the amide IIp mode of proline and the amide S mode are also utilized in UVRR spectroscopy.[66,68,69] Analysis of the amide III (~1250–

1350 cm^{-1}), amide II (~1520–1560 cm^{-1}), amide I (~1630–1680 cm^{-1}), and amide S (~1390 cm^{-1}) regions reveals the relative content of random coil, α-helix, and βsheet secondary structure in proteins and peptides.[68,70,71] A summary of vibrational normal modes and their correlation to structure and environment in UVRR spectra of proteins is presented in Table 5.1.

The information gained from UVRR analysis of the backbone may be compared to results from far-UV (190–250 nm) circular dichroism (CD) measurements. Because normal-mode frequencies may reflect variations in backbone dihedral angles, UVRR can report on a single turn of an α-helix.[72] In contrast, CD reports on the global average of the secondary structure of the peptide because of the effects of exciton coupling.[73] A consequence of this difference is that UVRR intensities scale linearly with the fraction of α-helix whereas in CD spectroscopy, the molar ellipticity per residue decreases as α-helical content decreases, and a threshold length of α-helix must persist to give reliable results in a CD spectrum.[74] Exciton coupling is especially important in CD spectra of short peptides. Short α-helical peptides result in CD spectra with variations in peak positions and relative intensities.[75] An additional challenge inherent to CD spectroscopy is that highly scattering samples are difficult to investigate. Differential light scattering and absorption flattening from particles, such as membrane vesicles, may alter the observed shapes and relative intensities in CD spectra.[76] Finally, CD spectra are broad and generally featureless relative to UVRR spectra and, therefore, do not easily reveal fractional contributions of mixed α–β sheet secondary structures. In summary, UVRR is an attractive alternative to far-UV CD

spectroscopy that will provide additional insights into the secondary structures of challenging systems.

5.5.1.2 Aromatic Amino Acids

The majority of UVRR studies of side chains focus on tryptophan, tyrosine, and histidine because these aromatic residues have strong Raman peaks that report on structure, environment, and protonation state (see Table 5.1).[77–87] Phenylalanine, like tyrosine and tryptophan, also exhibits strong resonance Raman peaks whose intensities depend on the absorption cross section at the Raman excitation wavelength. However, in contrast to tryptophan and tyrosine, the Raman peaks of phenylalanine are poor reporters of microenvironment because their peak positions are unchanged in varied solvents.[66] Hence, the UVRR spectrum of phenylalanine is not commonly studied. Off-resonance Raman studies of tryptophan and tyrosine have also played a critical role in interpretation of UVRR spectra.[88–91] These and other Raman studies have established empirical relationships between Raman frequencies/intensities and molecular details, including hydrogen bond strength, microenvironment, static structure, cation–π interactions, and protonation state. Figure 5.5shows UVRR spectra of model compounds of tryptophan (N-acetyl-L-tryptophan ethyl ester), tyrosine (N-acetyl-Ltyrosinamide), and phenylalanine (L-phenylalanine).

Tryptophan exhibits an intense absorption band in the UV, and has consequently been extensively studied by UVRR. Systematic analyses revealed spectral signatures of the

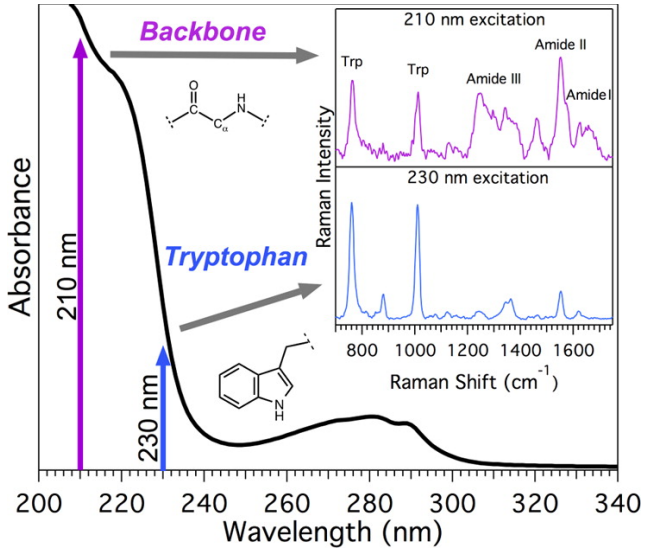

Figure 5.4. UVRR spectra of melittin in random coil conformation in buffer. The excitation wavelength is primarily resonant with the backbone (210 nm) or the single tryptophan residue at position 19 (230 nm). Modes that are enhanced with 210 nm are indicated in the top spectrum.

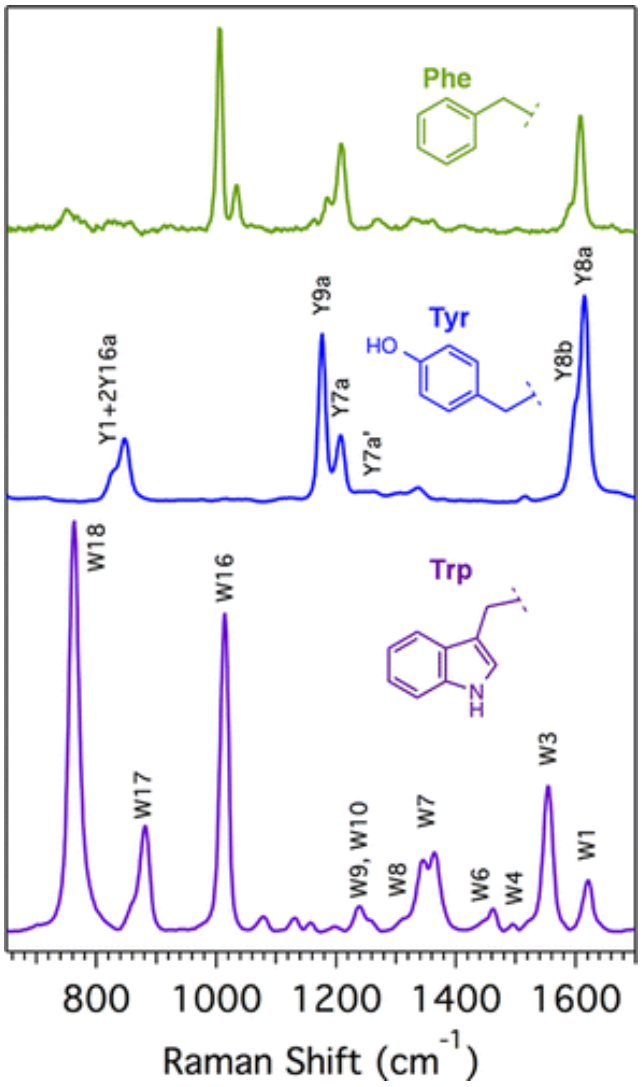

Figure 5.5. 230 nm UVRR spectra of L-phenylalanine (Phe), N-acetyl-Ltyrosinamide (Tyr), and N-acetyl-L-tryptophan ethyl ester (Trp). Amino acid side chains are shown. Labeled peaks correspond to those in Table 5.1.

Table 5.1 UVRR Bands of the Protein Backbone and Residues from refs 65, 66, 81, 85, and 86[a].

chemical group	designation	description	Raman shift (cm^{-1})	properties
tryptophan	W1	benzene ring stretch	1620	environment polarity
tryptophan	W3	CC pyrrole stretch	1552	structure
tryptophan	W4	CH bend + NH bend	1494	H-bonding
tryptophan	W6	NCC stretch + NH bend	1435	H-bonding
tryptophan	W7 doublet	Fermi doublet	1360 and 1340	environment polarity, π-interactions
tryptophan	W8	CC stretch + NH bend	1307	H-bonding
tryptophan	W9, W10	CH bend + NH bend	1230–1250	H-bonding
tryptophan	W16	benzene ring breathing	1004	environment polarity
tryptophan	W17	NH bend	879	H-bonding
tryptophan	HOOP	hydrogen out-of-plane	770–820	π-interactions
tryptophan	W18	indole breathing	760	environment polarity, π interactions
tyrosine	Y8a	ring stretch	1617	H-bonding, protonation state
tyrosine	Y8b	ring stretch	1601	H-bonding, protonation state
tyrosine	Y7a′	CO stretch	1263	proton-accepting strength
tyrosine	Y7a	CC stretch	1210	proton-donating strength
tyrosine	Y9a	CH bend + OH bend	1180	structure
tyrosine	Y1 + 2Y16a	Fermi doublet	850 and 830	H-bonding
histidine in D_2O	N/A	CC stretch and NCN stretch	1577 and 1317	neutral histidine
histidine-D^+ in D_2O	N/A	NCN stretch	1408	protonated histidine
amide backbone	amide I	CO stretch	1630–1680	secondary structure
amide backbone	amide II	CN stretch + NH bend	1520–1560	secondary structure
amide backbone	amide III	CN stretch + NH bend	1250–1350	secondary structure
amide backbone	amide S	CαH bend	1390	secondary structure
Proline	amide IIp	CN stretch of X-Pro	1460	H-bonding, cis/trans

[a] Molecular and environment properties that are correlated to the band positions and intensities are also indicated. Designations and normal-mode descriptions that are not available are indicated N/A.

indole ring that report on local hydrophobicity, the strength of the indole N–H hydrogen bond, and the C_2–C_3–Cβ–Cα torsional angle, $\chi^{2,1}$. Although the near-UV (>250 nm) CD spectrum of tryptophan contains information about hydrophobicity and hydrogen bonding,[92] interpretation can be challenging because of broad and overlapping features of varying sign, and analysis should ideally be aided by UVRR.[93,94] Overall, the breadth of information in a UVRR spectrum of tryptophan makes this an excellent tool for a wide range of biophysical studies.

The ability of UVRR to report on tryptophan is advantageous because this amino acid is one of the most important residues in terms of protein structure, function, and dynamics. It is the least abundant residue in soluble proteins, accounting for only 1.1% of the amino acids expressed in cytoplasmic proteins,[95] but is more prevalent in membrane proteins, with an abundance of 2.9% in transmembrane α-helical domains.[96] This aromatic residue plays key functional roles in proteins because of its unique properties among the 20 natural amino acids: tryptophan exhibits the largest accessible nonpolar surface area that is polarizable, possesses an indole N–H moiety that is capable of hydrogen bond donation, and displays the greatest electrostatic potential for cation–π interactions.[97,98]

These important physical properties render tryptophan an ideal amphiphilic residue. As such, it displays the greatest propensity to reside in the interfacial region of membrane proteins compared to any other naturally occurring amino acid.[99] Tryptophan has been found to stabilize membrane-spanning proteins and peptides by acting as anchors along the interface of the bilayer.[100,101] Replacement of tryptophan residues with phenylalanine in the 325-residue integral membrane protein, outer membrane protein A, destabilizes the

protein relative to the wild type when the protein is folded into lipid bilayers.[102,103] Tryptophan residues in membrane-associated antimicrobial peptides also play important functional roles in hemolytic and bactericidal activity.[104,105] These and other examples illustrate that the presence, location, and environment of tryptophan residues are critical in the study of folding and insertion of membrane proteins and membrane-associated peptides.

5.5.2 Applications of UVRR Spectroscopy to Proteins and Peptides

Soluble and membrane proteins have been investigated via UVRR. We briefly describe UVRR studies of soluble proteins and describe recent investigations of more challenging membrane-associated and aggregated proteins and peptides. The choice of biological systems that are discussed is intended to be representative of the array of biomolecules that may be studied as well as the types of scientific questions that may be investigated.

5.5.2.1 Soluble Proteins

A wide range of soluble proteins and scientific questions have been investigated via UVRR. UVRR frequencies and intensities are sensitive to environment, so it is relatively straightforward to correlate UVRR peaks with the local environment of tryptophan and tyrosine residues in proteins, including interactions with metals and charged residues.[80,88,106–111] One advantage of UVRR over electronic tools, such as fluorescence, is that the effects of hydrogen bonding and local dielectric on UVRR peaks are separable, thereby allowing independent investigations of changes in H-bonding or hydrophobicity.[81] Histidine protonation states are easily determined by UVRR studies of

protein in D_2O buffer, and such experiments have been performed on superoxide dismutase and galectins.[112–114] An area with growing use of UVRR is the pharmaceutical industry, in which UVRR experiments have been reported for recombinant therapeutic proteins[115] and antibodies[116] as well as drug binding.[117,118] Time-resolved UVRR experiments have also probed dynamics of heme proteins and photoactive yellow protein,[119–122] and a variety of UVRR experiments have investigated intermediates in protein folding.[123,124] In addition to native side chains and the backbone, other moieties have been interrogated by UVRR, such as unnatural amino acids[125] and flavins.[126] These and other examples illustrate the breadth of information gained from UVRR studies of soluble proteins.

5.5.2.2 Membrane Proteins

Membrane proteins have also been investigated by UVRR, but these systems are more challenging to study than soluble proteins because of limited sample quantities and high background scattering from vesicles or micelles. Bacteriorhodopsin and rhodopsin are perhaps the most well-studied membrane proteins, with UVRR papers on bacteriorhodopsin first appearing nearly 25 years ago.[127,128] Since these initial reports, other steady-state and pump–probe UVRR experiments have elucidated changes in structure during the bacteriorhodopsin photocycle, such as modifications in local and hydrogen bonding environments of tyrosine and tryptophan residues, opening of a water-permeable channel, and the picosecond-to-nanosecond response of protein pocket to isomerization reaction.[129–135] Experiments on the visual pigment rhodopsin have also been reported.[34,136,137] The insights gained from these UVRR studies have revealed the response of the retinal binding pocket to photon absorption. For example, it has been shown that

there is a 3 ps response of tryptophan and tyrosine residues to the photoisomerization reaction.[34] A small number of other detergent-solubilized membrane proteins have also been investigated, such as photosystem II,[138] cytochrome *c* oxidase,[139] and cytochrome bc_1 complex.[140] In the past several years, UVRR experiments have been extended to a membrane protein embedded in a synthetic lipid bilayer.[141,142] In particular, UVRR studies of outer membrane protein A (OmpA) and its mutants revealed tryptophan–lipid interactions during the insertion and folding of OmpA into bilayers of small unilamellar vesicles.[141,142] The ability to gain insight into the dynamics of membrane proteins is an important advantage of UVRR and allows for investigations of complex reactions and systems that may not be amenable to traditional tools such as NMR or crystallography.

5.5.2.3 Model Peptides for Soluble and Membrane Protein Folding

Small peptides provide an excellent opportunity to investigate protein folding. Model peptides are especially valuable for studies of membrane protein folding because experiments and data analysis can be simplified. Additionally, the expression and purification of large quantities of integral membrane proteins is a challenging task, whereas membrane-associated peptides can be synthesized in sufficient quantities. UVRR spectroscopy is well-suited for the study of membrane-associated biomolecules because the presence of lipid vesicles and detergents does not complicate the spectra.[142]

Several groups have measured UVRR spectra of small peptides to study the structures and kinetics of soluble protein folding. Asher and co-workers,[143] for example, have studied the kinetics and thermal stability of α-helix-like soluble peptides. In contrast, only a small number of model membrane peptides have been studied. One such model

membrane peptide, N-acetyl-tryptophan-pentaleucine (AcWL5), was found to have β-sheet-type structure in lipid vesicles based on results obtained from UVRR spectra;[144] this finding is in accordance with the β-sheet oligomeric structure previously reported for AcWL5.[145] The UVRR spectrum revealed that the tryptophan residue in AcWL5 is hydrogen-bonded in a hydrophobic region of the lipid bilayer. This result provides a molecular description of how tryptophan is able to help stabilize membrane proteins.[100] The hydrophobic α-helical model membrane peptide, ME1, has also been investigated using UVRR spectroscopy. ME1 is a 32-residue transmembrane helix segment of the natural membrane protein glycophorin A that has five additional mutations. Comparison of the UVRR spectrum of this peptide to that of the soluble α-helical protein myoglobin led to the conclusion that the intensity of UVRR amide bands serves as a reliable marker to identify lipid-solubilized and solvent-exposed helical structure in proteins.[146] A final example of a membrane-associated peptide for folding studies is the α-helical, pH low insertion peptide (pHLIP). This peptide exhibits structural changes as a function of pH, and UVRR experiments determined that this peptide is desolvated and structured as a membrane-associated peptide.[147]

5.5.2.4 Antimicrobial Peptides (AMPs)

While the membrane peptides described above serve as model systems for protein folding, some small membrane-active peptides fold and insert into lipid bilayers and function as membrane disruptors. One such class of peptides is antimicrobial peptides (AMPs). AMPs are an ancient component of innate immunity that are selectively toxic to bacteria[148] and are crucial for the survival of many organisms that do not possess

lymphocytes or antibodies important for immunity, such as insects.[149] AMPs typically have fewer than 50 residues and generally exhibit segregated regions of cationic and hydrophobic amino acid residues that give rise to an amphiphilic structure for binding to membranes.[149] In the presence of a bilayer, they form α-helices or rigid β-sheet structures with disulfide bridges and often exhibit primary sequences with an unusually high abundance of select amino acids.[148,150] Mutation or deletion of certain residues, including tryptophan, has been found to be detrimental to the activity of many AMPs.[104,151–153] These peptides are water-soluble yet spontaneously insert into membranes and, therefore, have properties of both soluble and membrane proteins. The observation that bacteria do not develop resistance to AMPs suggests that AMPs may serve as a novel class of antibiotics to combat antibiotic-resistant bacteria. This potentially transformative use of AMPs motivates UVRR and other studies of the mechanisms of membrane disruption.

The mechanisms of AMP insertion and folding into membranes are not well understood. Electrostatic interaction between cationic AMPs and anionic bacterial membranes is important for initial peptide–membrane binding. However, the formation of salt bridges does not fully explain the selectivity of AMPs for bacterial over eukaryotic membranes. Several models of AMP disruption mechanisms have been proposed. In one model, AMPs carpet the membrane, causing an increase in the permeability of the membrane. AMPs may form pores that cause ions and molecules to leak out through the membrane. It has also been proposed that AMPs simply act to dissolve the membrane in a manner similar to that of a detergent.[148]

One example of an AMP that has been successfully studied by UVRR is the human cathelicidin, LL-37.[154] This AMP is expressed primarily in neutrophils and epithelial cells and shows broad-spectrum antimicrobial activity.[155] An important goal of this project was to elucidate the microenvironment of the peptide buried in a bilayer and thus shed light on the mechanisms of membrane disruption. In this study, phenylalanine residues at positions 6 and 17 were replaced with tryptophan residues and yielded the two single-tryptophan mutant peptides F6W and F17W. These mutations did not alter the antimicrobial activity or the overall secondary structure compared to those of wild-type peptide LL-37. On the basis of results obtained from fluorescence quenching experiments and UVRR spectroscopy, the positions of tryptophan residues for both mutants were found to be deeply buried in the lipid bilayer (~12 Å from the bilayer center) of mixed anionic/zwitterionic lipid vesicles (bacterial membrane mimics). UVRR data revealed a decrease in hydrogen bonding and environment polarity for both tryptophan residues upon folding and insertion of the peptide into the lipid bilayer; this finding is consistent with deep insertion of the aromatic residues into the bilayer. The UVRR results, combined with fluorescence and CD data, ruled out a detergent like mode of action for this AMP and, instead, supported carpeting and/or toroidal pore mechanisms.

The UVRR and fluorescence results complement previous NMR studies by Ramamoorthy and colleagues.[156] Both studies support the possible mechanisms of carpeting and/or toroidal pore and suggest that the orientation of LL-37 in the bilayer is parallel, not perpendicular, to the bilayer surface. The solid-state NMR experiments also suggested that LL-37 lies at the bilayer surface and is immobilized. One of the strengths of UVRR is the ability to reveal microscopic detail near the tryptophan residue without the

need for isotopic labeling or high concentrations typical of NMR studies. The UVRR results suggest that tryptophan is not interacting with lipid headgroups but, instead, is likely buried in the hydrocarbon core of the bilayer. Analysis of the W18 and W16 tryptophan modes suggests that possible intramolecular cation–π interactions may stabilize one of the buried tryptophan residues in the bilayer. UVRR data also directly reveal differences in the level of hydration among random coil, soluble oligomer, and vesicle-bound forms of LL-37. Collectively, these molecular insights augment structural information that is gained through NMR studies and deepen our understanding of LL-37.

The AMPs lactoferricin B (LfB) and pEM-2 have also been investigated using UVRR spectroscopy.[157] LfB is an α-helical 25-residue peptide composed of a segment of bovine lactoferrin, and pEM-2 is a modified 13-residue peptide derived from myotoxin isolated from Bothrops asper snake venom. Both peptides have tryptophan residues that are important for AMP activity against Gram-negative and -positive bacteria.[158,159] As revealed by UVRR experiments, the hydrophobicity of tryptophan environments increased when both peptides were introduced into the helix-inducing solvent 2,2,2-trifluoroethanol. Additionally, the hydrophobicity near the tryptophan residues of LfB did not increase in the presence of purely zwitterionic lipid vesicles (eukaryotic membrane mimic). However, the hydrophobicity was enhanced in the presence of anionic lipid vesicles (bacterial membrane mimic), indicating that LfB preferentially folds and inserts into lipid bilayers that mimic bacterial membranes.

Similar results were found for the anoplin peptide, an α-helical peptide isolated from the venom of the wasp Anthemis samariensis.[160] Modifications in the primary

structure of the peptide, including full substitutions of L-amino acids for D-amino acids and C-terminal deamidation, did not change the overall secondary structure of the peptide based on the results obtained with UVRR spectroscopy. Furthermore, it was found that all modified forms of the peptide adopted α-helical secondary structure in the presence of anionic lipid vesicles.

Very little peptide structure was observed in the presence of zwitterionic lipid vesicles, further confirming the preferential binding of AMPs for anionic synthetic lipid bilayers.

A final example that illustrates the utility of UVRR experiments is the chimeric peptide CM15, which is a hybrid peptide comprised of seven residues from the AMP cecropin (from silk moth) and eight residues from the toxic peptide melittin (from honeybee venom).[161] CM15 is engineered to combine the best of two worlds: it is potent, like melittin, but selective and nonhemolytic, like cecropin. UVRR analysis of CM15 with both 228 and 210 nm excitation led to the surprising result that unlike typical AMPs and toxins, CM15 retains a predominantly unfolded, hydrated, conformation when bound to vesicles comprised of zwitterionic lipids. Even more unexpected was the finding that this unfolded CM15 is a potent membrane disruptor as assessed by fluorescence leakage assays. UVRR spectra of melittin, cecropin, and the hybrid CM15 in three different environments are shown in Figure 5.6; all three peptides are unfolded in buffer and fully folded as α-helices in the presence of anionic lipid vesicles. The fraction of α-helix in the presence of zwitterionic lipids was determined by using the unfolded and fully folded spectra as basis spectra. CM15 was found to be only 23% α-helical when bound to zwitterionic vesicles,

but it was nearly as potent as melittin (89% α-helical) in terms of membrane disruption. This finding that an engineered, hybrid peptide exhibits high potency as an unfolded peptide suggests that new models for peptide–membrane interactions may be needed.[161]

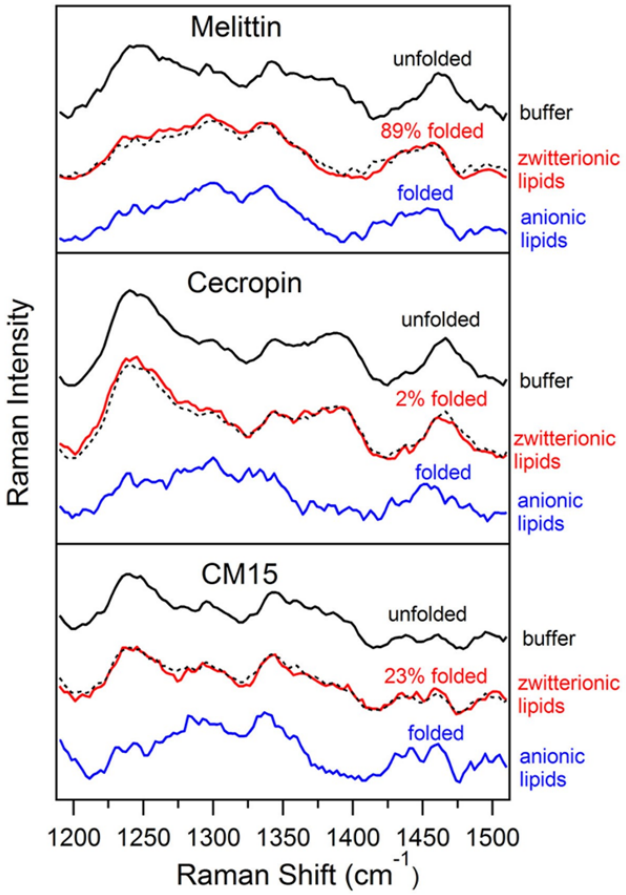

Figure 5.6. 210 nm UVRR spectra of melittin, cecropin, and CM15 in three different environments of buffer (fully unfolded), zwitterionic lipid vesicles (partially folded), and anionic lipid vesicles (fully folded). Fraction folded in zwitterionic lipids was determined by linear combination of fully folded and unfolded spectra, and best fits are shown as black dashed curves that overlay red curves. Resulting fractions are indicated. This figure is adapted from ref 161. See the text for details.

5.5.2.5 Fibril-Forming Peptides

Another family of challenging biomolecules consists of the aggregation-prone disordered peptides. Amyloid-β (Aβ) is an intrinsically unstructured peptide (29–43 amino acids) derived from proteolysis of the larger Aβ precursor protein. For reasons that are not yet understood, Aβ forms well-ordered insoluble aggregates, or fibrils, that collect as plaques in the brains of Alzheimer's patients. Because of the unique properties of this peptide, techniques typically utilized to elucidate protein structure, such as X-ray crystallography and solution NMR, are not well-suited for studying the structures of the biologically relevant, unfolded forms of this peptide.[162] UVRR spectroscopy, however, does not require a crystalline or homogeneous phase and, therefore, can be used to elucidate structures of disordered peptides and proteins, including fibrils and heterogeneous aggregates. An additional benefit is that UVRR spectroscopy specifically reports on hydrogen bonding networks that give rise to peptide secondary structure, local hydrophobicity, and tertiary contacts that are known to be associated with aggregate formation.[163,164] In the context of these advantages, UVRR spectroscopy, in particular deep UV (<200 nm excitation), is ideally suited for the study of Aβ and other peptides that may be linked to neurodegenerative disorders.

A relatively small number of UVRR studies of Aβ peptides have been published. The deep UVRR spectra of Aβ peptides that form either parallel or antiparallel β-sheets have been characterized. It was reported that these different β-sheet motifs of amyloid fibrils could be distinguished via UVRR.[165] This study further indicated that the parallel β-sheet conformation in fibrils is different from the analogous β-sheets in soluble proteins.

In contrast, antiparallel β-sheet conformations were described to be similar for both fibrils and soluble proteins. In another study, myricetin, a flavenoid known to interact with Aβ, was observed to inhibit amyloid formation of Aβ via a thioflavin T assay. Additionally, results from CD and UVRR experiments revealed that myricetin altered the conformation of the hydrophobic segment of the peptide and may interact with the aromatic amino acids present in Aβ. This finding indicates that UVRR spectroscopy may be sensitive to changes in peptide structure when anti-amyloidogenic small molecules are introduced into the sample.[166] These important discoveries on the structure of Aβ in amyloid fibrils underscore the flexibility of UVRR spectroscopy and the level of molecular detail that can be attained by this technique.

5.6 Conclusion

Resonance Raman spectroscopy is a valuable optical technique that elucidates structures and dynamics of biomolecules. A primary advantage of this method over other vibrational and structural tools is the ability to interrogate select portions of the protein by tuning the excitation wavelength to within an absorption band of the chromophore of interest. Given the widespread availability of robust and tunable UV-to-visible lasers, it is now relatively straightforward to obtain resonance Raman spectra of the protein backbone, side chains, and colored prosthetic groups. In combination with modern pulsed methods, resonance Raman spectroscopy is able to reveal structural changes and functional dynamics of biomolecules over all relevant time scales, from femtoseconds to seconds. These benefits make resonance Raman spectroscopy an excellent complement to the many other tools used in the study of the most complex and experimentally challenging biomolecules.

5.7 Acknowledgments

I.L.-P. acknowledges generous support from a UCSD National Institutes of Health Molecular Biophysics Training Grant Fellowship and a Department of Education Graduate Assistance in Areas of National Need (GAANN) Fellowship. We acknowledge the National Science Foundation for supporting our research program. We thank Prof. Michael Tauber for valuable feedback.

Chapter 5, in full, is a reprint of our previously published work. Reproduced with permission from Lopez-Peña, I; Leigh, B. S.; Schlamadinger, D. E.; Kim, J. E; *Biochemistry* **2015**, 54, 4770-4783. Copyright 2015 American Chemical Society. The dissertation author was the primary investigator and author of this paper.

5.8 References

1. Raman, C. V.; Krishnan, K. S., A new type of secondary radiation. *Nature* **1928,** *121*, 501-502.

2. Singh, R., C. V. Raman and the discovery of the Raman effect. *Phys. Perspect.* **2002,** *4*, 399-420.

3. McCreery, R. L., *Raman Spectroscopy for Chemical Analysis*. Wiley Interscience: New York, 2000.

4. Merlin, J. C., Resonance Raman spectroscopy of carotenoids and carotenoid-containing systems. *Pure Appl. Chem.* **1985,** *57*, 785-792.

5. Carey, P. R., *Biochemical applications of Raman and Resonance Raman spectroscopies*. Academic Press: New York, 1982.

6. Myers, A. B.; Mathies, R. A., Resonance Raman Intensities: A Probe of Excited-State Structure and Dynamics. In *Biological Applications of Raman Spectroscopy*, Spiro, T. G., Ed. John Wiley and Sons, Inc.: New York, 1984; Vol. 2, pp 1-58.

7. Rimai, L.; Kilponen, R. G.; Gill, D., Resonance-enhanced Raman spectra of visual pigments in intact bovine retinas at low temperatures. *Biochem. Biophys. Res. Commun.* **1970,** *41*, 492-497.

8. Gill, D.; Kilponen, R. G.; Rimai, L., Resonance Raman scattering of laser radiation by vibrational modes of carotenoid pigment molecules in intact plant tissues. *Nature* **1970,** *227*, 743-744.

9. Strekas, T. C.; Spiro, T. G., Hemoglobin: Resonance Raman spectra. *Biochim. Biophys. Acta* **1972,** *263*, 830-833.

10. Brunner, H.; Mayer, A.; Sussner, H. J., Resonance Raman scattering on the haem group of oxy- and deoxyhaemoglobin. *J. Mol. Biol.* **1972,** *70* (153-156).

11. Strekas, T. C.; Spiro, T. G., Cytochrome c: Resonance Raman spectra. *Biochim. Biophys. Acta* **1972,** *278*, 188-192.

12. Warshel, A., Interpretation of Resonance Raman spectra of biological molecules. *Annu. Rev. Biophys. Bioeng.* **1977,** *6*, 273-300.

13. Deng, H.; Callender, R., Raman spectroscopic studies of the structures, energetics, and bond distortions of substrates bound to enzymes. *Methods Enzymol.* **1999,** *308*, 176-201.

14. Moffat, K., Time-resolved biochemical crystallography: A mechanistic perspective. *Chem. Rev.* **2001,** *101*, 1569-1581.

15. Gardner, K. H.; Kay, L. E., The use of H-2, C-13, N-15 multidimensional NMR to study the structure and dynamics of proteins. *Annu. Rev. Biophys. Biomol. Struct.* **1998,** *27*, 357-406.

16. Terner, J.; Spiro, T. G.; Nagumo, M.; Nicol, M. F.; El-Sayed, M. A., Resonance Raman spectroscopy in the picosecond time scale: The carboxyhemoglobin photointermediate. *J. Am. Chem. Soc.* **1980,** *102*, 3238-3239.

17. Hayward, G.; Carlsen, W.; Siegman, A.; Stryer, L., Retina chromophore of rhodopsin photoisomerizes within picoseconds. *Science* **1981,** *211*, 942-944.

18. Doig, S. J.; Reid, P. J.; Mathies, R. A., Picosecond time-resolved resonance Raman spectroscopy of bacteriorhodops's J, K, and KL intermediates. *J. Phys. Chem.* **1991,** *95*, 6372-6379.

19. Petrich, J. W.; Martin, J. L.; Houde, D.; Orszag, A., Time-resolved Raman spectroscopy with subpicosecond resolution: Vibrational cooling and delocalization of strain energy in photodissociated (carbonmonoxy)hemoglobin. *Biochemistry* **1987,** *26*, 7914-7923.

20. Gustafson, T. L.; Roberts, D. M.; Chernoff, D. A., Picosecond transient Raman spectroscopy: The photoisomerization of trans-stilbene. *J. Chem. Phys.* **1983,** *79*, 1559-1564.

21. Uesugi, Y.; Mizutani, Y.; Kitagawa, T., Developments of widely tunable light sources for picosecond time-resolved resonance Raman spectroscopy. *Rev. Sci. Instrum.* **1997,** *68*, 4001-4008.

22. Zhu, L.; Kim, J.; Mathies, R. A., Picosecond time-resolved Raman system for studying photochemical reaction dynamics to the primary events in vision. *J. Raman Spectrosc.* **1999,** *30*, 777-783.

23. Kruglik, S. G.; Lambry, J. C.; Martin, J. L.; Vos, M. H.; Negrerie, M., Sub-picosecond Raman spectrometer for time-resolved studies of structural dynamics in heme proteins. *J. Raman Spectrosc.* **2011,** *42* (3), 265-275.

24. McCamant, D. W.; Kukura, P.; Mathies, R. A., Femtosecond time-resolved stimulated Raman spectroscopy: application to the ultrafast internal conversion in b-carotene. *J. Phys. Chem. A* **2003,** *107* (40), 8208-8214.

25. Kukura, P.; McCamant, D. W.; Mathies, R. A., Femtosecond stimulated Raman spectroscopy. *Annu. Rev. Phys. Chem.* **2007,** *58*, 461-488.

26. Yoshizawa, M.; Hattori, Y.; Kobayashi, T., Femtosecond time-resolved resonance Raman gain spectroscopy in polydiacetylene. *Phys. Rev. B* **1994,** *49*, 13259-13262.

27. Laimgruber, S.; Schreier, W. J.; Schrader, T.; Koller, F.; Zinth, W.; Gilch, P., The photochemistry of *o*-nitrobenzaldehyde as seen by femtosecond vibrational spectroscopy. *Angew. Chem., Int. Ed.* **2005,** *44*, 7901-7904.

28. Pézolet, M.; Yu, T. J.; Peticolas, W. L., Resonance and preresonance Raman spectra of nucleotides using ultraviolet lasers. *J. Raman Spectrosc.* **1975,** *3*, 55-64.

29. Hirakawa, A. Y.; Tsuboi, M., Molecular geometry in an excited electronic state and a preresonance Raman effect. *Science* **1975,** *188*, 359-361.

30. Ziegler, L. D.; Albrecht, A. C., Ultraviolet preresonance Raman scattering of benzene derivatives. I. Excitation profiles for fundamentals. *J. Chem. Phys.* **1979,** *70*, 2634-2643.

31. Balakrishnan, G.; Hu, Y.; Nielsen, S. N.; Spiro, T. G., Tunable kHz deep ultraviolet (193-210 nm) Laser for Raman applications. *Appl. Spectrosc.* **2005,** *59*, 776-781.

32. Bykov, S.; Lednev, I. K.; Ianoul, A.; Mikhonin, A. V.; Munro, C.; Asher, S. A., Steady-state and transient ultraviolet resonance Raman spectrometer for the 193-270 nm spectral region. *Appl. Spectrosc.* **2005,** *59*, 1541-1552.

33. Lednev, I. K.; Ermolenkov, V. V.; He, W.; Xu, M., Deep-UV Raman spectrometer tunable between 193 and 205 nm for structural characterization of proteins. *Anal. Bioanal. Chem.* **2005,** *381*, 431-437.

34. Kim, J.; Pan, D.; Mathies, R. A., Picosecond dynamics of G-protein coupled receptor activation in rhodopsin from time-resolved UV resonance Raman spectroscopy. *Biochemistry* **2003,** *42*, 5169-5175.

35. Zhao, X.; Chen, R.; Tengroth, C.; Spiro, T. G., Solid-state tunable kHz ultraviolet laser for Raman applications. *Appl. Spectrosc.* **1999,** *53*, 1200-1205.

36. Kaminaka, S.; Mathies, R. A., High-throughput large-aperture prism prefilter for ultraviolet resonance Raman spectroscopy. *Appl. Spect.* **1998,** *52* (3), 469-473.

37. Hashimoto, S.; Ikeda, T.; Takeuchi, H.; Harada, I., Utilization of a prism monochromator as a sharp-cut band-pass filter in ultraviolet Raman spectroscopy. *Appl. Spectrosc.* **1993,** *47*, 1283-1285.

38. Russell, M. P.; Vohnik, S.; Thomas Jr., G. J., Design and performance of an ultraviolet resonance Raman spectrometer for proteins and nucleic acids. *Biophys. J.* **1995,** *68*, 1607-1612.

39. Kaminaka, S.; Kitagawa, T., A novel idea for practical UV resonance Raman measurement with a double monochromator and its application to protein structural studies. *Appl. Spectrosc.* **1992,** *46*, 1804-1808.

40. Trulson, M. O.; Lueck, H. B.; Friedrich, D. M., Performance of a spatial-filter-equipped single monochromator for Raman spectroscopy. *Appl. Spectrosc.* **1994,** *48*, 720-723.

41. McFarland, J. T., Flavins. In *Biological Applications of Raman Spectroscopy: Volume 2*, Spiro, T. G., Ed. John Wiley and Sons, Inc.: New York, 1987; Vol. 2, pp 211-302.

42. McCamant, D. W.; Kukura, P.; Mathies, R. A., Femtosecond broadband stimulated Raman: A new approach for high-performance vibrational spectroscopy. *Appl. Spectrosc.* **2003,** *57*, 1317-1323.

43. Cherepy, N. J.; Shreve, A. P.; Moore, L. J.; Boxer, S. G.; Mathies, R. A., Temperature dependence of the Q(y) resonance Raman spectra of bacteriochlorophylls, the primary electron donor, and bacteriopheophytins in the bacterial photosynthetic reaction center. *Biochemistry* **1997,** *36*, 8559-8566.

44. Matousek, P.; Towrie, M.; Stanley, A.; Parker, A. W., Efficient rejection of fluorescence from Raman spectra using picosecond Kerr gating. *Appl. Spectrosc.* **1999,** *53*, 1485-1489.

45. Efremov, E. V.; Buijs, J. B.; Gooijer, C.; Ariese, F., Fluorescence rejection in resonance Raman spectroscopy using a picosecond-gated intensified charge-coupled device camera. *Appl. Spectrosc.* **2007,** *61*, 571-578.

46. Shreve, A. P.; Cherepy, N. J.; Mathies, R. A., Effective rejection of fluorescence interference in Raman spectroscopy using a shifted excitation difference technique. *Appl. Spectrosc.* **1992,** *46*, 707-711.

47. Fang, C.; Frontiera, R. R.; Tran, R.; Mathies, R. A., Mapping GFP structure evolution during proton transfer with femtosecond Raman spectroscopy. *Nature* **2009,** *462*, 200-205.

48. Ernst, O. P.; Lodowski, D. T.; Elstner, M.; Hegemann, P.; Brown, L. S.; Kandori, H., Microbial and animal rhodopsins: Structures, functions, and molecular mechanisms. *Chem. Rev.* **2014,** *114*, 126-163.

49. Palczewski, K.; Kumasaka, T.; Hori, T.; Behnke, C. A.; Motoshima, H.; Fox, B. A.; Trong, I. S.; Teller, D. C.; Okada, T.; Stenkamp, R. E.; Yamamoto, M.; Miyano, M., Crystal structure of rhodopsin: A G protein-coupled receptor. *Science* **2000,** *289*, 739-745.

50. Wald, G., Molecular basis of visual excitation. *Science* **1968,** *162* (230-239).

51. Lewis, A.; Fager, R. S.; Abrahamson, E. W., Tunable laser resonance Raman spectroscopy of the visual process. *J. Raman Spectrosc.* **1973,** *1*, 465-470.

52. Oseroff, A. R.; Callender, R. H., Resonance Raman spectroscopy of rhodopsin in retinal disk membranes. *Biochemistry* **1974,** *13*, 4243-4248.

53. Peters, K.; Applebury, M. L.; Rentzepis, P. M., Primary photochemical event in vision: Proton translocation. *Proc. Natl. Acad. Sci. U. S. A.* **1977,** *74*, 3119-3123.

54. Fransen, M. R.; Luyten, W. C. M. M.; van Thuijl, J.; Lugtenburg, J.; Jansen, P. A. A.; van Breugel, P. J. G. M.; Daemen, F. J. M., Structure of the chromophoric group in bathorhodopsin. *Nature* **1976,** *260*, 726-727.

55. Eyring, G.; Curry, B.; Mathies, R. A.; Fransen, R.; Palings, I.; Lugtenburg, J., Interpretation of the resonance Raman spectrum of bathrhodopsin based on visual pigment analogs. *Biochemistry* **1980,** *19*, 2410-2418.

56. Palings, I.; Van den Berg, E. M. M.; Lugtenburg, J.; Mathies, R. A., Complete assignment of the hydrogen-out-of-plan wagging vibrations of bathrhodopsin: Chromophore structure and energy storage in the primary photoproduct of vision. *Biochemistry* **1989,** *28*, 1498-1507.

57. Yan, E. C. Y.; Ganim, Z.; Kazmi, M. A.; Chang, B. S. W.; Sakmar, T. P.; Mathies, R. A., Resonance Raman analysis of the mechanism of energy storage and chromophore distortion in the primary visual photoproduct. *Biochemistry* **2004,** *43*, 10867-10876.

58. Kim, J. E.; McCamant, D. W.; Zhu, L.; Mathies, R. A., Resonance Raman structural evidence that the cis-to-trans isomerization in rhodopsin occurs in femtoseconds. *J. Phys. Chem. B* **2001,** *105* (1240-1249).

59. Pan, D.; Ganim, Z.; Kim, J. E.; Verhoeven, M. A.; Lugtenburg, J.; Mathies, R. A., Time-resolved resonance Raman analysis of chromophore structural changes in the formation and decay of rhodopsin's BSI intermediate. *J. Am. Chem. Soc.* **2002,** *124*, 4857-4864.

60. Pan, D.; Mathies, R. A., Chromophore structure in lumirhodopsin and metarhodopsin I by time-resolved resonance Raman microchip spectroscopy. *Biochemistry* **2001,** *40*, 7929-7936.

61. Kukura, P.; McCamant, D. W.; Yoon, S.; Wandschneider, D. B.; Mathies, R. A., Structural observation of the primary isomerization in vision with femtosecond-stimulated Raman. *Science* **2005,** *310*, 1006-1009.

62. Schoenlein, R. W.; Peteanu, L. A.; Mathies, R. A.; Shank, C. V., The first step in vision: Femtosecond isomerization of rhodopsin. *Science* **1991,** *254*.

63. McCamant, D. W., Re-evaluation of rhodopsin's relaxation kinetics determined from femtosecond stimulated Raman lineshapes. *J. Phys. Chem. B* **2011,** *115*, 9299-9305.

64. Kim, J. E.; Mathies, R. A., Anti-Stokes Raman study of vibrational cooling dynamics in the primary photochemistry of rhodopsin. *J. Phys. Chem. A* **2002,** *106*, 8508-8515.

65. Harada, I.; Takeuchi, H., Raman and Ultraviolet Resonance Raman Spectra of Proteins and Related Compounds. In *Spectroscopy of Biological Systems*, Clark, R. J. H.; Hester, R. E., Eds. John Wiley & Sons, Ltd.: Chichester, U.K., 1986; Vol. 13.

66. Austin, J. C.; Jordan, T.; Spiro, T. G., Ultraviolet Resonance Raman Studies of Proteins and Related Model Compounds. In *Biomolecular Spectroscopy, Part A*, Clark, R. J. H.; Hester, R. E., Eds. John Wiley and Sons: New York, 1993; pp 55-127.

67. Cantor, C. R.; Schimmel, P. R., *Biophysical Chemistry*. W. H. Freeman and Company: New York, 1980.

68. Wang, Y.; Purrello, R.; Jordan, T.; Spiro, T. G., UVRR spectroscopy of the peptide bond. 1. Amide S, a nonhelical structure marker, is a CaH bending mode. *J. Am. Chem. Soc.* **1991,** *113*, 6359-6368.

69. Jordan, T.; Mukerji, I.; Wang, Y.; Spiro, T. G., UV resonance Raman spectroscopy and hydrogen bonding of the proline peptide bond. *J. Mol. Struct.* **1996,** *379*, 51-64.

70. Huang, C.-Y.; Balakrishnan, G.; Spiro, T. G., Protein secondary structure from deep-UV sesonance Raman spectroscopy. *J. Raman Spectrosc.* **2006,** *37*, 277-282.

71. Chi, Z.; Chen, X. G.; Holtz, J. S. W.; Asher, S. A., UV resonance Raman-selective amide vibrational enhancement: quantitative methodology for determining protein secondary structure. *Biochemistry* **1998,** *36*, 2854-2864.

72. Ozdemir, A.; Lednev, I. K.; Asher, S. A., Comparison between UV Raman and circular dichroism detection of short α-helices in bombolitin III. *Biochemistry* **2002,** *41*, 1893-1896.

73. Sreerama, N.; Woody, R. W., *Circular Dichroism of Peptides and Proteins*. Wiley and Sons: New Jersey, 2000.

74. Woody, R. W., *Theory of Circular Dichroism of Proteins*. Plenum Press: New York, 1996.

75. Chin, D. H.; Woody, R. W.; Rohl, C. A.; Baldwin, R. L., Circular dichroism spectra of short, fixed-nucleus alanine helices. *Proc. Natl. Acad. Sci. U. S. A.* **2002,** *99*, 15416-15421.

76. Wallace, B. A.; Lees, J. G.; Orry, A. J. W.; Lobley, A.; Janes, R. W., Analyses of circular dichroism spectra of membrane proteins. *Protein Sci.* **2003,** *12*, 875-884.

77. Fodor, S. P. A.; Copeland, R. A.; Grygon, C. A.; Spiro, T. G., Deep-ultraviolet Raman excitation profiles and vibronic scattering mechanisms of pheylalanine, tyrosine, and tryptophan. *J. Am. Chem. Soc.* **1989,** *111* (15), 5509-5518.

78. Sweeney, J. A.; Asher, S. A., Tryptophan UV resonance Raman excitation profiles. *J. Phys. Chem.* **1990,** *94*, 4784-4791.

79. Chi, Z.; Asher, S. A., UV Raman determination of the environment and solvent exposure of tyr and trp residues. *J. Phys. Chem. B* **1998,** *102*, 9595-9602.

80. Efremov, R. G.; Feofanov, A. V.; Nabiev, I. R., Effect of hydrophobic environment on the resonance Raman spectra of tryptophan residues in proteins. *J. Raman Spectrosc.* **1992,** *23*, 69-73.

81. Schlamadinger, D. E.; Gable, J. E.; Kim, J. E., Hydrogen-bonding and solvent polarity markers in the UV resonance Raman spectrum of tryptophan: Application to membrane proteins. *J. Phys. Chem. B* **2009,** *113*, 14769-14778.

82. Hildebrandt, P. G.; Copeland, R. A.; Spiro, T. G.; Otlewski, J.; Laskowski, M.; Prendergast, F. G., Tyrosine hydrogen-bonding and environmental effects in

proteins probed by ultraviolet resonance Raman spectroscopy. *Biochemistry* **1988,** *27*, 5426-5433.

83. Ludwig, B.; Asher, S. A., Ultraviolet resonance Raman excitation profiles of tyrosine: Dependence of Raman cross sections on excited-state intermediates. *J. Am. Chem. Soc.* **1988,** *110*, 1005-1011.

84. Asher, S. A.; Murtaugh, J. L., UV Raman excitation profiles of imidazole, imidazolium, and water. *Appl. Spectrosc.* **1988,** *42*, 83-90.

85. Takeuchi, H., Raman structural markers of tryptophan and histidine side chains in proteins. *Biopolymers* **2003,** *72*, 305-317.

86. Schlamadinger, D. E.; Leigh, B. S.; Kim, J. E., UV Resonance Raman study of TrpZip2 and related peptides: π-π interactions of tryptophan. *J. Raman Spectrosc.* **2012,** *43*, 1459-1464.

87. Caswell, D. S.; Spiro, T. G., Ultraviolet resonance Raman spectroscopy of imidazole, histidine, and Cu(imidazole)v2+: Implications for protein studies. *J. Am. Chem. Soc.* **1986,** *108*, 6470-6477.

88. Miura, T.; Takeuchi, H.; Harada, I., Characterization of individual tryptophan side chains in proteins using Raman spectroscopy and hydrogen-deuterium exchange kinetics. *Biochemistry* **1988,** *27*, 88-94.

89. Miura, T.; Takeuchi, H.; Harada, I., Tryptophan Raman bands sensitive to hydrogen bonding and side-chain conformation. *J. Raman Spectrosc.* **1989,** *20*, 667-671.

90. Harada, I.; Miura, T.; Takeuchi, H., Origin of the doublet at 1360 and 1340 cm-1 in the Raman spectra of tryptophan and related compounds. *Spectrochim. Acta* **1986,** *42A*, 307-312.

91. Takeuchi, H.; Watanabe, Y.; Satoh, Y.; Harada, I., Effects of hydrogen bonding on the tyrosine Raman bands in the 1300-1150 cm-1 region. *J. Raman Spectrosc.* **1989,** *20*, 233-237.

92. Strickland, E. H.; Beychok, S., Aromatic contributions to circular dichroism spectra of proteins. *Crit. Rev. Biochem.* **1974,** *2*, 113-175.

93. Nagai, M.; Nagatomo, S.; Nagai, Y.; Ohkubo, K.; Imai, K.; Kitagawa, T., Near-UV circular dichroism and UV resonance Raman spectra of individual tryptophan residues in human hemoglobin and their changes upon the quaternary structure transition. *Biochemistry* **2012,** *51*, 5932-5941.

94. Nagatomo, S.; Nagai, M.; Ogura, T.; Kitagawa, T., Near-UV circular dichroism and UV resonance Raman spectra of tryptophan residues as a structural marker of proteins. *J. Phys. Chem. B* **2013,** *117*, 9343-9353.

95. The Universal Protein Resource (UniProt). *Nucleic Acids Res.* **2007,** *36*, D190-195.

96. White, S. H.; Ladokhin, A. S.; Jayasinghe, S.; Hristova, K., How membranes shape protein structure. *J. Biol. Chem.* **2001,** *276*, 32395-32398.

97. Gallivan, J. P.; Dougherty, D. A., Cation-π interactions in structural biology. *Proc. Natl. Acad. Sci. U. S. A.* **1999,** *96*, 9459-9464.

98. Millefiori, S.; Alparone, A.; Millefiori, A.; Vanella, A., Electronic and vibrational polarizabilities of the twenty naturally occurring amino acids. *Biophys. Chem.* **2008,** *132*, 139-147.

99. Wimley, W. C.; White, S. H., Experimentally determined hydrophobicity scale for proteins at membrane interfaces. *Nat. Struct. Biol.* **1996,** *3*, 842-848.

100. Killian, J. A.; von Heijne, G., How proteins adapt to a membrane-water interface. *Trends Biochem. Sci.* **2000**.

101. White, S. H.; Wimley, W. C., Membrane protein folding and stability: Physical principles. *Annu. Rev. Biophys. Biomol. Struct.* **1999,** *28*, 319-365.

102. Sanchez, K. M.; Gable, J. E.; Schlamadinger, D. E.; Kim, J. E., Effects of tryptophan microenvironment, soluble domain, and vesicle size on the thermodynamics of membrane protein folding: Lessons from the transmembrane protein OmpA. *Biochemistry* **2008,** *47*, 12844-12852.

103. Hong, H.; Park, S.; Flores Jimenez, R. H.; Rinehart, D.; Tamm, L. K., Role of aromatic side chains in the folding and thermodynamic stability of integral membrane proteins. *J. Am. Chem. Soc.* **2007,** *129*, 8320-8327.

104. Blondelle, S. E.; Houghten, R. A., Probing the relationships between the structure and hemolytic activity of melittin with a complete set of leucine substitution analogs. *Peptide Res.* **1991,** *4*, 12-18.

105. Andreu, D.; Merrifield, R. B.; Steiner, H.; Boman, H. G., N-terminal analogues of cecropin A: Synthesis, antibacterial activity, and conformational properties. *Biochemistry* **1985,** *24*, 1683-1688.

106. El-Mashtoly, S. F.; Takahashi, H.; Shimizu, T.; Kitagawa, T., Ultraviolet resonance Raman evidence for utilization of the heme 6-propionate hydrogen-bond network in signal transmission from heme to protein in *Ec* DOS protein. *J. Am. Chem. Soc.* **2007,** *129*, 3556-3563.

107. Miura, T.; Takeuchi, H.; Harada, I., Raman spectroscopic characterization of tryptophan side chains in lysozyme bound to inhibitors: Role of the hydrophobic box in the enzymatic function. *Biochemistry* **1991,** *30*, 6074-6080.

108. Xue, Y.; Davis, A. V.; Balakrishnan, G.; Stasser, J. P.; Staehlin, B. M.; Focia, P.; Spiro, T. G.; Penner-Hahn, J. E.; O'Halloran, T. V., Cu(I) recognition via cation-π and methionine interactions in CusF. *Nat. Chem. Biol.* **2008,** *4*, 107-109.

109. Di Lella, S.; Ma, L.; Díaz Ricci, J. C.; Rabinovich, G. A.; Asher, S. A.; Álvarez, R. M. S., Critical role of the solvent environment in galectin-1 binding to the disaccharide lactose. *Biochemistry* **2009,** *48*, 786-791.

110. Wen, Z. Q.; Thomas Jr., G. J., Ultraviolet-resonance Raman spectroscopy of the filamentous virus Pf3: Interactions of Trp38 specific to the assembled virion subunit. *Biochemistry* **2000,** *39*, 146-152.

111. Takeuchi, H., UV Raman markers for structural analysis of aromatic side chains in proteins. *Anal. Sci.* **2011,** *27*, 1077-1086.

112. Fujimaki, N.; Kitamura, F.; Takeuchi, H., Pro-oxidant copper-binding mode of the apo form of ALS-linked SOD1 mutant H43R denatured at physiological temperature. *Biochemistry* **2013,** *52*, 5184-5194.

113. Hiramatsu, H.; Takeuchi, K.; Takeuchi, H., Involvement of histidine residues in the pH-dependent b-galactoside binding activity of human galectin-1. *Biochemistry* **2013,** *52*, 2371-2380.

114. Wang, D.; Zhao, X. J.; Vargek, M.; Spiro, T. G., Metal-bound histidine modes in UV resonance Raman spectra of Cu, Zn superoxide dismutase. *J. Am. Chem. Soc.* **2000,** *122*, 2193-2199.

115. Arzhantsev, S.; Vilker, V.; Kauffman, J., Deep-ultraviolet (UV) resonance Raman spectroscopy as a tool for quality control of formulated therapeutic proteins. *Appl. Spectrosc.* **2012,** *66*, 1262-1268.

116. Ashton, L.; Xu, Y. H.; Brewster, V. L.; Cowcher, D. P.; Sellick, C. A.; Dickson, A. J.; Stephens, G. M.; Goodacre, R., The challenge of applying Raman spectroscopy to monitor recombinant antibody production. *Analyst* **2013,** *138*, 6977-6985.

117. Couling, V. W.; Fischer, P.; Klenerman, D.; Huber, W., Ultraviolet resonance Raman study of drug binding in dihydrofolate reducase, gyrase, and catechol o-methyltransferase. *Biophys. J.* **1998,** *75*, 1097-1106.

118. Hashimoto, S.; Yabusaki, T.; Takeuchi, H.; Harada, I., Structure and ligand-binding modes of human serum albumin studied by UV resonance Raman spectroscopy. *Biospectroscopy* **1995,** *1*, 375-385.

119. Huang, C.-Y.; Balakrishnan, G.; Spiro, T. G., Early events in apomyoglobin unfolding probed by laser T-jump/UV resonance Raman spectroscopy. *Biochemistry* **2005,** *44*, 15734-15742.

120. Balakrishnan, G.; Case, M. A.; Pevsner, A.; Zhao, X. J.; Tengroth, C.; McLendon, G. L.; Spiro, T. G., Time-resolved absorption and UV resonance Raman spectra reveal stepwise formation of T quaternary contacts in the allosteric pathway of hemoglobin. *Journal of Molecular Biology* **2004,** *340* (4), 843-856.

121. Mizuno, M.; Hamada, N.; Tokunaga, F.; Mizutani, Y., Picosecond protein response to the chromophore isomerization of photoactive yellow protein: Selective observation of tyrosine and tryptophan residues by time-resolved ultraviolet resonance Raman spectroscopy. *J. Phys. Chem. B* **2007,** *111*, 6293-6296.

122. Sato, A.; Gao, Y.; Kitagawa, T.; Mizutani, Y., Primary protein response after ligand photodissociation in carbonmonoxy myoglobin. *Proc. Natl. Acad. Sci. U. S. A.* **2007,** *104*, 9627-9632.

123. Rodriguez-Mendieta, I. R.; Spence, G. R.; Gell, C.; Radford, S. E.; Smith, D. A., Ultraviolet resonance Raman studies reveal the environment of tryptophan and tyrosine residues in the native and partially unfolded states of the E colicin-binding immunity protein Im7. *Biochemistry* **2005,** *44*, 3306-3315.

124. Chi, Z.; Asher, S. A., Ultraviolet resonance Raman examination of horse apomyoglobin acid unfolding intermediates. *Biochemistry* **1999,** *38*, 8196-8203.

125. Weeks, C. L.; Polishchuk, A.; Getahun, Z.; DeGrado, W. F.; Spiro, T. G., Investigation of an unnatural amino acid for use as a resonance Raman probe: Detection limits and solvent and temperature dependence of the nC≡N band of 4-cyanophenylalanine. *J. Raman Spectrosc.* **2008,** *39*, 1606-1613.

126. Copeland, R. A.; Spiro, T. G., Ultraviolet resonance Raman spectroscopy of flavin mononucleotide and flavin adenine dinucleotide. *J. Phys. Chem.* **1986,** *90*, 6648-6654.

127. Ames, J. B.; Bolton, S. R.; Netto, M. M.; Mathies, R. A., Ultraviolet resonance Raman spectroscopy of bacteriorhodopsin: Evidence against tyrosinate in the photocycle. *J. Am. Chem. Soc.* **1990,** *112*, 9007-9009.

128. Harada, I.; Yamagishi, K.; Uchida, K.; Takeuchi, H., Ultraviolet resonance Raman spectra of bacteriorhodopsin in the light-adapted and dark-adapted states. *J. Am. Chem. Soc.* **1990,** *112*, 2443-2445.

129. Ames, J. B.; Ros, M.; Raap, J.; Lugtenburg, J.; Mathies, R. A., Time-resolved ultraviolet resonance Raman studies of protein structure: Application to bacteriorhodopsin. *Biochemistry* **1992,** *31*, 5328-5334.

130. Hashimoto, S.; Sasaki, M.; Takeuchi, H.; Needleman, R.; Lanyi, J. K., Changes in hydrogen bonding and environment of tryptophan residues on helix F in bacteriorhodopsin during the photocycle: a time-resolved ultraviolet resonance Raman study. *Biochemistry* **2002,** *41*, 6495-6503.

131. Asakawa, K.; Masuda, S.; Takeuchi, H., Indole ring orientations of Trp189 in the ground and M intermediate of bacteriorhodopsin as studied by polarized UV resonance Raman spectroscopy. *J. Raman Spectrosc.* **2006,** *37*, 255-262.

132. Hashimoto, S.; Obata, K.; Takeuchi, H.; Needleman, R.; Lanyi, J. K., Ultraviolet resonance Raman spectra of Trp-182 and Trp-189 in bacteriorhodopsin: novel information on the structure of Trp-182 and its steric interaction with retinal. *biochemistry* **1997,** *36*, 11583-11590.

133. Kaminaka, S.; Mathies, R. A., Time-resolved ultraviolet resonance Raman of protein structural changes in the KL-intermediate of bacteriorhodopsin. *Laser Chem.* **1999,** *19*, 165-168.

134. Mizuno, M.; Shibata, M.; Yamada, J.; Kandori, H.; Mizutani, Y., Picosecond time-resolved ultraviolet resonance Raman spectroscopy of bacteriorhodopsin: Primary protein response to the photoisomerization of retinal. *J. Phys. Chem. B* **2009,** *113*, 12121-12128.

135. Hashimoto, S.; Sasaki, M.; Takeuchi, H., Ultraviolet resonance Raman evidence for the opening of a water-permeable channel in the M to N transition of bacteriorhodopsin. *J. Am. Chem. Soc.* **1998,** *120*, 443-444.

136. Kochendoerfer, G. G.; Kaminaka, S.; Mathies, R. A., Ultraviolet resonance Raman examination of the light-induced protein structural changes in rhodopsin activation. *Biochemistry* **1997,** *36* (43), 13153-13159.

137. Hashimoto, S.; Takeuchi, H.; Nakagawa, M.; Tsuda, M., Ultraviolet resonance Raman evidence for the absence of tyrosinate in octopus rhodopsin and the participation of Trp residues in the transition to acid metarhodopsin. *FEBS Lett.* **1996,** *398*, 239-242.

138. Chen, J.; Barry, B. A., Ultraviolet resonance Raman microprobe spectroscopy of photosystem II. *Photochem. Photobiol.* **2008,** *84*, 815-818.

139. Aki, M.; Ogura, T.; Shinzawa-Itoh, K.; Yoshikawa, S.; Kitagawa, T., A new measurement system for UV resonance Raman spectra of large proteins and its application to cytochrome *c* oxidase. *J. Phys. Chem. B* **2000,** *104*, 10765-10774.

140. Halsey, C. M.; Oshokoya, O. O.; Jiji, R. D.; Cooley, J. W., Deep-UV resonance Raman analysis of the *Rhodobacter capsulatus* cytochrome bc_1 complex reveals a potential marker for the transmembrane peptide backbone. *Biochemistry* **2011,** *50*, 6531-6538.

141. Sanchez, K. M.; Kang, G.; Wu, B.; Kim, J. E., Tryptophan-lipid interactions in membrane protein folding probed by UV resonance Raman and fluorescence spectroscopy. *Biophys. J.* **2011,** *100*, 2121-2130.

142. Sanchez, K. M.; Neary, T. J.; Kim, J. E., UV resonance Raman spectroscopy of folded and unfolded states of an integral membrane protein. *J. Phys. Chem. B* **2008,** *112*, 9507-9511.

143. Oladepo, S. A.; Xiong, K.; Hong, Z.; Asher, S. A., Elucidating peptide and protein structure and dynamics: UV resonance Raman spectroscopy. *J. Phys. Chem. Lett.* **2011,** *2*, 334-344.

144. Shafaat, H. S.; Sanchez, K. M.; Neary, T. J.; Kim, J. E., Ultraviolet resonance Raman spectroscopy of a β-sheet peptide: A model for membrane protein folding. *J. Raman Spectrosc.* **2009,** *40*, 1060-1064.

145. Wimley, W. C.; Hristova, K.; Ladokhin, A. S.; Silvestro, L.; Axelson, P. H.; White, S. H., Folding of β-sheet membrane proteins: A hydrophobic hexapeptide model. *J. Mol. Biol.* **1998,** *277*, 1091-1110.

146. Halsey, C. M.; Xiong, J.; Oshokoya, O. O.; Johnson, J. A.; Shinde, S.; Beatty, J. T.; Ghirlanda, G.; JiJi, R. D.; Cooley, J. W., Simultaneous observation of peptide backbone lipid polvation and α-helical ptructure by deep-UV resonance Raman spectroscopy. *ChemBioChem* **2011,** *12*, 2125-2128.

147. Brown, M. C.; Yakubu, R. A.; Taylor, J.; Halsey, C. M.; Xiong, J.; Jiji, R. D.; Cooley, J. W., Bilayer surface association of the pHLIP peptide promotes extensive backbone desolvation and helically-constrained structures. *Biophys. Chem.* **2014,** *187-188*, 1-6.

148. Brogden, K. A., Antimicrobial peptides: Pore formers or metabolic inhibitors in bacteria? *Nat. Rev. Microbiol.* **2005,** *3*, 238-250.

149. Zasloff, M., Antimicrobial peptides of multicellular organisms. *Nature* **2002,** *415*, 389-395.

150. Epand, R. M.; Vogel, H. J., Diversity of antimicrobial peptides and their mechanism of action. *Biochim. Biophys. Acta, Biomembr.* **1999,** *1462*, 11-28.

151. Blondelle, S. E.; Houghten, R. A., Hemolytic and antimicrobial activities of the twenty-four individual omission analogs of melittin. *Biochemistry* **1991,** *30* (19), 4671-4678.

152. Wei, G.; Pazgier, M.; De Leeuw, E.; Rajabi, M.; Li, J.; Zou, G.; Jung, G.; Yuan, W.; Lu, W.-Y.; Lehrer, R. I.; Lu, W., Trp-26 imparts functional versatility to human α-defensin HNP1. *J. Biol. Chem.* **2010,** *285* (16275-16285).

153. Andreu, D.; Merrifield, R. B.; Steiner, H.; Boman, H. G., N-terminal analogues of cecropin A: Synthesis, antibacterial activity, and conformational properties. *Biochemistry* **1985**, 24, 1683-1688.

154. Gable, J. E.; Schlamadinger, D. E.; Cogen, A. L.; Gallo, R. L.; Kim, J. E., Fluorescence and UV resonance Raman study of peptide-vesicle interactions of human cathelicidin LL-37 and its F6W and F17W mutants. *Biochemistry* **2009,** *48*, 11264-11272.

155. Turner, J.; Cho, Y.; Dinh, N.-N.; Waring, A. J.; Lehrer, R. I., Activities of LL-37, a cathelin-associated antimicrobial peptide of human neutrophils. *Antimicrob. Agents Chemother*. **1998,** *42*, 2206-2214.

156. Dürr, U. H. N.; Sudheendra, U. S.; Ramamoorthy, A., LL-37, the only human member of the cathelicidin family of antimicrobial peptides. *Biochim. Biophys. Acta, Biomembr*. **2006,** *1758*, 1408-1425.

157. Quan, B.; Ianoul, A., UV resonance Raman spectroscopy probes the localization of tryptophan-containing antimicrobial peptides in lipid vesicles. *J. Raman Spectrosc.* **2009,** *40*, 260-263.

158. Strøm, M. B.; Rekdal, Ø.; Svendsen, J. S., Antibacterial activity of 15-residue lactoferricin derivatives. *J. Pept. Res.* **2000,** *56*, 265-274.

159. Santamaría, C.; Larios, S.; Quirós, S.; Pizarro-Cerda, J.; Gorvel, J.; Lomonte, B.; Moreno, E., Bactericidal and antiendotoxic properties of short cationic peptides derived from a snake venom lys49 phospholipase A_2. *Antimicrob. Agents Chemother*. **2005,** *49*, 1340-1345.

160. Pripotnev, S.; Won, A.; Ianoul, A., The effects of L-to D-isomerization and C-terminus deamidation on the secondary structure of anitmicrobial peptide Anoplin

in aqueous and membrane mimicking environment. *J. Raman Spectrosc.* **2010,** *41*, 1645-1649.

161. Schlamadinger, D. E.; Wang, Y.; McCammon, J. A.; Kim, J. E., Spectroscopic and computational study of melittin, cecropin A, and the hybrid peptide CM15. *J. Phys. Chem. B* **2012,** *116*, 10600-10608.

162. Lührs, T.; Ritter, C.; Adrian, M.; Riek-Loher, D.; Bohrmann, B.; Döbeli, H.; Schubert, D.; Riek, R., 3D structure of Alzheimer's amyloid-β(1-42) fibrils. *Proc. Natl. Acad. Sci. U. S. A.* **2005,** *102*, 17342-17347.

163. Sikirzhytski, V.; Topilina, N. I.; Higashiya, S.; Welch, J. T.; Lednev, I. K., Genetic engineering combined with deep UV resonance Raman spectroscopy for structural characterization of amyloid-like fibrils. *J. Am. Chem. Soc.* **2008,** *130*, 5852-5853.

164. Pawar, A. P.; DuBay, K. F.; Zurdo, J.; Chiti, F.; Vendruscolo, M.; Dobson, C. M., Prediction of "aggregation-prone" and "aggregation-susceptible" regions in proteins associated with neurodegenerative diseases. *J. Mol. Biol.* **2005,** *350*, 379-392.

165. Popova, L. A.; Kodali, R.; Wetzel, R.; Lednev, I. K., Structural variations in the cross-β core of amyloid β fibrils revealed by deep UV resonance Raman spectroscopy. *J. Am. Chem. Soc.* **2010,** *132*, 6324-6328.

166. Wang, M.; JiJi, R. D., Resolution of localized small molecule-Aβ interactions by deep-ultraviolet resonance Raman spectroscopy. *Biophys. Chem.* **2011,** *158*, 96-103.

167. Cheng, H.; Xia, B.; Reed, G. H.; Markley, J. L., Optical, EPR, and H-1 NMR spectroscopy of serine-ligated [2Fe-2S] ferredoxins produced by site-directed mutagenesis of cysteine residues in recombinant *anabaena* 7120 vegetative ferredoxin. *Biochemistry* **1994,** *33*, 3155-3164.

168. Oelze, J., Analysis of Bacteriochlorophylls. *Methods Enzymol.* **1985,** *18*, 257-284.

169. Kobayashi, M.; Akiyama, M.; Kano, H.; Kise, H., Spectroscopy and structure determination. In *Chlorophylls and Bacteriochlorophylls: Biochemistry, Biophysics, Functions and Applications*, Grimm, B.; Porra, R. J.; Rudiger, W.; Scheer, H., Eds. Springer: Dordrecht, The Netherlands, 2006.

6 Conclusion

Tryptophan, although a relatively rare amino acid, is important in enzymatic catalysis[1] and in membrane proteins as an interfacial residue[2]. Indeed, oxidized radical intermediates can play an important role in long-range electron transfer,[3] and the large hydrophobic surface-area and hydrogen bonding-capabilities result in tryptophan making a large contribution to the thermodynamics of insertion and folding of membrane proteins[4]. In this dissertation, the role of the tryptophan triplet state in the oxidation of tryptophan was investigated, and furthermore, the tryptophan triplet decay kinetics were shown to be sensitive to local hydration of the tryptophan residue in unfolded and folded proteins.

The photogeneration of tryptophan radical in apoAzW48 presented in Chapter 3 was unexpected. However, the role of the triplet in the photooxidation reaction is not surprising based on simple kinetic arguments. A long-lived triplet excited state is expected to be readily accessible to electron transfer in the presence of an acceptor if the driving force is sufficient. Certainly, in short-range electron-exchange dye sensitization this is a well-characterized excited state quenching mechanism.[5] However, a more general question arises from these results. Is the observed photooxidation of the triplet a general property of tryptophan, including in other proteins that exhibit long tryptophan phosphorescence lifetimes? Or does the azurin scaffold play a significant role in enabling long-range electron transport through the protein matrix? A systematic study of proteins which exhibit both long triplet lifetimes and contain buried, solvent excluded tryptophan residues, can be used to investigate the general oxidation of tryptophan in proteins. A few candidates based on published results are promising.[6] The method of steady-state

photolysis in the presence of electron acceptor described in this dissertation presents one approach for investigating the photooxidation products. The method developed here allows for simultaneous photolysis and interrogation of sample, and transient products with lifetimes greater than ~0.5 sec can be accessed using a standard UV/Vis spectrometer. We report the generation of relatively unstable neutral radical in apoprotein $\left(\tau_{\text{decay}} = 40\,\text{sec}\right)$ that enabled investigation of the neutral radical formation kinetics. The neutral radical in metalated protein decays on the order of hours,[7] and accordingly, the metal cofactor contributes to the decay dynamics in a significant way. The difference between metalated and apoprotein dynamics can be investigated using molecular dynamics simulations or NMR. It remains to be shown whether the local environment of the radical in apo- and metalated protein differ. This may be accessible to EPR and resonance Raman. The formation kinetics can be revisited with azurin mutants that affect the electron transfer, deprotonation, and decay pathways using the method presented in this dissertation.

The influence of H_2O and D_2O on the triplet decay kinetics of NATA, melittin, and OmpA, has been studied in Chapter 4. These experiments show that the solvent contributes the most to the isotope effect on the triplet decay kinetics of tryptophan, while inherent NH/D exchange makes little to no contribution to the isotope effect. The isotope effect reported here is inverse relative to literature data,[8-10] and the origin of this opposite trend should be the focus of future studies. Despite this unexpected direction for the isotope effect, nonetheless, the decay kinetics can be used to examine the local hydration of unfolded and folded membrane proteins. We report that membrane protein bound by the molecular chaperone Skp lacks an isotope effect. This finding suggests that the unfolded

protein bound by chaperone maybe “pre-desolvated” prior to bilayer insertion, aiding in folding. The results also indicate that the triplet lifetime increases on the same time-scale as protein folding, and thus it may be possible to investigate the extent of solvation during insertion and folding into a bilayer. In addition to experiments on the formation of tertiary, secondary, and contact formation, solvation can be used to illustrate a complete picture of OmpA folding.

In conclusion, this work has extended our understanding of the photochemistry, i.e. triplet electron transfer, and photophysics, i.e. triplet decay kinetics, of tryptophan in biological systems. As described in Chapter 5, spectroscopy of native residues and prosthetic groups can provide a great deal of insight into local structure and dynamics of proteins. These results provide an additional spectroscopic handles in protein structure investigation.

6.1 References

1. Stubbe, J.; van der Donk, W. A., Protein radicals in enzyme catalysis. *Chem. Rev.* **1998,** *98*, 705-762.

2. Killian, J. A.; von Heijne, G., How proteins adapt to a membrane-water interface. *Trends. Biochem. Sci.* **2000,** *25* (9), 429-434.

3. Gray, H. B.; Winkler, J. R., Electron tunneling through proteins. *Q. Rev. Biophys.* **2003,** *36*, 341-372.

4. Wimley, W. C.; White, S. H., Experimentally determined hydrophobicity scale for proteins at membrane interfaces. *Nat. Struct. Biol.* **1996,** *3*, 842-848.

5. Turro, N. J., *Modern molecular photochemistry*. University Science Books: California, 1992.

6. Vanderkooi, J. M.; Calhoun, D. B.; Englander, S. W., On the prevalence of room-temperature protein phosphorescence. *Science* **1987,** *236*, 568-569.

7. Larson, B. C.; Pomponio, J. R.; Shafaat, H. S.; Kim, R. H.; Leigh, B. S.; Tauber, M. J.; Kim, J. E., Photogeneration and quenching of tryptophan radical in azurin. *J. Phys. Chem. B* **2015,** *119*, 9438-9449.

8. Robinson, G. W.; Frosch, R. P., Electronic excitation transfer and relaxation. *J. Chem. Phys.* **1963,** *38* (5), 1187-1203.

9. Fischer, C. J.; Schauerte, J. A.; Wisser, K. C.; Gafni, A.; Steel, D. G., Hydrogen exchange at the core of *Escherichia coli* alkaline phosphatase studied by room-temperature tryptophan phosphorescence. *Biochemistry* **2000,** *39* (6), 1455-1461.

10. Fischer, C. J.; Gafni, A.; Steel, D. G.; Schauerte, J. A., The triplet-state lifetime of indole in aqueous and viscous environments: Significance to the interpretation of room temperature phosphorescence in proteins. *J. Am. Chem. Soc.* **2002,** *124*, 10359-10366.

Appendix

A.1 Igor Pro procedures for modeling tryptophan photooxidation

```
Function TrpET_T(pw,tt,yw,dydt)
        Wave pw
        Variable tt
        Wave yw
        Wave dydt

// photooxidation scheme from the triplet state
//   k1/k2   k3    k5     k6      k7
// A <==> B* --> T --> C+. --> D. --> E
// ^-------------|
//      k4

//pw[0] k1 excitation rate     //yw[0] A
//pw[1] k2 IC/fluorescence     //yw[1] B*
//pw[2] k3 ISC_ST              //yw[2] T
//pw[3] k4 ISC_TS, phosphoresc //yw[3] C+.
//pw[4] k5 ET                  //yw[4] D.
//pw[5] k6 Deprot              //yw[5] E
//pw[6] k7 Decay

//dA/dt
        dydt[0]=-pw[0]*yw[0] + pw[1]*yw[1] + pw[3]*yw[2]
//dB/dt
        dydt[1]= pw[0]*yw[0] - pw[1]*yw[1] - pw[2]*yw[1]
//dT/dt
        dydt[2]= pw[2]*yw[1] - pw[3]*yw[2] - pw[4]*yw[2]
//dC/dt
        dydt[3]= pw[4]*yw[2] - pw[5]*yw[3] - pw[7]*yw[3]
//dD/dt
        dydt[4]= pw[5]*yw[3] - pw[6]*yw[4]
//dE/dt
        dydt[5]= pw[6]*yw[4]
        return 0
End

// Fitting function for the curve fitting menu
Function FitTrpET_T(pw,yw,xw) : FitFunc
        Wave pw
        Wave yw // data y wave
        Wave xw // x values to be solved
        Make/O/D/N=(numpnts(yw),6) ODEsolution
        ODEsolution=0
        ODEsolution[0][0]=1

        IntegrateODE/M=3/E=1e-9/X=xw TrpET_T, pw, ODEsolution
        yw = ODEsolution[p][4] // offset
End
```

A.2 Skp activity assay

Refolding experiments were performed on OmpA-Skp complexes to determine the activity of Skp chaperone stock. The refolding kinetics of OmpA into dimyristoylphosphatidylcholine (DMPC) vesicles was examined using an electrophoric mobility assay previously described by *Bulieris, P. V. et al.*[1] OmpA-Skp complexes were prepared by dilution of OmpA (8 M Urea) into 20 mM pH 7.3 buffer containing 4×Skp. The residual urea concentration was 0.3-0.8 M. Samples were equilibrated at room temperature for at least 30 minutes before being further diluted with DMPC vesicles. In Figure A2.1, the electrophoric mobility of OmpA are shown for protein refolded from dilute urea, and for samples refolded from a Skp bound complex. The results for the refolding kinetics are shown in Figure A2.2. Folded OmpA migrates to lower molecular weight, as previously described.[2] The kinetics for refolding into neutral vesicles from OmpA-Skp complexes are inhibited compared to refolding directly from dilute urea. This is consistent with previous observations of Skp activity.[1, 3] This assay indicates the Skp protein utilized in these experiments is in a functional form, and capable of binding OmpA within its cavity.

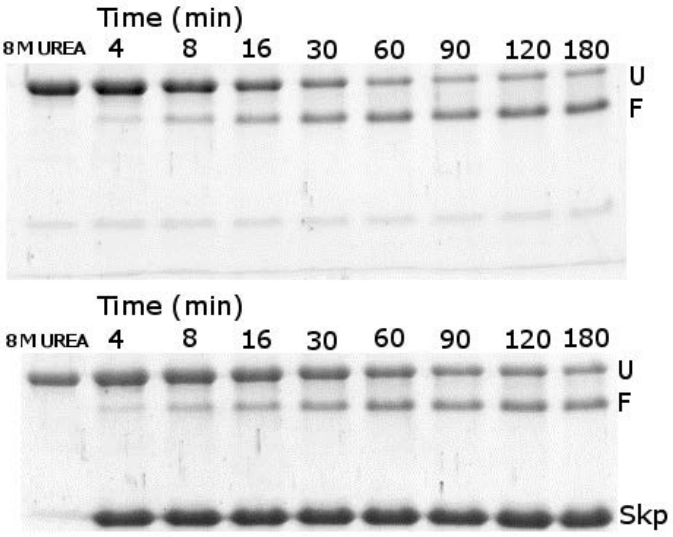

Figure A.2.1 SDS-polyacrylamide gel of OmpA refolding kinetics. Top: refolding into DMPC vesicles from 0.8 M urea. Sample denatured in 8 M urea is shown in lane 1 as a reference. Samples were taken during the folding reaction at 4, 8, 16, 30, 60, 90, 120, and 180 min and shown in lanes 2-9. The unfolded bands (U) migrate to lower molecular weight when folded (F). Bottom: refolding into DMPC vesicles from a complex with the molecular chaperone Skp. The Skp band is indicated for

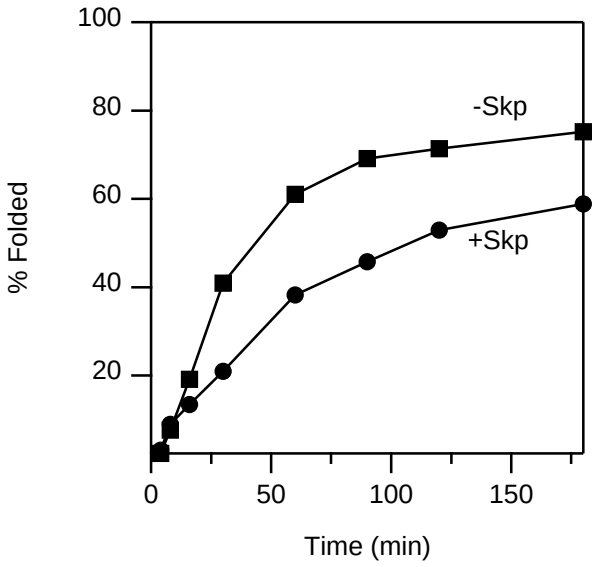

Figure A.2.2 Densiometric analysis of OmpA refolding kinetics. The fraction folded was determined for refolding into DMPC vesicles from a denatured state (-Skp), and from a Skp-bound complex (+Skp).

A.3 Raman spectroscopy of UV excited tryptophan-containing compounds

Visible resonance Raman spectra were acquired of n-acetyl-l-tryptophanamide (NATA, Figure A.3.1) and azurin (Figure A.3.2). In Figure A.3.1, pump-only, probe-only, and pump/probe spectra of NATA are shown. The pump (295 nm) and probe (442 nm) wavelengths were chosen to simultaneously excite and interrogate the sample using the 3rd and 2nd harmonics of a Ti:Sapph laser, respectively. Both beams were overlapped spatially and temporally. The middle panel shows a transient spectrum present in pump/probe experiments after subtraction of the pump-induced background and probe-only spectra. In Figure A.3.2, the resonance Raman spectrum of NATA (middle) was compared to azurin and calculated results for the tryptophan triplet state. The steady-state accumulation of tryptophan triplet in apoazurin (apoAzW48) is expected under constant 280 nm photolysis (see Chapter 3). The 456 nm resonance Raman spectra of apoAzW48 resembles the spectrum of photogenerated tryptophan neutral radical in zinc-substituted azurin (Zn(II)AzW48), in particular the intensity and position of the peaks at ~1560 and ~1590 cm^{-1}. The neutral radical in Zn(II)AzW48 was generated as described by Larson et al.[4] The resonance Raman spectrum of the neutral radical in azurin has been previously described.[5] The peaks in the NATA Raman spectrum (middle) in the aromatic region of the spectrum may be explained by the presence of either an excited state, such as the triplet, or an unknown aromatic photoproduct. The ground state spectra and calculated triplet spectra support this explanation. However, a definite assignment of the spectrum is challenging due to excited state photochemistry, i.e. photoionization, as shown to be the case in apoazurin (See Chapter 3).

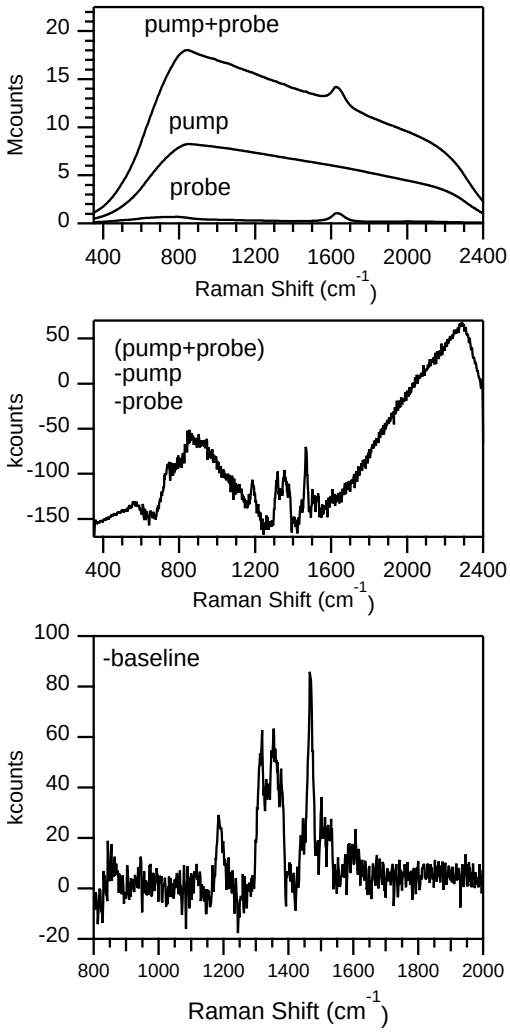

Figure A.3.1 Raman spectrum of UV excited 300 μM N-acetyl-l-tryptophanamide (NATA), 3 M KI, 3 mM Na_2SO_3. Using a Ti:Sapph laser with a fundamental ~884 nm (1 kHz, ~100 ns) the sample was excited using the third harmonic (295 nm, pump) and interrogated with the second harmonic (442 nm, probe). The pump (power = 3 mW) and probe (power = 5 mW) beams were overlapped approximately 30% onto the face of fused silicia capillary (250 μm i.d.). The sample was flowed continuously at a rate of 40 μm/msec through the capillary from a nitrogen pressurized reservoir. The scattering was collected in a 135-degree backscattering geometry. Top: the probe- or pump-only spectra each represent an accumulation of 60 minutes. The pump and probe spectrum was accumulated for 120 minutes. Middle: subtraction of probe- and pump-only

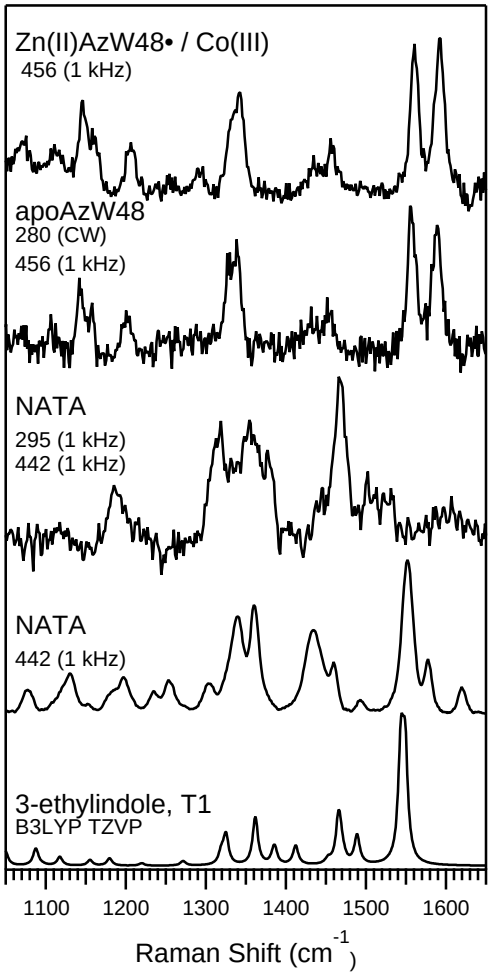

Figure A.3.2 Comparison of experimental and theoretical Raman spectra of tryptophan-containing compounds. Sample type, probe wavelengths (2nd harmonic 442 or 456 nm), and repetition rate of pump and probe sources (continuous wave, CW, or pulsed) are inset. Raman spectra of deoxygenated 250 μM azurin samples were collected in a right-angle geometry using a cuvette. For apoAzW48, a 280 nm CW beam (power=1 mW) was perpendicular to the Raman probe beam (power=15 mW), and the signal was collected through a mechanical shutter (200 μsec, 500 Hz). For NATA, the sample also contained the reagents described in Figure A.3.1, and a 295 nm beam was either present (3rd spectrum) or absent (4th Spectrum). A vibrational spectrum of the 3-ethylindole triplet (bottom) was calculated with B3LYP/TZVP using density functional theory method.

A.4 Transient absorption spectra of N-acetyl-l-tryptophanamide triplet

The transient absorption of N-acetyl-l-trytopanamide (NATA) was measured using flash photolysis of deoxygenated samples for comparison with the steady-state results observed in azurin. See Chapter 3 for details. Potassium iodide was used to enhance the intersystem crossing yield. Sodium dithionite was used to maintain the samples oxygen free, and prevent the formation of iodates. In Figure A.4.1, a transient triplet-triplet absorption with a peak at 450 nm was observed with a μs lifetime following excitation with a 295 nm pulse (~10 ns, see Chapter 2). This result agrees with previous reports of a triplet-triplet absorption with a maximum at 450-460 nm for L-tryptophan.[6]

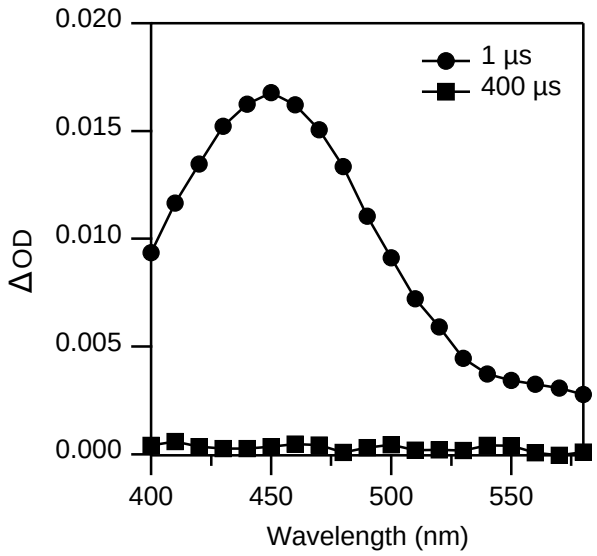

Figure A.4.1 Transient absorption spectra of 100 µM N-acetyl-l-tryptophanamide (NATA), 1 M KI, 1 mM Na_2SO_3, 40 mM Tris, using 295 nm 75 µJ pulses for excitation. See text for details.

A.5 References

1. Bulieris, P. V.; Behrens, S.; Holst, O.; Kleinschmidt, J. H., Folding and insertion of the outer membrane protein OmpA is assisted by the chaperone Skp and by lipopolysaccharide. *J. Biol. Chem* **2003,** *278* (11), 9092-9099.

2. Surrey, T.; Jähnig, F., Refolding and oriented insertion of a membrane protein into a lipid bilayer. *Proc. Natl. Acad. Sci. U. S. A.* **1992,** *89*, 7457-7461.

3. Patel, G. J.; Behrens-Kneip, S.; Holst, O.; Kleinschmidt, J. H., The periplasmic chaperone Skp facilitates targeting, insertion, and folding of OmpA into lipid membranes with a negative membrane surface potential. *Biochemistry* **2009,** *48*, 10235-10245.

4. Larson, B. C.; Pomponio, J. R.; Shafaat, H. S.; Kim, R. H.; Leigh, B. S.; Tauber, M. J.; Kim, J. E., Photogeneration and quenching of tryptophan radical in azurin. *J. Phys. Chem. B* **2015,** *119*, 9438-9449.

5. Shafaat, H. S.; Leigh, B. S.; Tauber, M. J.; Kim, J. E., Spectroscopic comparison of photogenerated tryptophan radicals in azurin: effects of local environment and structure. *J. Am. Chem. Soc.* **2010,** *132*, 9030-9039.

6. Bent, D. V.; Hayon, E., Excited state chemistry of aromatic amino acids and related peptides. III. Tryptophan. *J. Am. Chem. Soc.* **1975,** *97* (10), 2612-2619.